UNIVERSITÀ
DI TRENTO

DEPARTMENT OF INFORMATION ENGINEERING AND COMPUTER SCIENCE
DEPARTMENT OF INDUSTRIAL ENGINEERING
FONDAZIONE BRUNO KESSLER

Doctorate Program in Industrial Innovation

Quantum interference with undetected photons for sensing and imaging

Chiara Michelini

Advisor
Prof. Lorenzo Pavesi
Università di Trento

Co-Advisor
Dr. Massimiliano Dispenza
Leonardo S.p.A.

April 2026

A Milla

"Tu sei per me
la più bella del mondo"

Abstract

Quantum interference with undetected photons has gained significant attention in the past ten years due to its potential to decouple the probing and the detection of an active sensing system. The technique is based on correlated photon pairs: one photon interacts with the analyte, and the signature of the interaction is stored in its correlated counterpart. The probing photon remains *undetected*, while the other photon is measured. When the photons are highly non-degenerate, the spectral separation of the probing and detected photons offers significant advantages in terms of ease of operation and enhanced sensitivity, enabling more precise measurements and analysis with respect to other sensing techniques. This possibility enables a wide range of applications, particularly in fields such as imaging, spectroscopy, and optical coherence tomography, among others. This thesis describes experiments for imaging and sensing based on undetected photons, both in a free-space optical setup and in an integrated photonic circuit. The free-space configuration was used to perform undetected three-dimensional imaging reconstruction of diffusive targets. This validation of imaging with undetected photons paves the way to further development to in vivo biomedical imaging, covert imaging, and remote sensing. On the other hand, the integrated configuration overcomes the limitation of alignment tolerance and scalability of a free-space optical setup, enabling the development of integrated sensors based on undetected photons.

Acknowledgments

During my PhD journey, I had the opportunity to meet and work with the most extraordinary people. This has been an enriching experience, of which I am really proud. Those who mostly contributed to my growth, both professionally and personally, are acknowledged below:

- Lorenzo Pavesi, my academic supervisor, who patiently supervised all of my thesis works from the bachelor's to the PhD. I am really grateful for all the constructive feedback I received and for everything I learned.
- Massimiliano Dispenza, my industrial tutor, who gave me the opportunity to be part of the growth of a newly born research laboratory in an industrial environment. I surely experienced something outstanding.
- Massimiliano Proietti, the principal investigator of the Quantum Laboratory in Leonardo, for always being one of us. I am really glad for the environment you created in the lab, and it is a pleasure to be a part of your team.
- Ugo Zanforlin, for getting his hands dirty with me in the lab. Thank you for all the time you dedicated to me, for shouldering the mental load. For listening to all my complaints and doubts, I will always be grateful to you.
- Stefano Signorini, I really learned a lot from you, and I hope we will cross our professional paths again in the future.
- Alessia Suprano, for her illuminating approach to research. You are an inspiration. Thank you for seeing and encouraging my strengths, and for your friendship.
- Francesco Poggiali, for the most fun I ever had aligning an optical setup.
- Riccardo Romanelli, the idler to my signal: somehow we are in coincidence. Thank you for your constant support and for letting me be my nitpicking self.
- Valentina Carpenella, for all the coffee we drank and the tea we spilled. Thank you for your friendship, for all the talk and gossip.
- Davide Rizzotti, for being close even when we were kilometers or miles apart.
- Giusy Cancelliere and Elisa Frigato, my flatmates, for making our apartment a home.
- Erica Alfinelli and Fabio Mazza, my dearest friends, for visiting me in all my adventures.
- Guendalina Tonidandel and Monica Tramontin, with you I feel as light as I was when we first met at 13, 13, and 14.
- Pietro Michelini, my brother and my first reviewer.
- My mother, Federica Azzali, for loving me.

Contents

List of Figures

List of acronyms

ADC	Asymmetric Directional Coupler
BPF	Band-Pass Filter
BS	Beam Splitter
DM	Dichroic Mirror
DFG	Difference Frequency Generation
EM	Electromagnetic
FWHM	Full Width at Half Maximum
FWM	Four-Wave Mixing
h.c.	Hermitian Conjugate
JSA	Joint Spectral Amplitude
JSI	Joint Spectral Intensity
KTP	Potassium Titanyl Phosphate (KO_5PTi)
OCT	Optical Coherence Tomography
OPA	Optical Parametric Amplification
PDC	Parametric Down-Conversion
PIC	Photonic Integrated Circuit
PM	Phase Matching
PSF	Point Spread Function
pp	Periodically Poled
QPM	Quasi-Phase Matching
SFG	Sum Frequency Generation
SFWM	Spontaneous Four-Wave Mixing
SNR	Signal to Noise Ratio
SPAD	Single Photon Avalanche Diode
SPDC	Spontaneous Parametric Down-Conversion
TE	Transverse Electric
TEM	Transverse Electromagnetic
TM	Transverse Magnetic

Introduction

Optical imaging and sensing play a crucial role in biomedical diagnostics [1], environmental sensing [2], and remote sensing [3,4], among others. A common implementation for imaging and sensing relies on active systems, in which a sample to be analyzed is probed by an external light source. In a typical active-system configuration, the probing light interacts with a sample, and it is analyzed to retrieve information about the changes caused by this interaction in a detection stage. The probing light is usually required to fall within a spectral region where detection technologies are efficient to ensure that it can be effectively measured after the interaction with the target. However, this condition often involves a trade-off between the detector's efficiency, noise level, cost, and ease of use and the sample's spectral responsivity.

Early solutions to this limitation relied on time-coincidence measurements of time-correlated photon pairs generated via spontaneous parametric nonlinear optical processes: the noise at the detector measuring the photon interacting with the sample is mitigated by taking coincidence measurements with its time-correlated photon partner [5]. This temporal correlation allows discriminating between photon-pair events and uncorrelated noise contributions at the detectors. The coincidence-to-accidental ratio, i.e., the ratio between the total number of coincidences and the number of accidental coincidences originating from uncorrelated detection events [6], is improved by selecting the wavelength of the non-interacting photon in a spectral region where the detection technologies exhibit low dark counts and high efficiency.

The advantages become even more significant when the technique is extended to imaging. In addition to the temporal correlation, an imaging implementation exploits the spatial correlation (or momentum anti-correlations) between the photons of the pair. Within this framework, the technique is known as *quantum ghost imaging* [7, 8]. In a ghost imaging configuration, one photon of the pair interacts with the sample and is detected without spatial resolution, while its correlated partner is directly measured with a spatially resolving detector such as a camera. When the photon transmitted through the sample is detected, it heralds the correlated photon at the camera, allowing the image of the sample to be reconstructed from the accumulated coincidence events. To optimize the acquisition, the photon source can be selected such that the probing photon - usually named *the idler* - is in a spectral region where the sample responsivity is strong, while the photon measured at the camera - *the signal* - falls within a spectral region where spatially resolving detection technologies are mature and efficient. This solution reduces the requirement for an efficient spatially resolving detector at the probe wavelength, as the probing photon is measured with a single-pixel detector. However, even though the trade-off between the sample responsivity and the detector efficiency has been relaxed, the choice of the probing wavelength is still constrained by the single-pixel detector's availability. Solutions based on frequency conversion modules [6, 9] allow the idler to be shifted to wavelengths compatible with available detectors; however, they exhibit limited efficiency.

These limitations motivate the technique of *quantum interference with undetected photons* [10], which is an interferometric method that allows the probing photon to remain undetected, fully decoupling probing and detection and enabling novel applications in active imaging and sensing. Quantum interference with undetected photons exploits the effect of *induced coherence without induced emission*, which was first introduced by Wang, Zou, and Mandel in 1991 [11, 12].

Induced coherence without induced emission manifests as interference between two alternative indistinguishable photon-pair generation processes. This is commonly implemented by cascading two probabilistic photon-pair sources. The generation probability in each source must be sufficiently small so that simultaneous generation events in both sources are negligible. The generation processes are indistinguishable when the sources generate photons that are identical in every degree of freedom, their optical paths are overlapped (spatial indistinguishability) [13], and the relative path between the signal and the idler is identical within their coherence length (temporal indistinguishability) [14]. With these conditions satisfied, the probability amplitudes for the pair to be generated in the first source and in the second source interfere. When a sample is placed between the sources, its properties affect the interference pattern: the interference pattern can be measured to retrieve the properties of the sample. Interestingly, if the object interacts with only one photon of the pair, it affects the whole two-photon state, and the altered interference pattern can be observed by detecting the photons that did not interact with the sample. The interacting photon remains undetected, and the detection is completely decoupled from the interaction.

The technique was experimentally demonstrated for spectroscopy [15, 16] and for imaging [17]. However, the state-of-the-art implementations present two main limitations. First, they are heavily affected by losses of the probing photon, limiting their practical application to partially transmissive or purely reflective samples. Second, the experimental configurations rely on free-space optical setups, which inherently suffer from limited robustness, portability, and alignment tolerance.
This thesis addresses these limitations. Specifically, it:

i. experimentally investigates three-dimensional imaging of rough-surface diffusive targets with undetected photons;

ii. demonstrates phase sensing with undetected photons using a photonic integrated circuit.

Indeed, practical imaging applications have been focused on imaging thin biological samples, in which the probing photon is transmitted through the sample and its properties are inferred from the local variations of the interference visibility measured on the detected photons [18,19]. In such experiments, photons are typically generated via broadband spontaneous parametric down-conversion processes [20], such that the signal falls within a spectral region where efficient cameras exhibit significant sensitivity (wavelength range: 0.4-1.1 μm [21]), and the idler lies in the mid-infrared spectral region (MIR, 2-20 μm [22]). The latter is a relevant spectral region for imaging, as many organic and inorganic molecules exhibit strong resonances in the MIR [23]. A consequence of the broadband processes is the reduced coherence length of the generated photons, which enables sensitive optical coherent tomography [24] with undetected photons [25,26], allowing three-dimensional imaging. A major challenge for three-dimensional imaging of realistic targets with undetected photons is preserving the indistinguishability between the photons generated in the two alternative generation processes. In particular, the idler generated in the first process interacts with the target and can be diffused, degrading the spatial indistinguishability necessary for interference with the idler generated in the second source. Addressing this limitation would be an important step forward for three-dimensional imaging with undetected photons, as it would enable imaging of in vivo biological samples, rather than being restricted to thin samples in a transmissive configuration.
Beyond biomedical imaging, such a configuration could also enable remote-sensing applications. In this case, the limited coherence length of the photons becomes a significant constraint, as the optical paths are required to be matched within the photon coherence length, which is not feasible if the position of the remote target is unknown. To solve this issue, recent efforts have focused on theoretically demonstrating a configuration such that temporal indistinguishability is

preserved even if the optical paths of the idler and the signal are not matched [27]. Nevertheless, these studies do not address the issue of the spatial distinguishability induced by the interaction with the target. In this thesis, I study this effect and experimentally explore strategies to enable three-dimensional imaging of diffusive targets with undetected photons.

To address the second limitation of the current state-of-the-art configurations, i.e., their reliance on free-space optical implementations, integrated photonics would be the ideal platform to implement an experiment based on undetected photons. Indeed, alignment between the sources is guaranteed in an integrated device, as the optical modes supported by an integrated structure are spatially confined. This would maximize the spatial indistinguishability between the generation processes. Moreover, devices based on photonic integrated circuits hold the promise of compatibility with mass-manufacturable consumer electronics, enabling compact and scalable devices characterized by reduced footprint, alignment quality, and robustness. In this thesis, I study the performance of a photonic integrated circuit designed for phase measurements with undetected photons.

This work has been written in the framework of the Industrial Innovation doctorate program offered by the University of Trento (Italy), which aims to train specialized experts in a setting that bridges academia with industry.

On the academic side, this thesis is the result of research work conducted at the Nanoscience Laboratory of the Physics Department of the University of Trento, in collaboration with ICFO, the Institute of Photonic Sciences in Barcelona (Spain), where I worked on the study and characterization of the first integrated design for undetected interference, performing the first on-chip sensing experiment with undetected photons [28, 29].

On the industrial side, the work discussed in this thesis has been carried out at the Quantum Technologies Unit of the Leonardo Innovation Hub of Leonardo S.p.A. in Rome (Italy), a company specializing in aerospace, defense, and security. This collaboration provided the opportunity to bring research-oriented activities into an industrial environment, prioritizing practical applications. The activities carried out at Leonardo focused on the study of imaging applications based on entangled photons [30], as well as on the experimental implementation of a setup for imaging with undetected photons for both partially transmissive targets and diffusive rough-surface targets [31]. Part of the work at Leonardo was conducted in the framework of the project MUQUABIS (Multiscale Quantum BioImaging and Spectroscopy) [32].

This thesis is organized as follows:

- In **Chapter 1**, I introduce fundamental concepts in both free-space and integrated photonics relevant to this thesis. This chapter presents a discussion on the nonlinear optical processes employed in this work to generate correlated photon pairs: spontaneous parametric down-conversion and spontaneous four-wave mixing.
- **Chapter 2** presents the effect of induced coherence without induced emission, which is the fundamental concept underlying undetected photon interference.
- In **Chapter 3**, I discuss the applications of induced coherence without induced emission to two-dimensional imaging. In addition to the theoretical discussion, I show the experimental configurations I implemented and the relative experimental results.
- In **Chapter 4**, I introduce the concept of three-dimensional imaging with undetected photons enabled by optical coherent tomography. Then, I extend its application to imaging rough-surface targets.
- In **Chapter 5**, I present the experiment of phase measurement with undetected photons

using an integrated design.

- The **Conclusions** summarize the final remarks of the thesis.
- In **Appendix A**, I detail the calculations that were too tedious to be included in the main text, and in **Appendix B**, I share the codes for the simulations discussed in this work.

1. Fundamentals

The results of this thesis rely on entangled photon pair generation either with a free-space optical setup based on spontaneous parametric down-conversion (SPDC) or with spontaneous four-wave mixing (SFWM) in a photonic integrated circuit.
In this chapter, I introduce the fundamental concepts for both free-space and integrated photonics that are functional to this thesis, together with an overview of nonlinear optics and a detailed discussion on SPDC and SFWM.

1.1. Linear optics

The optical response of a medium to a driving optical field $\boldsymbol{E}$ is determined by the polarization vector $\boldsymbol{P}$. In a dielectric material, polarization is governed by valence electrons, weakly bound to the ion cores, and displaced by a driving optical field. An oscillating driving field induces an oscillating motion in the valence electrons of the material, and the accelerated charges radiate an electromagnetic (EM) field in turn [33]. Considering a single atom and modeling the nucleus-electron interaction as a damped oscillator driven by the electric field (Lorentz model), at the first approximation order, the radiated EM field has the same frequency as the driving field and amplitude proportional to the driving field amplitude [34]. Therefore, at the first approximation order, the light-matter interaction is governed by a linear relation:

$$\boldsymbol{P} = \varepsilon_0 \boldsymbol{\chi}^{(1)} \cdot \boldsymbol{E}, \tag{1.1}$$

where ε_0 is the vacuum permittivity and $\boldsymbol{\chi^{(1)}}$ is optical susceptibility, which is a 9-component, 2-rank tensor. The phase of the radiated field depends on the nucleus-electron interaction. Interference occurs between the driving and the radiating fields, and the resulting wave has a phase that is an intermediate between the phase of the driving field and the radiated field [33].

Considering a material of length L along the propagation dimension z of the driving field instead of a single atom, the number of atoms N in the material scales linearly with its thickness, i.e., $N \propto L$. The resulting wave has the same frequency as the driving field and exhibits a phase shift with respect to the driving field that is proportional to N. Effectively, it is like the driving field, propagating in the material, builds up a phase proportional to the material thickness, experiencing slower velocity inside the material. The ratio between the speed of light in the vacuum and the speed of propagation in the material is the real part of the material refractive index n. In general, the refractive index is a complex quantity $\tilde{n}$, and it is related to the optical susceptibility as $\tilde{n}^2 = 1 + \chi$ [35]. While the real part of the refractive index is connected to the light propagation in the material, the imaginary part is associated with absorption. In this thesis, I consider the light-matter interaction to occur in the transparent window of the material, i.e., $\mathbb{Im}(\tilde{n}) = 0$, and I refer to the refractive index as a real quantity n.

The response of the material depends on the frequency of the driving field, i.e., the refractive index of the material exhibits a frequency dependence. For a detailed report of the refractive index of the materials discussed in this thesis, see Sect. 1.1.3.

The optical response of the material generally depends on the propagation direction of the driving field. Hence, $\boldsymbol{\chi}^{(1)}$ and n are tensors. Such materials in which the optical response depends on the propagation direction are called *anisotropic materials*. It can be demonstrated that the refractive index of such materials can be represented as an ellipsoid in the space coordinate, in which three principal axes can be identified: x, y, and z. Conventionally, the axes are chosen such that $n_z > n_y > n_x$ [36]. When light is not polarized along one of the principal axes, the orthogonal components of the field undergo a different phase delay, and the polarization of the field is affected.

This thesis deals with both free-space and integrated optics applications. These cases are distinguished by the spatial distribution of the refractive index in the propagation material. In the following, I treat light propagation, taking into account the spatial dependence of the refractive index $n(\boldsymbol{r})$, with $\boldsymbol{r} = (x, y, z)$ denoting the spatial coordinate, with focus on the spatial evolution of the field along the propagation coordinate z.

Consider an electric field $\tilde{\boldsymbol{E}}(\boldsymbol{r}, t)$ propagating in a transparent material characterized by refractive index $n(\boldsymbol{r})$. Assume that the field is a monochromatic wave with optical frequency ω, $\tilde{\boldsymbol{E}}(\boldsymbol{r}, t) = \boldsymbol{E}(\boldsymbol{r})\mathrm{e}^{-i\omega t}$. In the absence of free charges, and assuming that the distribution of the refractive index in the structure varies slowly enough, $\mathbf{E}(\mathbf{r})$ satisfies the equation [37]

$$\nabla^2 \boldsymbol{E}(\boldsymbol{r}) + \left(\frac{\omega}{c}\right)^2 n^2(\boldsymbol{r})\, \boldsymbol{E}(\boldsymbol{r}) = 0. \tag{1.2}$$

Assume that z is the propagation direction of the field and that the refractive index does not vary along the propagation direction, i.e., $n(\mathbf{r}) = n(x, y)$. We look for solutions of Eq. (1.2) that are separable such that they are not subjected to spatial divergence, i.e., they satisfy Eq. (1.3), and with finite intensity in the xy-plane - Eq. (1.4):

$$\boldsymbol{E}(x, y, z) = \boldsymbol{U}(x, y)\, \mathrm{e}^{i\beta z}, \tag{1.3}$$

and

$$\iint dx\, dy\, |\boldsymbol{U}(x, y)|^2 < \infty. \tag{1.4}$$

By substituting Eq. (1.3) in Eq. (1.2), one finds the two-dimensional Helmholtz equation:

$$\nabla_\perp^2 U(x, y) + \left[\left(\frac{\omega}{c}\right)^2 n(x, y) - \beta^2\right] U(x, y) = 0 \tag{1.5}$$

The two-dimensional Helmholtz equation is similar to the two-dimensional time-independent Schrödinger equation for a particle with a wave function $\psi(x, y)$ confined in two-dimensional potential $V(x, y)$ with energy E:

$$-\frac{\hbar^2}{2m}\nabla_\perp^2 \psi(x, y) + (V(x, y) - E)\, \psi(x, y) = 0. \tag{1.6}$$

In this similarity, the refractive index $n(x, y)$ in Eq. (1.5) plays the role of the potential $V(x, y)$ in Eq. (1.6).

Taking into account the very well-known results for Eq. (1.6) and its similarities with Eq. (1.5), I distinguish between the two specific cases analyzed in this thesis:

- The refractive index is constant, i.e., free-space propagation.
- The refractive index exhibits a spatial dependence as in $n(x, y)$, in the specific case of channel optical waveguides.

1.1.1. Free-space optics

If the refractive index is a constant, a solution for Eq. (1.5) that satisfies both Eq. (1.3) and Eq. (1.4) cannot be found. That is equivalent to looking for a solution of the Scrödinger equation (1.6) for a free particle. Indeed, one finds that the probability density for the position of the free particle in free-space is not normalizable, i.e., condition (1.4) cannot be satisfied in free-space.

Indeed, wave propagation in free-space is subjected to divergence, i.e, the condition in Eq. (1.3) must be relaxed to

$$\boldsymbol{E}(x,y,z) = \boldsymbol{U}(x,y,z)\,\mathrm{e}^{i\beta z} \tag{1.7}$$

A solution for $\boldsymbol{U}(x,y,z)$ in the paraxial approximation[1] is the Gaussian beam, a diverging solution that maintains its transverse shape during propagation. An mn-order Gaussian beam exhibits m and n nodes along the x and y axes, respectively, and is referred to as Transverse Electromagnetic mode of order m,n (TEM_{mn}). In the free-space applications discussed in this thesis, we are interested in the fundamental Gaussian beam TEM_{00}, which has a single-lobed Gaussian profile with no transverse nodes. In the following, when referring to a Gaussian beam, I will refer to the fundamental order.

The analytical expression for the TEM_{00} is

$$\boldsymbol{U}(x,y,z) = \boldsymbol{U_0}\frac{w_0}{w(z)}\exp\left[-\frac{x^2+y^2}{w^2(z)}\right]\exp\left[-ik\frac{x^2+y^2}{2R(z)}+i\zeta(z)\right], \tag{1.8}$$

where $w(z)$ is the beam radius at position z, defined as

$$w(z) = w_0\sqrt{1+\left(\frac{z}{z_R}\right)^2}, \tag{1.9}$$

with

$$z_R = \frac{\pi w_0^2}{\lambda}. \tag{1.10}$$

w_0 is called the beam waist and z_R is the Rayleigh range. The beam radius is the distance from the axis at which the intensity on the xy-plane drops to $1/\mathrm{e}^2$ of its peak value. The relation between the beam radius and the full width at half maximum (FWHM) is

$$w(z) = \frac{\mathrm{FWHM}(z)}{\sqrt{2\,\ln(2)}}. \tag{1.11}$$

The beam radius $w(z)$ follows a hyperbolic shape, with a minimum at the waist w_0. For $z \gg z_R$, the beam diverges linearly, with a divergence angle

$$\theta = \arctan\left(\frac{\lambda}{\pi w_0}\right). \tag{1.12}$$

The Rayleigh range z_R is the distance along z from the waist, such as $w(z_R) = \sqrt{2}\,w_0$. Eq. (1.8) assumes that the beam waist is located at $z = 0$, for simplicity. The beam radius, the Rayleigh range, and the divergence angle are emphasized in Fig. 1.1. The term $R(z)$ denotes the radius of curvature of the wavefront,

$$R(z) = z\left[1+\left(\frac{z_R}{z}\right)^2\right] \tag{1.13}$$

[1] The paraxial approximation assumes that the divergence angle of the beam is sufficiently small so that the field primarily propagates along the z-axis.

and $\zeta(z) = \arctan(z/z_R)$ is the Gouy phase, which is an additional phase shift contribution acquired upon propagation.

The parameters that uniquely characterize a Gaussian beam and that are sufficient for predicting their propagation are the wavelength λ, the waist w_0, and the waist position.

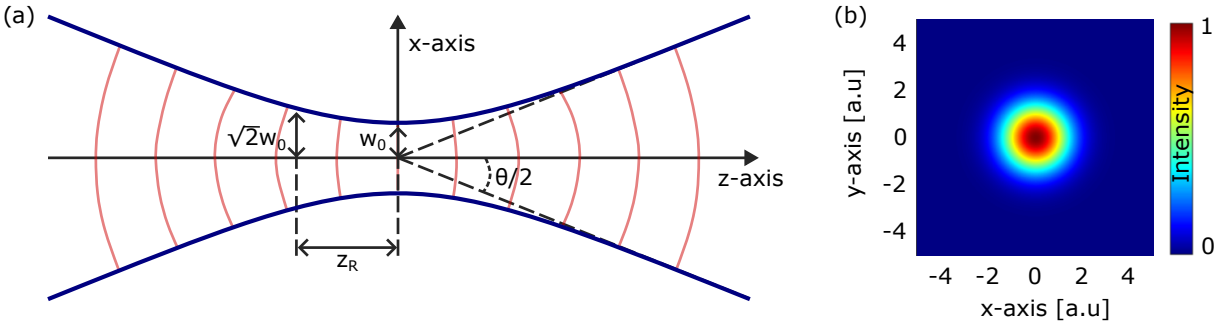

Figure 1.1.: TEM_{00} Gaussian beam propagating along the z-axis. (a) Schematic representation of a Gaussian beam with waist w_0, Rayleigh range z_R, and divergence angle θ. The blue lines delimit the spatial localization of the beam in the xz-plane, and the red lines show the beam radius at different positions z. (b) Normalized transverse intensity distribution of the beam in the xy-plane.

Gaussian beams for experimentalists

Some simple considerations are useful when working in an experimental setup that employs Gaussian beams:

- Increasing the beam waist reduces the beam divergence (z_R increases).
- For the same beam waist, a beam with a longer wavelength is characterized by larger divergence (z_R decreases increasing λ).
- The wavefront is nearly planar at the beam waist, and for $z \ll z_R$: Gaussian beams with a very large z_R can be considered collimated ($R(z)$ is large for large values of z_R).

Moreover, it is appropriate to manipulate Gaussian beams either in the near-collimated regime ($z \ll z_R$) or in the far-field asymptotic regime ($z \gg z_R$), where standard optical elements can be accurately described using the ray optics approximation. In the intermediate region around the Rayleigh range ($z \sim z_R$), the full Gaussian beam formalism is required, as geometrical optics no longer provides an accurate description. In this thesis, Gaussian beams have been manipulated within the near-field and far-field regimes. For all the optical elements used in free-space setups in this thesis, the thin-lens approximation holds. When focusing (collimating) a collimated (diverging) beam with waist w_0^A, the output beam waist w_0^B in the thin-lens approximation is [38]

$$w_0^B = \frac{f\lambda}{\pi w_0^A}, \tag{1.14}$$

where f is the focal length of the lens.

1.1.2. Guided-wave optics

If the refractive index depends on the transverse spatial coordinates, i.e., $n(\boldsymbol{r}) = n(x, y)$, eigen-solutions of Eq. (1.5) are supported. Such eigenfunctions are guided in the material without

being subjected to divergence and are called *optical modes*. The specific case $n(\boldsymbol{r}) = n(x, y)$ represents a two-dimensional optical confinement, and the guiding structure is called a *waveguide*. A few examples of cross-sections for two-dimensional optical confinements are shown in Fig. 1.2. In a waveguide, a medium characterized by a certain refractive index (core) is embedded in a medium with a lower refractive index (cladding). The index contrast allows light to propagate in the waveguide core through total internal reflection. Optical modes in waveguides are the result of the interference of the plane waves propagating in the waveguide core with bounching angles $+\theta$ and $-\theta$, producing stationary field intensity distribution in the x and y dimensions [35].

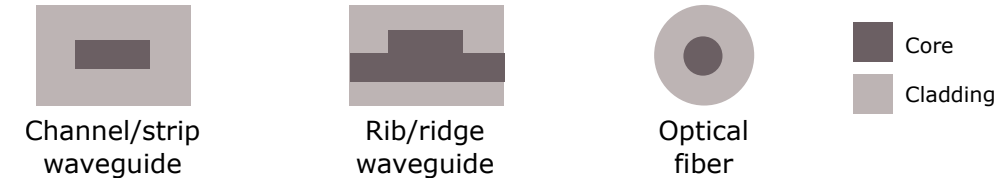

Figure 1.2.: Examples of cross-sections of structures for a two-dimensional optical confinement.

Equivalently to the case of a particle subjected to a two-dimensional potential well, the eigenfunctions of Eq. (1.5) are characterized by discrete eigenvalues. In the confined particle case, the eigenvalues are the discrete energies E of the particle in the well. Similarly, Eq. (1.5) admits as eigenvalues discrete values for the refractive index experienced by the modes in the confined structure. Such eigenvalues are called effective refractive indexes. A waveguide that sustains the fundamental mode only is called a single-mode waveguide, otherwise it is called a multimode waveguide. Fig. 1.3 shows the fundamental and first-order optical modes in two different polarization states, transverse electric (TE) and transverse magnetic (TM). The integrated structures presented in this work only admit the fundamental and first-order TE optical modes, TE0 and TE1, respectively.

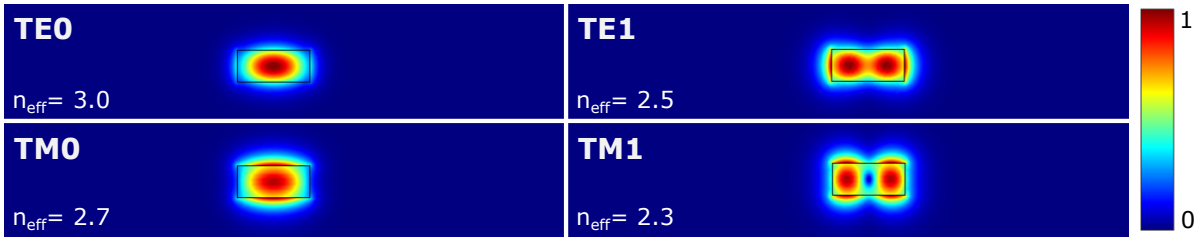

Figure 1.3.: Simulations of the normalized norm of the electric field for the fundamental (0) and first order (1) optical modes in the TE and TM polarizations, at wavelength 1.55 μm. The waveguide core is made of silicon, and its cross-section is 0.8 μm $\times$ 0.35 μm. The cladding is made of silica. The effective index is indicated for each mode with n_{eff}.

In the same way in which the eigenfunctions of the Schrödinger equation for a particle in a finite potential well are not entirely confined within the well, the waveguide modes are characterized by evanescent field in the cladding. Less confined modes experience a lower refractive index in the waveguide, since they experience more the lower index of the cladding. Typically, higher-order modes are less confined. When two waveguides are in proximity, the evanescent field of a wave propagating in a waveguide can excite the mode in the other one, allowing transferred from one waveguide to the other. This phenomenon is subjected to the phase matching (PM) condition, according to which the propagating solution and a solution supported by the adjacent waveguide exhibit the same effective refractive index. The coupling length, which is the distance in the propagation direction for which the mode is coupled from one waveguide to the other, depends on the distance between the waveguides. A structure that allows coupling modes from

one waveguide to another is a directional coupler. Coupling can also occur between different order modes. In that case, the structure is an asymmetric directional coupler (ADC).

Among the factors that influence the mode, the geometry of the waveguide must be considered. As an example, bending waveguides admit skewed optical modes, and the refractive index experienced is lower than in a straight waveguide, as the mode is less confined. Fig. 1.4 shows how a mode is affected by the radius of curvature of the waveguide. Since the geometry of the refractive index affects the mode, coupling can occur between modes of different order in a bending multimode waveguide, i.e., the PM condition can be satisfied between optical modes of different order in a bending structure, and a mode can excite another one.

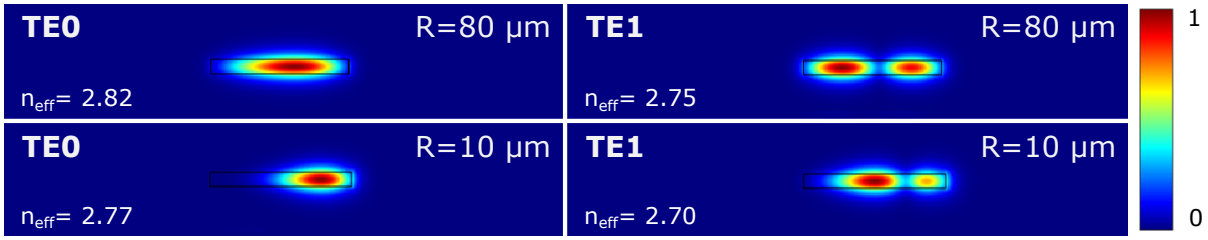

Figure 1.4.: Simulations of the normalized norm of the electric field for the fundamental and first-order TE optical modes at wavelength 1.55 μm in a bending waveguide, with bending radius R. Here is shown the cross-section of the curve, with the center of the curve located to the left. The waveguide core is made of silicon, and its cross-section is 2 μm $\times$ 0.22 μm. The cladding is made of silica. The effective index is indicated for each mode with n_{eff}.

1.1.3. Refractive indexes of the materials employed in this work

In this section, I detail the refractive indexes of the materials treated in this thesis. Specifically, I will discuss the Potassium Titanyl Phosphate (KTP), KO_5PTi, for the free-space applications, and the effective refractive indexes for the fundamental and first-order optical modes in multimode silicon waveguides.

Refractive index in KTP

KTP is an anisotropic material, and it is characterized by three principal axes x, y, z. Eqs (1.15) and (1.16) report the Sellmeier equations for KTP, which express the dependence of the refractive index on the wavelength.

The Sellmeier equations in the **wavelength range 440 nm-3.55 μm**, at a **temperature of 20°C** are [39]

$$n_i^2(\lambda) = a_i + \frac{b_i}{\lambda^2 - c_i} + \frac{d_i}{\lambda^2 - e_i}, \tag{1.15}$$

where the subscript $i = x, y, z$ labels a principal axis, λ is the wavelength expressed in μm, and the values of the coefficients $a_i, ..., e_i$ are listed in Tab. 1.1.

i	a_i	b_i	c_i	d_i	e_i
x	3.29100	0.04140	0.03978	9.35522	31.45571
y	3.45018	0.04341	0.04597	16.98825	39.43799
z	4.59423	0.06206	0.04763	110.80672	86.12171

Table 1.1.: Coefficients for the refractive indexes in Eq. (1.15) for the KTP, at a temperature of 20°C.

Katz et al. [40] provide the Sellmeier equation for the z-axis in a broader spectral region (**350 nm-4.5μm**) at a **temperature of 20°C**:

$$n_z^2(\lambda) = 1 + \frac{1.71645 \cdot \lambda^2}{\lambda^2 - 0.01346} + \frac{0.0594 \cdot \lambda^2}{\lambda^2 - 0.06503} + \frac{0.3226 \cdot \lambda^2}{\lambda^2 - 67.1208} - 0.01133 \cdot \lambda^2 \tag{1.16}$$

Eqs. (1.15) and (1.16) do not consider the temperature dependence of the refractive index. When the temperature deviates from the temperature of 20°C, an adjustment Δn to the refractive index is necessary. This adjustment is expressed in Eq. (1.17) as a function of the temperature and the wavelength, in the **wavelength range 532 nm-1585 nm**, in the **temperature range 25°C-200°C** [41], and for the **principal axes y, z**:

$$\Delta n(\lambda, T) = m_1^i(\lambda)(T - 25°C) + m_2^i(\lambda)(T - 25°C)^2, \tag{1.17}$$

with λ expressed in μm, $i = y, z$ labels a principal axis, and the coefficients m_j^i, with $j = 1, 2$, depend on the wavelength as

$$m_j^i(\lambda) = \sum_{k=0}^{3} \frac{a_j^i[k]}{\lambda^k}. \tag{1.18}$$

The arrays a_j^i, of the k-th element $a_j^i[k]$, are reported in Tab. 1.2.

	k=0	k=1	k=2	k=3
a_1^y $[10^{-6}]$:	6.2897	6.3061	-6.0629	2.6486
a_2^y $[10^{-8}]$:	-0.14445	2.2244	-3.5770	1.3470
a_1^z $[10^{-6}]$:	9.9587	9.9228	-8.9603	4.1010
a_2^z $[10^{-8}]$:	-1.1882	10.459	-9.8136	3.1481

Table 1.2.: Numerical values for the elements $a_j^i[k]$ ($i = y, z$; $j = 1, 2$; $k = 0, ..., 3$) used in Eq. (1.18) for the KTP.

In this work, three spectral regions are relevant, centered at wavelengths 0.532 μm, 0.81 μm, and 1.55 μm, with the material thermalized at 73°C. Moreover, this work is interested in the case in which the propagating waves experience the refractive index along the z-axis. While simulations and calculations in this thesis take into account the full spectrum of the propagating waves and allow for tunability of the material temperature according to Eq. (1.17), I report in Tab. 1.3 the refractive indexes at the relevant wavelengths and temperature as a quick reference.

λ [μm]	0.532	0.810	1.550
n_z @ 73°C	1.890	1.845	1.816

Table 1.3.: Refractive indexes along the principal axis z in a KTP crystal at temperature 73°, for the wavelengths relevant to this work.

Effective refractive index in silicon-on-insulator channel waveguides

This work employs multimode channel waveguides with a silicon core and a silica cladding. The advantage of silicon photonics with respect to other platforms is that the contrast index between silicon and silica is strong (3.48/1.44 at a wavelength of 1550 nm at room temperature), allowing for strong optical confinement in small structures [42]. Fig. 1.5 shows the results of a simulation for the effective refractive indexes of the modes of interest in three spectral regions for a multimode waveguide with a core cross-section of 2 μm $\times$ 0.22 μm.

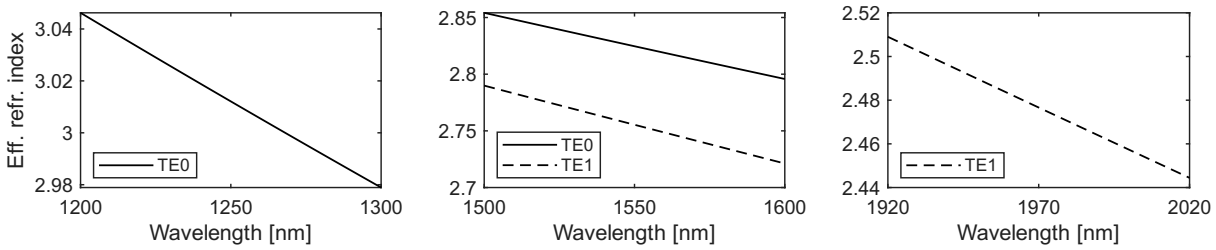

Figure 1.5.: Effective refractive index as a function of the wavelength for the TE0 optical mode (solid line) and for the TE1 optical mode (dashed line) in the spectral regions 1200-1300 nm (left), 1500-1600 nm (center), and 1920-2020 nm (right). The waveguide cross-section is 2 μm $\times$ 0.22 μm.

If the waveguide bends, the optical modes in the waveguide are skewed, and the effective refractive index is affected. A simulation for the effective refractive index as a function of the bending radius is shown in Fig. 1.6, for the modes of interest in this work.

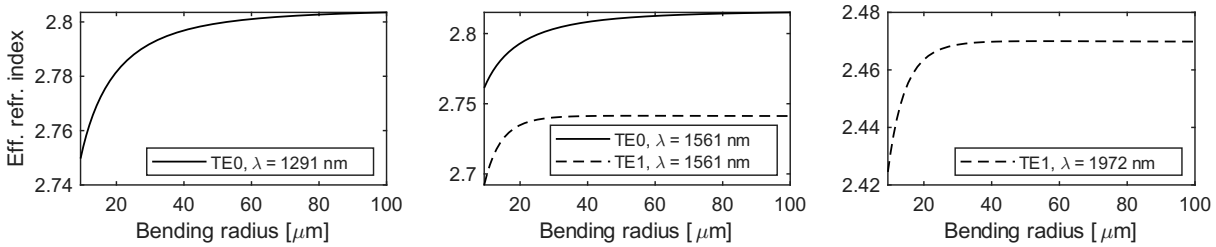

Figure 1.6.: Effective refractive index of the TE0 (solid line) and TE1 (dashed line) optical modes as a function of the bending radius of a waveguide of cross-section 2 μm $\times$ 0.22 μm at wavelength 1291 nm (left), at wavelength 1561 nm (center), and at wavelength 1972 nm (right).

The temperature dependence of the silicon refractive index and the silica refractive index affects the effective refractive index of the mode propagating in the waveguide. In this work, to selectively control the effective refractive index of the modes propagating in specific waveguides, a resistor is positioned in the cladding above the waveguide of interest, and the effective refractive index of the propagating mode is controlled via the Joule effect by flowing a current through the resistor. Fig. 1.7(a) shows a simulation for the temperature distribution on the cross-section of the waveguide, using a metallic sheet-resistor of cross-section 0.6 μm $\times$ 0.3 μm in the cladding positioned 1 μm above the waveguide core to avoid any mode leakage to the metal wire. Fig. 1.7(b) shows the simulation for the effective refractive indexes for the modes and geometries of interest. The waveguides are single-mode waveguides of cross-section 0.45 μm $\times$ 0.22 μm in which propagates the TE0 mode at a wavelength of 1561 nm, and single-mode waveguides of cross-section 0.8 μm $\times$ 0.22 μm in which propagates the TE0 mode at a wavelength of 1972 nm.

1.2. Nonlinear optics

While the output of a linear system is a linear combination of the inputs, nonlinearity enables input mixing [43]. In a light-matter interaction system, nonlinearity yields higher-power terms in the polarization, as displayed in Eq. (1.19):

$$P_i = \varepsilon_0 \sum_j \chi^{(1)}_{ij} E_j \ + \ \varepsilon_0 \sum_{jk} \chi^{(2)}_{ijk} E_j E_k \ + \ \varepsilon_0 \sum_{jkl} \chi^{(3)}_{ijkl} E_j E_k E_l \ + \ ... \tag{1.19}$$

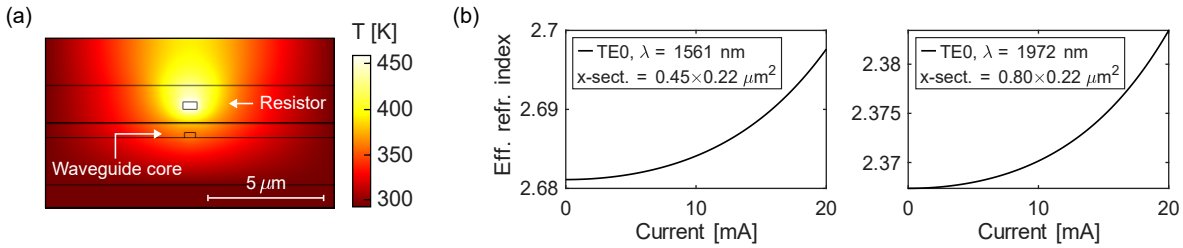

Figure 1.7.: External current control on the effective refractive index. (a) Simulation for the temperature on the waveguide cross-section when the current is 20 mA. (b) Effective refractive index as a function of the current applied to the resistor, for the optical mode TE0 at 1561 nm in a single-mode waveguide of cross-section 0.45 μm × 0.22 μm (left), and for the mode TE0 at 1972 nm in a single-mode waveguide of cross-section 0.8 μm × 0.22 μm (right).

E_x and P_x are the x-components ($x = i, j, k, l$) of the driving electric field $\boldsymbol{E}$ and of the polarization vector $\boldsymbol{P}$, respectively, and $\boldsymbol{\chi}^{(n)}$ is the optical susceptibility of order n, a tensor of rank $(n+1)$. If the driving field contains components at frequencies $\omega_i, \omega_j, \omega_k, \omega_l$, these frequencies are mixed by the non-zero components of $\boldsymbol{\chi}^{(2)}$ (three-wave mixing) and $\boldsymbol{\chi}^{(3)}$ (four-wave mixing). The nonlinear components come from anharmonic terms that must be introduced into the Lorentz model for strong driving fields, while they are negligible at the first-approximation order. The second-order nonlinearity ($\chi^{(2)}$) is found only in non-centrosymmetric materials, i.e., in materials that present asymmetries in the potential experienced by the electrons. Due to this asymmetry, the orientation of a $\chi^{(2)}$ nonlinear material is relevant for nonlinear optics applications, as I will show when discussing quasi-phase matching. While $\chi^{(2)}$ nonlinearity is not naturally present in centrosymmetric crystals, asymmetries in the electronic potential can be externally induced [44]. The third-order nonlinearity ($\chi^{(3)}$) is present in all dielectric materials.

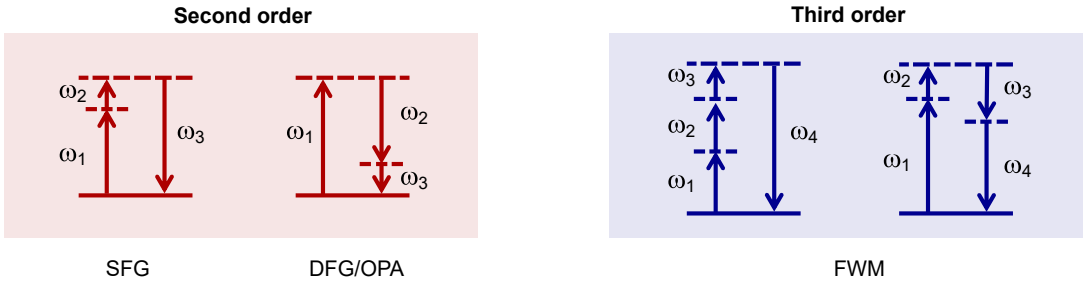

Figure 1.8.: Examples of nonlinear optical processes of the second (left) and third (right) nonlinear orders and their energy conservation conditions. SFG: sum frequency generation; DGF: difference frequency generation; OPA: optical parametric amplification; FWM: four-wave mixing. Solid line: real energy state; dashed line: virtual energy state; arrow: energy transition.

In Fig. 1.8 are schematized the following non-linear optical processes of the second order [33] and third order [45]:

- Sum frequency generation (SFG): two fields at frequencies ω_1 and ω_2 mix to generate a third field at frequency $\omega_3 = \omega_1 + \omega_2$. Particular cases for SFG include:
  - Second harmonic generation: degenerate case, i.e., $\omega_1 = \omega_2 = \tilde{\omega}$ and $\omega_3 = 2\tilde{\omega}$.
  - Parametric up-conversion: one of the input fields, say ω_1, is much stronger than the other (ω_2). The fields at frequencies ω_1 and ω_2 are called "the pump" and "the seed", respectively.

- Difference frequency generation (DFG): two fields at frequencies ω_1 and ω_2 mix to generate a third field at frequency $\omega_3 = \omega_1 - \omega_2$. Specific variations of DFG are:
  - Parametric down-conversion (PDC): the field at frequency ω_1, "the pump", is much stronger than the one at frequency ω_2, "the seed". The spontaneous form of this process, in which one pump photon spontaneously annihilates to generate two new frequencies, is called spontaneous parametric down-conversion (SPDC). SPDC is of major interest in this thesis and is detailed in Sect. 1.2.1.
  - Optical parametric amplification (OPA): the pump at ω_1 is depleted, and the seed at ω_2 is amplified.
- Four-wave mixing (FWM): three fields at frequencies ω_1, ω_2 and ω_3 mix to generate a field at frequency ω_4, with either
  - $\omega_4 = \omega_1 + \omega_2 + \omega_3$.
    In the degenerate case, in which $\omega_1 = \omega_2 = \omega_3 = \tilde{\omega}$, the process is called third harmonic generation, and $\omega_4 = 3\tilde{\omega}$.
  - $\omega_4 = \omega_1 + \omega_2 - \omega_3$.
    The spontaneous form of this process, in which two pump photons at frequencies ω_1 and ω_2 spontaneously annihilate to generate two frequencies ω_3 and ω_4, is of interest in this thesis, and it is described in Sect. 1.2.2.

Due to the typical strength of the optical susceptibilities - $\chi^{(1)}$ (order of unity), $\chi^{(2)}$ ($10^{-12}\ \frac{m}{V}$ in non-centrosymmetric materials), and $\chi^{(3)}$ ($10^{-24}\ \frac{m^2}{V^2}$) [46] - wave mixing is enabled at amplitudes of the optical driving field typically larger than $10^5\ \frac{V}{m}$. Indeed, the first experimental report of a nonlinear optical response of a material was observed by Franken et al. in 1961 [47], after the first operation of the ruby laser, which allowed for a strong driving optical field.

In the following, I present the nonlinear optical processes of relevance to this thesis, specifically spontaneous parametric down-conversion in free-space and spontaneous four-wave mixing in multimode waveguides, in its intermodal declination.

1.2.1. Spontaneous parametric down-conversion

PDC is the case of DFG when one field (the pump, at frequency ω_1) is much stronger than the other (the seed, at frequency ω_2). The third frequency satisfies the energy conservation condition $\omega_3 = \omega_1 - \omega_2$. I assume $\omega_2 > \omega_3$, as it is the most common application of PDC, and I call the fields at ω_1, ω_2 and ω_3, as the pump, the signal, and the idler, respectively. In spontaneous parametric down-conversion (SPDC), a pump photon annihilates, and two photons, the idler and signal, are generated. The process is spontaneous, i.e., the generation of photon pairs is seeded by vacuum fluctuations [46], and requires quantum treatment.

To model SPDC, I assume the following specific conditions to be valid, as they correctly fit the cases of interest of this thesis:

1. The process is collinear, and the pump, the signal, and the idler interact along the spatial coordinate z in a material of length L.
2. The individual polarization of the pump, the signal, and the idler is along one of the principal axes of the crystal if the crystal is anisotropic. The effective nonlinear susceptibility experienced by the photons is a scalar number $\chi^{(2)}$.
3. The pump can be treated classically.

4. The probability for SPDC to occur is low enough to apply the first-order time-dependent perturbation theory when treating the associated unitary transformation [48].

Considering **1.** and **2.**, the Hamiltonian describing the SPDC process at time t is [49]

$$\hat{\mathcal{H}}_{SPDC}(t) = \int_{-\frac{L}{2}}^{\frac{L}{2}} dz\ \varepsilon_0\, \chi^{(2)}\ \hat{E}_p^{(+)}(z,t)\ \hat{E}_s^{(-)}(z,t)\ \hat{E}_i^{(-)}(z,t)\ +\ h.c., \tag{1.20}$$

where the field operator $\hat{E}_x^{(-)}$ ($\hat{E}_x^{(+)}$) is defined by the creation (annihilation) operator $\hat{a}^\dagger$ ($\hat{a}$) for the photon x at frequency ω_x, with wavenumber k_x:

$$\hat{E}_x^{(-)}(z,t) = \hat{E}_x^{(+)\dagger}(z,t) \propto \int d\omega_x\ \exp\left[-i(\omega_x t - k_x(\omega_x)z)\right]\ \hat{a}_x^\dagger(\omega_x). \tag{1.21}$$

The Hamiltonian in Eq. (1.20) describes a process in which either a pump photon annihilates, and signal and idler photons are created (displayed term), or a signal-idler pair annihilates to generate a pump photon (hermitian conjugate term, *h.c.*). According to the condition **3.**, the operator describing the pump can be treated classically:

$$\hat{E}_p^{(+)}(z,t) \to E_p(z,t) = \int d\omega_p\ \alpha(\omega_p)\ \exp\left[i(\omega_p t - k_p(\omega_p)z)\right], \tag{1.22}$$

where $\alpha(\omega_p)$ is the complex amplitude of the pump. The Hamiltonian $\hat{\mathcal{H}}_{SPDC}$ generates the unitary transformation $\hat{\mathcal{U}}$,

$$\hat{\mathcal{U}} = \exp\left[-\frac{i}{\hbar}\int_{-\infty}^{\infty} dt\ \hat{\mathcal{H}}_{SPDC}(t)\right], \tag{1.23}$$

such that

$$|\psi\rangle_1 = \hat{\mathcal{U}}\,|\psi\rangle_0\,, \tag{1.24}$$

where $|\psi\rangle_0$ and $|\psi\rangle_1$ are the initial and final two-photon states, respectively. Applying the first-order time-dependent perturbation theory (**4.**), the unitary transformation (1.23) simplifies to the identity operator $\hat{\mathbb{1}}$ plus an effective Hamiltonian term $\hat{\mathcal{H}}_{eff}$:

$$\hat{\mathcal{U}} \approx \hat{\mathbb{1}} - \frac{i}{\hbar}\int_{-\infty}^{\infty} dt\ \hat{\mathcal{H}}_{SPDC}(t) = \hat{\mathbb{1}} + \hat{\mathcal{H}}_{eff}. \tag{1.25}$$

The effective Hamiltonian is

$$\hat{\mathcal{H}}_{eff} \propto \int_{-\infty}^{\infty} dt \int_{-L/2}^{L/2} dz \int d\omega_p d\omega_s d\omega_i\ \chi^{(2)}\alpha(\omega_p)\ \mathrm{e}^{-i\Delta\omega t}\mathrm{e}^{i\Delta k(\omega_p,\omega_s,\omega_i)z}\ \hat{a}_s^\dagger(\omega_s)\ \hat{a}_i^\dagger(\omega_i) + h.c., \tag{1.26}$$

where $\Delta\omega = \omega_p - \omega_s - \omega_i$ is the frequency (energy[2]) mismatch, and $\Delta k(\omega_p,\omega_s,\omega_i) = k_p(\omega_p) - k_s(\omega_s) - k_i(\omega_i)$ is the momentum (phase[3]) mismatch. k_x is the momentum component in the propagation direction. In the collinear case, k_x is the wavenumber, with $k_x(\omega) = \frac{\omega_x}{c}n(\omega_x)$, where $c/n(\omega_x)$ is the speed of light at angular frequency ω_x, in a medium characterized by refractive index n.

It is worth noticing that we did not impose the condition of energy or momentum conservation, but they are intrinsically contained in Eq. (1.26). Indeed, time integration stores the energy conservation condition,

$$\int_{-\infty}^{+\infty} dt\ e^{i(\omega_p-\omega_s-\omega_i)t} = 2\pi\ \delta(\omega_p - \omega_s - \omega_i), \tag{1.27}$$

[2]Photon energy: $E = \hbar\omega$, with $\hbar$ the reduced Plank constant.
[3]Photon phase: $\varphi = kL$, with L the medium length.

which allows removing the dependence on one optical frequency, e.g., ω_p, in $\hat{\mathcal{H}}_{eff}$.

$$\hat{\mathcal{H}}_{eff} \propto \int d\omega_s d\omega_i \; \alpha(\omega_s + \omega_i) \int_{-L/2}^{L/2} dz \; \chi^{(2)} \; \exp\left[i\Delta k(\omega_s, \omega_i) z\right] \; \hat{a}_s^\dagger(\omega_s) \; \hat{a}_i^\dagger(\omega_i) + h.c. \tag{1.28}$$

The integration in the spatial coordinate leads to the phase matching (PM) function $\phi(\omega_s, \omega_i)$, which is representative of momentum conservation:

$$\phi(\omega_s, \omega_i) \propto \int_{-L/2}^{L/2} dz \; \chi^{(2)} \; \exp\left[i\Delta k(\omega_s, \omega_i) z\right] \propto L \; \mathrm{sinc}\left(\frac{\Delta k L}{2}\right). \tag{1.29}$$

If the crystal is infinitely long, only perfect PM is admitted, i.e., $\phi(\omega_s, \omega_i) \to \delta(\Delta k(\omega_s, \omega_i))$. However, if the crystal length is finite, bands with $\Delta k \neq 0$ are admitted. Indeed, $\phi(\omega_s, \omega_i)$ derives from the integration over the coordinate z of the phasor contributions $\tilde{y} = \mathrm{sign}(\chi^{(2)}) \mathrm{e}^{i\Delta k z}$. These contributions destructively interfere when they have opposite phase. Completely destructive interference occurs when the phasor makes a complete turn in the complex space. For a finite-length material, such that $z \in [-L/2, L/2]$, $\Delta k \neq 0$ contributions periodically cancel out. Smaller contributions of the momentum mismatch cancel out in longer crystals: longer crystals are required to explore destructive interference. In the limit of an infinitely long crystal, only contributions with $\Delta k = 0$ constructively interfere.

The effective Hamiltonian can be written as

$$\hat{\mathcal{H}}_{eff} = \int d\omega_s d\omega_i \; f(\omega_s, \omega_i) \; \hat{a}_s^\dagger(\omega_s) \; \hat{a}_i^\dagger(\omega_i) + h.c., \tag{1.30}$$

where, up to a normalization constant, $f(\omega_s, \omega_i) = \alpha(\omega_s + \omega_i)\phi(\omega_s, \omega_i)$.

Joint spectral amplitude, joint spectral intensity, and photon spectra

The product between the pump envelope function and the PM function is the joint spectral amplitude (JSA) $f(\omega_s, \omega_i)$, which represents the complex probability amplitude of generating a pair at angular frequencies ω_s and ω_i. Fig. 1.9 graphically shows the JSA as the product of the pump envelope function and the PM function in the two-dimensional space of the signal and idler wavelengths, in the specific case in which these functions are real.

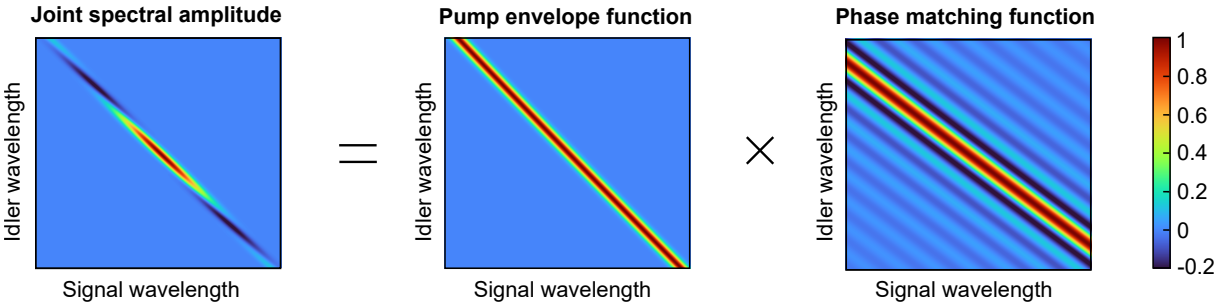

Figure 1.9.: Graphical representation of the joint spectral amplitude as the product between the pump envelope function and the phase matching function, in a specific case in which these quantities are real. All the functions are normalized to their absolute maximum.

The modulus square of the JSA is the joint spectral intensity (JSI), which is the joint probability density that characterizes the spectral correlation of the pair. The signal (idler) spectrum $p_{s(i)}$

can be obtained from the JSI by tracing out the idler (signal) states. As an example, the spectral probability density for the signal is

$$p_s(\omega_s) = \int d\omega_i |f(\omega_s, \omega_i)|^2. \tag{1.31}$$

Fig. 1.10 shows an example for the JSI and the corresponding signal and idler spectra. The source code for such a simulation can be found in Appx. B.1.

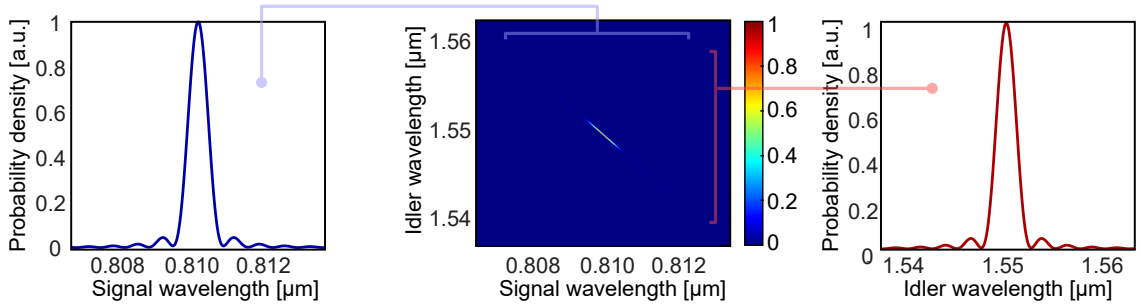

Figure 1.10.: Simulated joint spectral intensity (center) and signal and idler photon spectra (left and right, respectively). The process simulated is a collinear SPDC process in a ppKTP nonlinear crystal with a poling period of 9.668 μm at temperature 73°C, with a pump of central wavelength 532 nm and an FWHM of 5 pm (5.3 GHz). The length of the crystal is 20 mm. All functions are normalized to their absolute maximum.

As the JSI goes as the square modulus of the pump amplitude and the phase matching function, it is straightforward to derive that the probability of generating a signal-idler photon pair grows linearly with the pump power and quadratically with the crystal length.

Photon spectra with a monochromatic pump

In some cases, the bandwidth of the pump envelope function could be much narrower than the bandwidth of the PM function. In this regime, a numerical simulation of the JSI as in Fig. 1.10 could be inefficient, as it requires a fine discretization on a relatively large spectral region. In this case, it is convenient to treat the pump as effectively monochromatic to derive the photon spectra analytically. For a monochromatic pump with angular frequency ω_p, the pump envelope function can be replaced with a delta function:

$$\alpha(\omega) = \delta(\omega - \omega_p). \tag{1.32}$$

It follows that the spectral probability density for the signal is

$$p_s(\omega_s) \propto L^2 \mathrm{sinc}^2 \left[\frac{L}{2} \left(k_p(\omega_p) - k_s(\omega_s) - k_i(\omega_p - \omega_s) \right) \right]. \tag{1.33}$$

Transverse momenta distribution

The Hamiltonian (1.30) takes into account the angular frequency ω and longitudinal momentum k distributions of the modes involved in the SPDC process. In a more refined model, one can also take into account the distribution of the transverse momenta $\boldsymbol{q}$. Such a distribution

becomes relevant when the pump is tightly focused in the crystal: the pump carries a distribution of transverse momenta, and PM is allowed for different signal and idler transverse momenta components. In this case, the effective Hamiltonian, in the same approximations **1.-4.** as for the previous case, is

$$\hat{\mathcal{H}}_{eff}^{\omega,\boldsymbol{q}} \propto \int dt \int d^3r \int d\boldsymbol{q}_p d\boldsymbol{q}_s d\boldsymbol{q}_i \int d\omega_p d\omega_s d\omega_i \, \zeta(t,\boldsymbol{r},\omega_p,\omega_s,\omega_i,\boldsymbol{k}_p,\boldsymbol{k}_s,\boldsymbol{k}_i)\hat{a}_s^\dagger(\omega_s,\boldsymbol{q}_s)\hat{a}_i^\dagger(\omega_i,\boldsymbol{q}_i) + h.c. \tag{1.34}$$

with

$$\zeta(t,\boldsymbol{r},\omega_p,\omega_s,\omega_i,\boldsymbol{k}_p,\boldsymbol{k}_s,\boldsymbol{k}_i) = \chi^{(2)}\,\alpha(\omega_p)\,\xi(\boldsymbol{q_p})\,\mathrm{e}^{-i\Delta\omega t}\,\mathrm{e}^{i\Delta k z}\,\mathrm{e}^{i(\Delta q_x x + \Delta q_y y)}, \tag{1.35}$$

where $\boldsymbol{k} = (k, \boldsymbol{q})$ is the momentum vector, and $\Delta\omega$, Δk, and Δq_j are the angular frequency mismatch, the longitudinal momentum mismatch, and the j-component of the transverse momentum mismatch, respectively. $\alpha(\omega_p)$ is the spectral amplitude of the pump, and $\xi(\boldsymbol{q_p})$ is the pump transverse momenta distribution amplitude.

I consider the following:

i. As before, time integration leads to the energy conservation condition:

$$\int_{-\infty}^{\infty} dt \, \exp\left[-i(\omega_p - \omega_s - \omega_i)t\right] \propto \delta(\omega_p - \omega_s - \omega_i). \tag{1.36}$$

I use the relation (1.36) to remove the integration over the idler angular frequencies, i.e., $\omega_i = \omega_p - \omega_s$.

ii. For simplicity, I assume the case of a monochromatic pump beam, i.e., $\alpha(\omega) = \delta(\omega - \omega_p)$.

iii. The pump transverse momenta distribution $\xi(\boldsymbol{q}_p)$, assuming that the pump is a Gaussian beam with beam waist w_p positioned at the crystal center, is [50]

$$\xi(\boldsymbol{q}_p) \propto \exp\left(-\frac{\left|\boldsymbol{q}_p\right|^2 w_p^2}{4}\right). \tag{1.37}$$

iv. Assuming that the crystal cross-section is wide enough, the integration in the transverse spatial coordinate $\boldsymbol{x} = (x, y)$ allows for perfect momentum matching only in the transverse components:

$$\int_{-\infty}^{\infty} d\boldsymbol{x} \;\; \exp\left[i(\boldsymbol{q}_p - \boldsymbol{q}_s - \boldsymbol{q}_i)\boldsymbol{x}\right] \propto \delta(\boldsymbol{q}_p - \boldsymbol{q}_s - \boldsymbol{q}_i). \tag{1.38}$$

Integrating over the spatial transverse components, I remove the dependence on $\boldsymbol{q}_p$, i.e., $\boldsymbol{q}_p = \boldsymbol{q}_s + \boldsymbol{q}_i$.

v. The integration over the propagation coordinate z gives the PM function

$$\phi(\omega_p, \omega_s, \boldsymbol{q}_s, \boldsymbol{q}_i) \propto \mathrm{sinc}\left(\frac{\Delta k L}{2}\right) \tag{1.39}$$

with Δk depending on the pump single frequency ω_p, the signal frequencies ω_s, and the signal and idler transverse momenta component $\boldsymbol{q}_s$ and $\boldsymbol{q}_i$:

$$\begin{aligned}\Delta k = \sqrt{\left(\frac{\omega_p}{c} n(\omega_p)\right)^2 - |\boldsymbol{q}_i + \boldsymbol{q}_s|^2} - \sqrt{\left(\frac{\omega_s}{c} n(\omega_s)\right)^2 - |\boldsymbol{q}_s|^2} + \\ - \sqrt{\left(\frac{\omega_p - \omega_s}{c} n(\omega_p - \omega_s)\right)^2 - |\boldsymbol{q}_i|^2}\end{aligned} \tag{1.40}$$

The simplified Hamiltonian is therefore [50]:

$$\hat{\mathcal{H}}_{eff}^{\omega,\boldsymbol{q}} \propto \int d\boldsymbol{q}_s\, d\boldsymbol{q}_i \int d\omega_s \, \exp\left(-|\boldsymbol{q}_s + \boldsymbol{q}_i|^2 w_p^2\right) \, L\mathrm{sinc}\left(\frac{\Delta k L}{2}\right) \hat{a}_s^\dagger(\omega_s, \boldsymbol{q}_s)\hat{a}_i^\dagger(\omega_p - \omega_s, \boldsymbol{q}_i) + h.c., \tag{1.41}$$

In Eq. (1.41), the term

$$f^{\omega,\boldsymbol{q}}(\omega_s, \omega_p, \boldsymbol{q}_s, \boldsymbol{q}_i) = \exp\left(-|\boldsymbol{q}_s + \boldsymbol{q}_i|^2 w_p^2\right) \, L\mathrm{sinc}\left(\frac{\Delta k L}{2}\right) \tag{1.42}$$

is the probability amplitude of generating a pair with angular frequencies ω_s and $\omega_p - \omega_s$, and transverse momenta components $\boldsymbol{q}_s$ and $\boldsymbol{q}_i$. The square modulus of this quantity is the corresponding probability density. Integrating over the idler transverse momenta components $\boldsymbol{q}_i$, one finds the probability density $p^{\omega,\boldsymbol{q}}(\omega_s, \omega_p, \boldsymbol{q}_s)$ of having a signal photon at frequency ω_s with transverse momentum component $\boldsymbol{q}_s$, for a pump at frequency ω_p.

$$p^{\omega,\boldsymbol{q}}(\omega_s, \omega_p, \boldsymbol{q}_s) = \int d\boldsymbol{q}_i \, |f^{\omega,\boldsymbol{q}}(\omega_s, \omega_p, \boldsymbol{q}_s, \boldsymbol{q}_i)|^2. \tag{1.43}$$

Fig. 1.11 shows a simulation for this probability density. The original code for the simulation can be found in Appx. B.2. To show the results of the simulation in a surface plot, Fig. 1.11 shows $p^{\omega,\boldsymbol{q}}$ at constant ω_p, and constant transverse component $q_{s,y} = 0$. Two branches are visible, one for the signal frequencies (right) and one for the idler frequencies (left). The simulation shows the results for a collinear non-degenerate generation case. Indeed, the stronger components of the momentum are obtained at $q_{s,x} = 0$, at different frequencies for the idler and the signal.

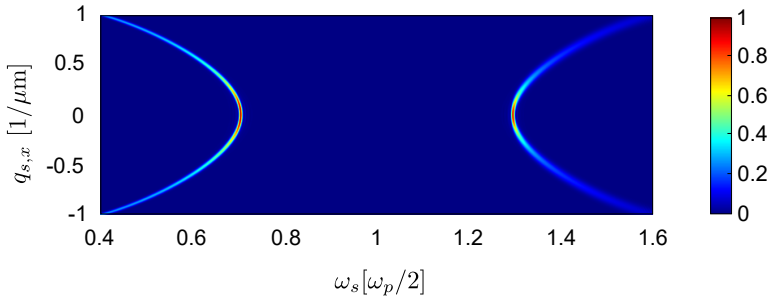

Figure 1.11.: Simulation for the transverse momentum and spectral probability density, normalized to its absolute maximum. The process simulated is an SPDC process in a ppKTP nonlinear crystal with a poling period of 9.675 μm at temperature 25°C, with a monochromatic pump of wavelength 532 nm. The length of the crystal is 3 mm, and the pump waist at the crystal center is 20 μm.

The simulation reported in Fig. 1.11 is useful to illustrate the typical result of a simulation based on the model described by Eq. (1.41), since it exhibits an appreciable contribution in the non-zero components of the transverse momentum. However, this thesis focuses on processes characterized by a smaller momenta distribution, which exhibit a less interesting shape. A few examples of the kind of processes that are of interest in this thesis are shown in Figs 1.12 and 1.13. In Fig. 1.12, a process in which the generated photons do not exhibit a strong spectral dependence in their momenta distribution can be observed. At each transverse momentum component, the signal and the idler exhibit the sinc-squared spectral distribution typical of an SPDC process.

In Fig. 1.13, I show the dependence of the probability density on the crystal length and the pump focusing, for the signal branch. By comparing the panels in Fig. 1.13, it can be observed

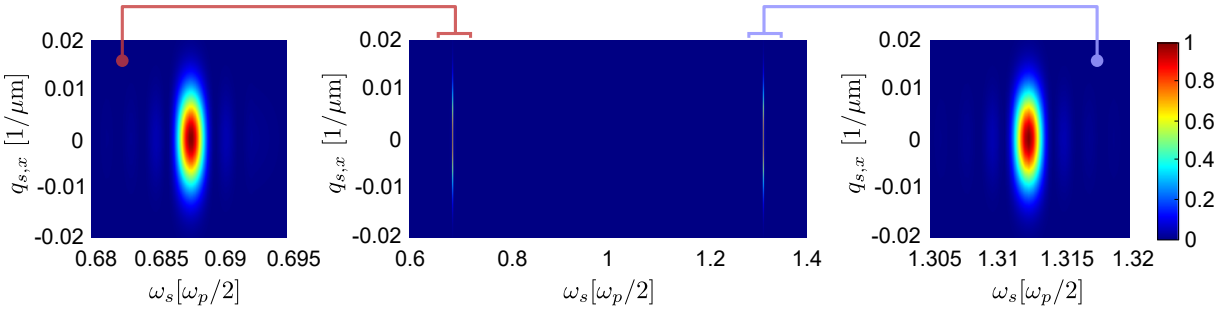

Figure 1.12.: Transverse momentum and spectral probability density in a collinear case. (Center) Full simulation. The simulated process is an SPDC process in a ppKTP nonlinear crystal with a poling period of 9.668 μm at temperature 73°C, with a monochromatic pump of wavelength 532 nm. The length of the crystal is 10 mm, and the pump waist at the crystal center is 150 μm. Due to the length of the crystal, signal and idler are generated with a narrow spectrum. (Left) [(Right)] Magnified view on the idler [signal] branch.

that collinear processes with the same pump focusing condition exhibit the same transverse momenta distribution, while a tighter pump waist w_p in the crystal leads to a broader momenta distribution. For longer crystals, the spectrum is narrower.

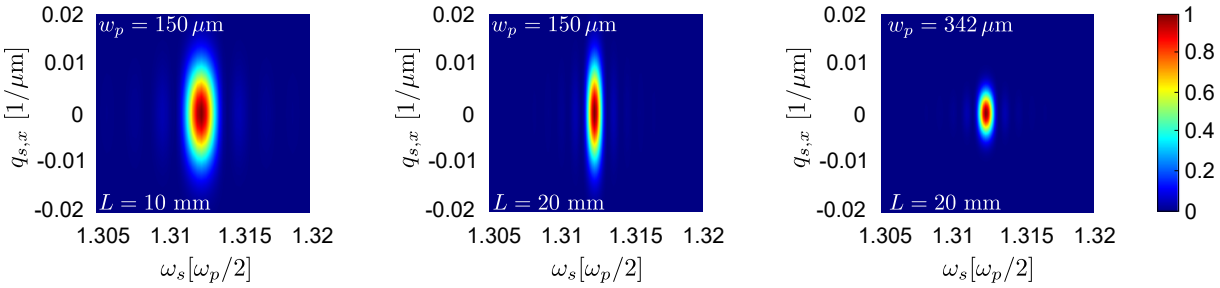

Figure 1.13.: Dependence on the pump focusing and crystal length of the transverse momenta distribution. In this simulation, I considered an SPDC process in a ppKTP nonlinear crystal with a poling period of 9.668 μm at temperature 73°C, with a monochromatic pump of wavelength 532 nm. L: crystal length. w_p pump waist at the crystal center.

Spatial distribution

Rather than in the momenta distribution, one could be interested in the spatial distribution of the generated photons at the crystal plane. As an example, one could want to know the spatial distribution of the generated photons to efficiently couple the generated photons with another optical system. An approachable method is to study the JSI, taking into account the complete spatial dependence of the Hamiltonian [51]:

$$\hat{\mathcal{H}}^{r}_{SPDC}(t) = \int d\boldsymbol{r}\ \varepsilon_0 \boldsymbol{\chi^{(2)}} : \hat{\boldsymbol{E}}^{(+)}_p(\boldsymbol{r},t)\ \hat{\boldsymbol{E}}^{(-)}_s(\boldsymbol{r},t)\ \hat{\boldsymbol{E}}^{(-)}_i(\boldsymbol{r},t)\ + h.c. \tag{1.44}$$

The electric field operators are defined as the integral over the positive frequency components of the spatial modes $\hat{U}_\omega(\boldsymbol{r})$:

$$\hat{\boldsymbol{E}}^{(+)}(\boldsymbol{r},t) \propto \int_0^\infty d\omega\, \hat{\boldsymbol{U}}_\omega(\boldsymbol{r}) \mathrm{e}^{-i\omega t}\, \hat{a}_\omega, \tag{1.45}$$

where $\hat{U}_\omega(\boldsymbol{r})$ is the spatial-dependent probability amplitude for the mode at frequency ω. In the following, I consider $\hat{U}_\omega(\boldsymbol{r})$ to be described by the fundamental Gaussian mode at frequency ω

as in Eq. (1.8) [51][4], and I will limit the discussion to the collinear case. With this assumption, the spatial probability density of generating a photon pair mimics a Gaussian beam intensity distribution. In this sense, in the following, I will often refer to the spatial probability for the photon as "beam" or "Gaussian beam". Such a distribution is characterized by the focusing parameter ε, which is a dimensionless parameter that depends on the crystal length L, the beam waist w_0, and the wavenumber k:

$$\varepsilon = \frac{L}{k w_0^2}. \tag{1.46}$$

In general, the pump (p), the signal (s), and the idler (i) are characterized by their individual focusing parameters ε_j, with $j = p, s, i$, respectively. In reference [51], Bennink finds that the JSI is maximum when $\varepsilon_s = \varepsilon_i = \sqrt{2.84\,\varepsilon_p}$, i.e, once the focusing parameter of the pump ε_p is fixed, the signal (idler) probability amplitude propagate as a Gaussian beam characterized by a beam waist that satisfies

$$w_{0s(i)}^2 = \frac{L}{k_{s(i)}\sqrt{2.84\varepsilon_p}}. \tag{1.47}$$

Quasi-phase matching

Previously, I assumed the nonlinear susceptibility $\chi^{(2)}$ to be independent from the propagation direction z. This is not true in general, and a relevant example is the case of quasi-phase matching (QPM).

QPM allows for constructive interference even if the PM condition $\Delta k = 0$ is not satisfied. As discussed before, materials characterized by second-order nonlinearity are non-centrosymmetric, and the sign of the optical susceptibility $\chi^{(2)}$ carries information on their physical orientation. By periodically flipping the sign of $\chi^{(2)}$, i.e., by inverting the orientation of the material, the phasors $\tilde{y} = \text{sign}(\chi^{(2)})\text{e}^{i\Delta kz}$ periodically acquire a π phase in the complex space. Fig. 1.14(a) compares a bulk crystal with a periodically poled (pp) crystal, Fig. 1.14(b) shows the differences in the evolution of the phasors $\tilde{y}$ in the complex space when increasing z, and Fig. 1.14(c) shows the cumulative contribution of the phasors to the phase matching function. Effectively, a poling with period Λ yields an additional momentum contribution $-2\pi/\Lambda$ to the pump, and the poling period can be chosen to compensate for the momentum mismatch. The momentum mismatch in a periodically poled crystal is

$$\Delta k_{pp} = \Delta k - \frac{2\pi}{\Lambda}, \tag{1.48}$$

which allows for constructive build up of the PM function even in the case in which $\Delta k \neq 0$.

SPDC in anisotropic crystals

Anisotropic crystals exhibit refractive indexes that depend on the orientation of the crystal, i.e., photons with different polarization experience different refractive indexes in the material. PM or QPM condition could be satisfied when the pump, the signal, and the idler do not share the same polarization, and their relative polarization characterizes different SPDC processes. There are three types of SPDC in anisotropic crystals:

[4] In ref. [51], the fundamental Gaussian beam is written as a function of the curvature parameter $q(z) = \omega_0^2 + \frac{2iz}{k}$. The standard form as in Eq. (1.8) is found considering that the relation between the radius and the parameter q is $w(z) = \sqrt{\mathbb{R}\text{e}(q(z))}$.

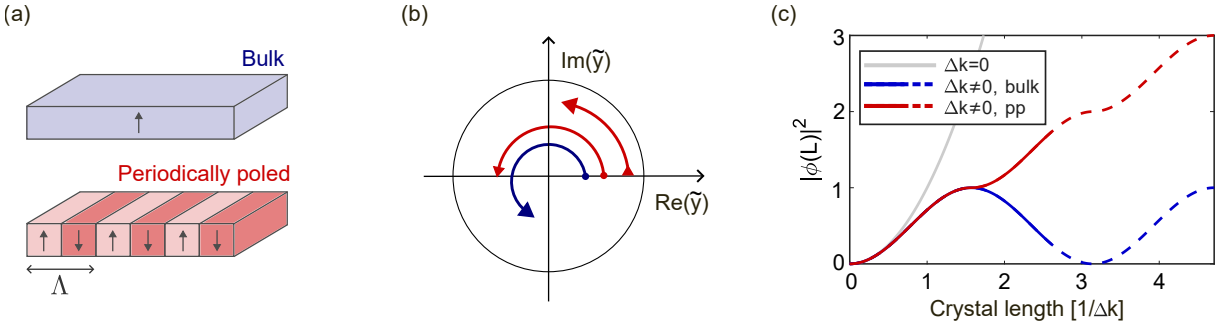

Figure 1.14.: Contribution to the phase matching function for unmatched phases in a bulk (blue) crystal and in a periodically poled crystal (red). (a) Schematics of a bulk (top) and of a periodically poled (bottom) crystal. The vertical arrows indicate the orientation of the second-order nonlinearity. Λ is the poling period of the periodically poled crystal. (b) Representation of the evolution of the phasors $\tilde{y}$ in the case $\Delta k \neq 0$. Dots: starting point; arrows: direction. In a bulk crystal, the phasor evolution in the crystal length causes destructive interference of the generated waves. In a periodically poled crystal, the poling period is chosen such that the waves constructively interfere inside the crystal. (c) Modulus square of the phase matching function in the case of perfect phase matching (gray) and in the case of $\Delta k \neq 0$ in a bulk and periodically poled nonlinear crystal.

- Type 0: the pump, the signal, and the idler share the same polarization. This is the process discussed in this thesis.
- Type I: the signal and the idler share the same polarization, which is orthogonal to the pump polarization.
- Type II: the signal and the idler have orthogonal polarization.

SPDC in this work

In this thesis, I used a 20 mm long ppKTP nonlinear crystal to generate signal and idler photon pairs via collinear type-0 SPDC. Specifically, the nonlinearity exploited in this process is along a principal axis characterized by the tensor component $d_{33} = 16.9$ pm/V of the second-order susceptibility ($\boldsymbol{\chi}^{(2)}$). The pump wavelength is 532 nm, and the expected signal and idler central wavelengths are 810 nm and 1550 nm, respectively. All these wavelengths lie in the transparency range of the KTP (0.4-3 μm) [52]. Phase matching is met at temperature 73°C, with a poling period Λ of 9.668 μm. The bandwidth $\Delta\nu$ of the pump is not provided by the constructor, who provides the lower bound for its coherence length to be $\mathcal{L}_{\text{coh}} > 100$ m. The coherence length and the spectral bandwidth are related as [53]

$$\mathcal{L}_{\text{coh}} = \frac{c}{\Delta\nu}. \tag{1.49}$$

The lower bound on the coherence length corresponds to an upper bound to the pump bandwidth 3 MHz, which is approximately 3×10^{-6} nm at the pump wavelength. A simulation of the JSI by using such a narrow pump bandwidth cannot be performed within a reasonable time with the numerical simulation detailed in Appx. B.1. However, photon spectra can be derived by treating the pump as monochromatic. Specifically, the signal spectrum can be derived by means of Eq. (1.33), with a correction to the momentum mismatch due to the periodically poled structure. The equation for the signal probability density for a quasi-phase matched crystal is

$$p_s(\omega_s) \propto L^2 \text{sinc}^2 \left[\frac{L}{2} \left(k_p(\bar{\omega}_p) - k_s(\omega_s) - k_i(\bar{\omega}_p - \omega_s) - \frac{2\pi}{\Lambda} \right) \right]. \tag{1.50}$$

I simulated the signal and idler spectra for the process of interest in this thesis. The resulting bandwidth is 327 GHz, which corresponds to 0.716 nm at 810 nm in wavelength and 2.6 nm at 1550 nm. From an experimental characterization, shown in Chap. 4, it results that the bandwidth of the generated photons is 400±21 GHz, which is comparable with the simulated value. The discrepancy between the simulated and experimental results can be attributed to deviations in the crystal parameters, which affect the phase-matching condition. Nevertheless, a precise simulation of the bandwidth of the generated photons is beyond the scope of this thesis. A simulation of the JSI for the generation process of interest in this thesis with a broader pump spectrum has been shown in Fig. 1.10. In this work, the pump is a Gaussian beam with a waist of 342 μm positioned at the crystal center. The simulation for the transverse momenta components in this case is the one shown in the right panel in Fig. 1.13. The processes of interest in this thesis are collinear and exhibit a transverse momenta distribution that has a weak dependence on the photon spectra. Regarding the spatial distribution, the signal and idler waists that satisfy Eq. (1.47) are 113 μm and 156 μm, respectively.

1.2.2. Spontaneous four-wave mixing

Spontaneous four-wave mixing (SFWM) is a third-order nonlinear optical process in which two pump photons, at frequencies ω_{p_0} and ω_{p_1}, spontaneously annihilate to create a signal-idler pair at angular frequencies ω_s and ω_i, respectively. It is the spontaneous version of FWM, in which the pumps interact in the nonlinear material with a seeding signal beam. As for the case of SPDC, SFWM requires a quantum treatment to be modeled.

I assume the following conditions to be valid:

1. The process is collinear, z is the propagation direction, and the material has a length L.
2. The probability for SFWM to occur is low enough to apply the first-order perturbation theory, similarly to how I treated the SPDC case.
3. The pumps, p_0 and p_1, can be treated as classical beams.

The Hamiltonian for the collinear (**1.**) SFWM process is

$$\hat{\mathcal{H}}_{SFWM}(t) = \int_{-L/2}^{L/2} dz\ \varepsilon_0\ \chi^{(3)} \hat{E}_{p_0}^{(+)}(z,t)\hat{E}_{p_1}^{(+)}(z,t)\hat{E}_{s}^{(-)}(z,t)\hat{E}_{i}^{(-)}(z,t)\ + h.c., \tag{1.51}$$

According to the first-order perturbation theory (**2.**), the unitary transformation associated with the Hamiltonian (1.51) can be approximated to the identity plus a small perturbative term described by the effective Hamiltonian $\hat{\mathcal{H}}_{eff}$:

$$\hat{\mathcal{U}} = \exp\left[-\frac{i}{\hbar}\int_{-\infty}^{\infty} dt\, \hat{\mathcal{H}}_{SFWM}(t)\right] \simeq \hat{\mathbb{1}} + \hat{\mathcal{H}}_{eff}, \tag{1.52}$$

with

$$\hat{\mathcal{H}}_{eff} \propto \int_{-\infty}^{\infty} dt \int_{-L/2}^{L/2} dz \int d\omega_{p_0} d\omega_{p_1} d\omega_s d\omega_i\, \chi^{(3)}\ \alpha_0(\omega_{p_0})\alpha_1(\omega_{p_1}) \mathrm{e}^{-i\Delta\omega t} \mathrm{e}^{i\Delta k t} a_s^\dagger(\omega_s) a_i^\dagger(\omega_i) + h.c., \tag{1.53}$$

where $\Delta\omega = \omega_{p_0} + \omega_{p_1} - \omega_s - \omega_i$ and $\Delta k = k_{p_0}(\omega_{p_0}) + k_{p_1}(\omega_{p_1}) - k_s(\omega_s) - k_i(\omega_i)$.

As in the SPDC case, the time integration leads to the energy conservation condition, which allows dropping an angular frequency dependence. I choose to remove the dependence on one of the pump frequencies $\omega_{p_1} = \omega_s + \omega_i - \omega_{p_0}$.

The spatial coordinate integration yields to the phase matching function:

$$\phi(\omega_{p_0}, \omega_s, \omega_i) = L \,\mathrm{sinc}\left(\Delta k(\omega_{p_0}, \omega_s, \omega_i)\frac{L}{2}\right). \tag{1.54}$$

The effective Hamiltonian results in

$$\hat{\mathcal{H}}_{eff} = \int d\omega_s d\omega_i \, f(\omega_s, \omega_i)\hat{a}_s^\dagger(\omega_s)\hat{a}_i^\dagger(\omega_i) + h.c., \tag{1.55}$$

where $f(\omega_s, \omega_i)$ is the JSA, with

$$f(\omega_s, \omega_i) \propto \int d\omega_{p_0} \, \alpha_0(\omega_{p_0})\alpha_1(\omega_s + \omega_i - \omega_{p_0})\phi(\omega_{p_0}, \omega_s, \omega_i) \tag{1.56}$$

As before, the modulus square of the JSA is the probability density of generating a pair at frequencies ω_s and ω_s, i.e., the JSI. Since the JSA in Eq. (1.56) depends on the product of the pump amplitudes, it follows that the generation probability density grows quadratically with the pump power. Similarly, it can be derived from the modulus square of Eq. (1.54), that the generation probability grows quadratically with the source length.

Intermodal spontaneous four-wave mixing

In this thesis, I focus on SFWM in two-dimensionally confined guided optical structures. The guided structure allows for exact spatial overlap of the spatial modes, and the maximum efficiency is met when the modes involved in the process, the pumps, the signal, and the idler, share the same spatial mode. This is the case of intramodal SFWM. However, despite the process having a good efficiency due to the precise overlap between the optical modes, the phase matching condition in Eq. (1.54) is typically satisfied for a process that is not highly non-degenerate in the intramodal case[5].

If the nonlinear optical material used as a source is a multimode waveguide, intermodal SFWM is enabled [55]. Working with the transverse waveguide-mode degree of freedom allows for perfect PM at largely non-degenerate wavelengths. Indeed, the PM condition changes, as different modes experience different effective refractive indexes in the waveguide.

Intermodal spontaneous four-wave mixing in this work

In this thesis, the sources are multimode silicon channel waveguides of cross-section 2 μm $\times$ 0.22 μm and length 7.5 mm. The nonlinear optical process of interest is intermodal SFWM, with spectrally degenerate pumps in the C-band (1530 nm-1565 nm [56]), in the fundamental and first-order TE optical modes. Phase matching is met with the signal in the O-band (1260 nm-1360 nm) in the TE0 optical mode, and the idler approaching the mid-infrared spectral region in the TE1 mode. The wide spectral tunability of this process and the strong non-degeneracy in the generated modes were demonstrated by Signorini et al. in [55]. For this process, the momentum mismatch is

$$\begin{aligned}\Delta k &= k_{p_0}^{TE0}(\omega_{p_0}) + k_{p_1}^{TE1}(\omega_{p_1}) - k_s^{TE0}(\omega_s) - k_i^{TE1}(\omega_i) \\ &= \frac{1}{c}\left(n^{TE0}(\omega_{p_0})\;\omega_{p_0} + n^{TE1}(\omega_{p_1})\;\omega_{p_1} - n^{TE0}(\omega_s)\;\omega_s - n^{TE1}(\omega_i)\;\omega_i\right),\end{aligned} \tag{1.57}$$

[5] As an example, see the source in [54].

where $n^m(\omega)$ is the effective refractive index for the spatial mode m at angular frequency ω. In the intermodal configuration, the mismatch between effective refractive indexes for different mode orders increases with respect to the intramodal case (see Fig. 1.5), allowing for PM at largely non-degenerate frequencies.

Fig. 1.15 reports the experimental characterization of the source. Fig. 1.15(a) shows the tunability of the source and the high non-degeneracy of the generated signal and idler photons. Fig. 1.15(b) shows the signal spectrum at pump wavelength 1550 nm for two nominally identical sources on the same photonic integrated circuit (PIC). The purpose of this figure is to highlight that sources with the same design exhibit consistent performance, demonstrating the repeatability of the design. The same measurement has been performed with pairs of nominally identical sources in four different PICs. The average overlap integral, which characterizes the spectral and brightness indistinguishability of the sources, results in 99.75(6)%.

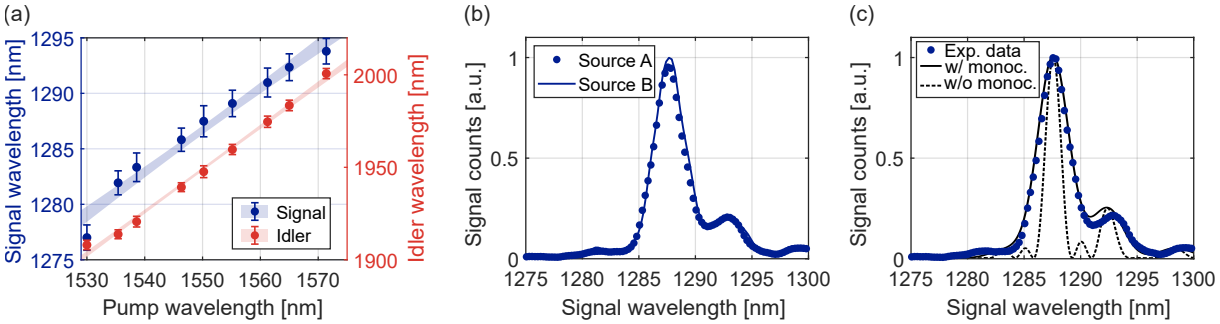

Figure 1.15.: Integrated source characterization. (a) Signal and idler central wavelengths as a function of the pump wavelength. Dots: experimental data. Shaded area: linear regression with its uncertainty. (b) Signal spectra of two nominally identical sources on the same chip. The pump wavelength is 1550 nm. (c) Comparison between the experimental data and the simulation. Dots: experimental data. Dashed line: simulation without including the monochromator. Solid line: simulation convolved with the impulse response of the monochromator.

It can be noticed that the signal spectrum does not exhibit the sinc-squared shape that is typical of a nonlinear optical process. In fact, the integrated sources discussed in this thesis are not straight waveguides but consist of three straight waveguides connected by curves, as it is schematized in Fig. 1.16(a). As it was detailed in Sect. 1.1.2 and in Sect. 1.1.3, the bending waveguides induce a variation in the refractive index experienced by the modes and, consequently, a phase-shift between the propagating modes, as it is represented in Fig. 1.16(b). The phase shift induced by the curves affects the signal spectrum, as I will show in the following. The whole source can be modeled as three sources, labeled with $j = 1, 2, 3$, separated by phase-shifters for the pumps, the signal, and the idler. Between the sources, a phase γ_k is applied to the k-th mode, with $k = p_0, p_1, s, i$.

The unitary transformation that describes this system is

$$\hat{\mathcal{U}} = \prod_{j=1}^{3} \hat{\mathcal{U}}_j, \tag{1.58}$$

where $\hat{\mathcal{U}}_j$ is the unitary transformation for the generation of a pair in the j-th straight waveguide, and it is defined as in Eq. (1.52). Assuming that SFWM has a low probability to occur, the probability for simultaneous generations in different sources can be neglected. Eq. (1.58) can be simplified as

$$\begin{aligned} \hat{\mathcal{U}} &= \hat{\mathbb{1}} + \hat{\mathcal{H}}_{eff,\,1} + \hat{\mathcal{H}}_{eff,\,2} + \hat{\mathcal{H}}_{eff,\,3} \\ &= \hat{\mathbb{1}} + \hat{\mathcal{H}}_{eff}^{tot}, \end{aligned} \tag{1.59}$$

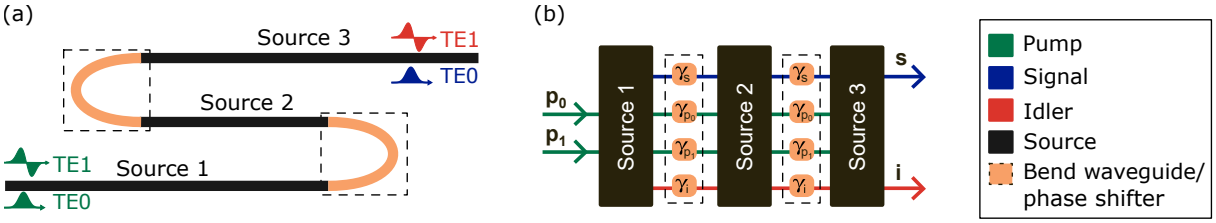

Figure 1.16.: Schematic of the SFWM source employed in this thesis. (a) Schematic of the integrated source, not in scale. The source is composed of three multimode waveguides connected by curves. The structure is fed with the pump optical modes TE0 and TE1, and signal and idler photons are generated in the optical modes TE0 and TE1, respectively. (b) Equivalent model of the source. The source is modeled as three independent nonlinear sources, fed by the pump modes p_0 and p_1. The signal and idler modes are labeled as s and i, respectively. Each bend induces a phase-shift γ_k on the mode $k = p_0, p_1, s, i$.

where

$$\hat{\mathcal{H}}_{eff,\ j} = \int d\omega_s d\omega_i\ f_j(\omega_s, \omega_i) a_s^\dagger(\omega_s) a_i^\dagger(\omega_i) + h.c., \tag{1.60}$$

with $f_j(\omega_s, \omega_i)$ is the JSA for the generation in source j. Therefore, the total effective Hamiltonian $\hat{\mathcal{H}}_{eff}^{tot}$ carries the sum between the complex joint probability amplitudes of generating a pair in one of the sources

$$\begin{aligned} \hat{\mathcal{H}}_{eff}^{tot} &= \int d\omega_s d\omega_i\ \left[f_1(\omega_s, \omega_i) + f_2(\omega_s, \omega_i) + f_3(\omega_s, \omega_i)\right]\ \hat{a}_s^\dagger(\omega_s)\hat{a}_i^\dagger(\omega_i) + h.c. \\ &= \int d\omega_s d\omega_i\ f^{tot}(\omega_s, \omega_i)\ \hat{a}_s^\dagger(\omega_s)\hat{a}_i^\dagger(\omega_i) + h.c., \end{aligned} \tag{1.61}$$

where $f^{tot}(\omega_s, \omega_i)$ is the JSA for the whole system. In the following, I distinguish the cases for a pair to be generated in source $j = 1, 2, 3$. I neglect the propagation losses, and, without loss of generality, I assume the pumps to be characterized by real amplitudes when fed to source 1. To keep the notation light, I will drop the spectral dependence in the JSA, in the pump amplitudes α_0 and α_1, in the phase matching function for the generation in the source j, ϕ_j, in the spectral-dependent phase shift of the modes due to the curves, and in the wavenumber k_j. To derive the total JSA, I distinguish the following cases:

- When a pair is generated in the first source ($j = 1$), the generated signal and idler acquire the propagation phase in sources 2 and 3 and experience the phase shift due to the interaction with two phase shifters (curves).

$$f_1 \propto \int d\omega_{p_0}\ \alpha_0\alpha_1\phi_1 \exp\left[i\left(2\gamma_s + k_s(L_2 + L_3)\right) + i\left(2\gamma_i + k_i(L_2 + L_3)\right)\right]$$

- When the pair is generated in the second source ($j = 2$), the signal and idler carry the phases that the pumps acquired in the propagation through source 1 and the first curve. Then, the photons experience a phase shift due to the second curve, and the phase propagation in source 3.

$$f_2 \propto \int d\omega_{p_0}\ \alpha_0\alpha_1\phi_2 \exp\left[i(\gamma_{p_0} + k_{p_0}L_1) + i(\gamma_{p_1} + k_{p_1}L_1) + i(\gamma_s + k_s L_3) + i(\gamma_i + k_i L_3)\right]$$

- If the pair is generated in the third straight waveguide ($j = 3$), the photons carry the phase that the pumps acquired in their propagation through sources 1 and 2, and due to the two curves.

$$f_3 \propto \int d\omega_{p_0}\ \alpha_0\alpha_1\phi_1 \exp\left[i\left(2\gamma_{p_0} + k_{p_0}(L_1 + L_2)\right) + i\left(2\gamma_{p_1} + k_{p_1}(L_1 + L_2)\right)\right]$$

The JSA for the whole structure is

$$f^{tot}(\omega_s, \omega_i) = f_1(\omega_s, \omega_i) + f_2(\omega_s, \omega_i) + f_3(\omega_s, \omega_i). \tag{1.62}$$

The signal spectrum is obtained by integrating the JSI, i.e., the square modulus of the JSA, over the idler frequencies. In Fig. 1.15(c), I compare a simulation for the signal spectrum with the experimental data. The simulation matches the experimental data when convolved with the impulse response of the monochromator used for acquiring the spectrum, which is a Gaussian function with an FWHM of 2.5 nm.

The case I just presented, in which the JSAs of alternative generation processes interfere, is an example of a nonlinear interferometer. Nonlinear interferometers are of major interest in this thesis, and a particular case will be detailed in Chapter 2.

1.3. Correlation functions: coherence and statistics

As it was already introduced, this thesis discusses an interference phenomenon between the probability amplitudes of photons generated via nonlinear optical processes. Interference is a manifestation of coherence, which can be studied with the first-order correlation function. Additionally, photons generated in a nonlinear optical source are characterized by a statistics that is related to the second-order correlation function. In Sect. 1.3.1, I discuss how the visibility of the interference between two fields and their mutual coherence are related to the first-order correlation. In Sect. 1.3.2, I introduce the relation between the second-order correlation function and the photon statistics.

1.3.1. First-order correlation function

A general expression for the normalized first-order correlation function between two electric fields is [12]

$$g_{12}^{(1)}(\boldsymbol{r}_1, t_1, \boldsymbol{r}_2, t_2) = \frac{\langle \hat{E}_1^{(-)}(\boldsymbol{r}_1, t_1) \hat{E}_2^{(+)}(\boldsymbol{r}_2, t_2) \rangle}{\left(\langle \hat{E}_1^{(-)}(\boldsymbol{r}_1, t_1) \hat{E}_1^{(+)}(\boldsymbol{r}_1, t_1) \rangle \langle \hat{E}_2^{(-)}(\boldsymbol{r}_2, t_2) \hat{E}_2^{(+)}(\boldsymbol{r}_2, t_2) \rangle \right)^{1/2}}, \tag{1.63}$$

where $\hat{E}_j^{(-)}(\boldsymbol{r}_j, t_j) = \mathcal{K} \hat{a}_j^\dagger(\boldsymbol{r}_j, t_j)$ is the field operator that describes the mode j in the spatial coordinate $\boldsymbol{r}_j$, at time t_j, with $\mathcal{K}$ a constant, and $\langle \hat{\circ} \rangle$ is the expectation value of the operator $\hat{\circ}$.

To see how mutual coherence between two fields affects their interference, I consider two electric field operators that are superposed at coordinates $(\boldsymbol{r}, t)$. The resulting operator is

$$\hat{E}^{(-)}(\boldsymbol{r}, t) = \hat{E}_1^{(-)}(\boldsymbol{r}, t)\, \mathrm{e}^{i\phi_1} + \hat{E}_2^{(-)}(\boldsymbol{r}, t)\, \mathrm{e}^{i\phi_2}, \tag{1.64}$$

where the different phases ϕ_1 and ϕ_2 are due to the different propagation paths. The intensity I of the resulting field at coordinates $(\boldsymbol{r}, t)$ is the expectation value of the intensity operator $\hat{E}^{(-)}(\boldsymbol{r}, t) \hat{E}^{(+)}(\boldsymbol{r}, t)$. In the following, I will omit the dependence of the operator on the spatial and temporal coordinates to avoid cluttering the notation.

$$\begin{aligned} I &= \langle \hat{E}^{(-)} \hat{E}^{(+)} \rangle \\ &= \langle \left(\hat{E}_1^{(-)}\, \mathrm{e}^{i\phi_1} + \hat{E}_2^{(-)}\, \mathrm{e}^{i\phi_2} \right) \left(\hat{E}_1^{(+)}\, \mathrm{e}^{-i\phi_1} + \hat{E}_2^{(+)}\, \mathrm{e}^{-i\phi_2} \right) \rangle \\ &= \langle \hat{E}_1^{(-)} \hat{E}_1^{(+)} \rangle + \langle \hat{E}_1^{(-)} \hat{E}_2^{(+)} \rangle \mathrm{e}^{-i\Delta\phi} + \langle \hat{E}_2^{(-)} \hat{E}_1^{(+)} \rangle \mathrm{e}^{i\Delta\phi} + \langle \hat{E}_2^{(-)} \hat{E}_2^{(+)} \rangle \\ &= I_1 + 2 \left| g_{12}^{(1)} \right| \cos(\theta - \Delta\phi) \sqrt{I_1 I_2} + I_2, \end{aligned} \tag{1.65}$$

where I_j is the individual intensity of the field j, and $\Delta\phi = \phi_2 - \phi_1$ is the phase difference. In Eq. (1.65), I used the identities

$$\langle \hat{E}_1^{(-)} \hat{E}_2^{(+)} \rangle = g_{12}^{(1)} \left(\langle \hat{E}_1^{(-)} \hat{E}_1^{(+)} \rangle \langle \hat{E}_2^{(-)} \hat{E}_2^{(+)} \rangle \right)^{1/2} = \langle \hat{E}_2^{(-)} \hat{E}_1^{(+)} \rangle^* \tag{1.66}$$

and

$$g_{12}^{(1)} = \left| g_{12}^{(1)} \right| e^{i\theta}, \qquad \text{where} \quad \theta = \arg\left(g_{12}^{(1)} \right). \tag{1.67}$$

The visibility of the interference is defined as the difference between the maximum in the interference $I_{\max}$ (when $\cos(\theta - \Delta\phi) = 1$) and its minimum $I_{\min}$ ($\cos(\theta - \Delta\phi) = -1$), normalized to their sum. The visibility v is related to the first-order correlation function between the fields $\hat{E}_1$ and $\hat{E}_2$ as

$$v = \frac{I_{\max} - I_{\min}}{I_{\max} + I_{\min}} = \frac{2\left| g_{12}^{(1)} \right| \sqrt{I_1 I_2}}{I_1 + I_2} \leq \left| g_{12}^{(1)} \right| \tag{1.68}$$

That is, the degree of correlation between the fields limits the maximum visibility in the resulting interference pattern. The equality in (1.68) is obtained when $I_1 = I_2$.

1.3.2. Second-order correlation function

The second-order correlation function is [57]

$$g_{12}^{(2)}(\boldsymbol{r}_1, t_1, \boldsymbol{r}_2, t_2) = \frac{\langle \hat{E}_1^{(-)}(\boldsymbol{r}_1, t_1) \hat{E}_2^{(-)}(\boldsymbol{r}_2, t_2) \hat{E}_1^{(+)}(\boldsymbol{r}_1, t_1) \hat{E}_2^{(+)}(\boldsymbol{r}_2, t_2) \rangle}{\langle \hat{E}_1^{(-)}(\boldsymbol{r}_1, t_1) \hat{E}_1^{(+)}(\boldsymbol{r}_1, t_1) \rangle \langle \hat{E}_2^{(-)}(\boldsymbol{r}_2, t_2) \hat{E}_2^{(+)}(\boldsymbol{r}_2, t_2) \rangle}, \tag{1.69}$$

which represents the joint probability of detecting a photon at position $\boldsymbol{r}_1$ and time t_1, and a photon at position $\boldsymbol{r}_2$ and time t_2, normalized by the product of the individual detection probabilities.

The self second-order correlation function gives the information on the statistics of a source. Consider $\hat{E}_1^{(-)}(\boldsymbol{r}_1, t_1) = \hat{E}^{(-)}(\boldsymbol{r}, t) = \mathcal{K} a^\dagger(\boldsymbol{r}, t)$ and $\hat{E}_2^{(-)}(\boldsymbol{r}_2, t_2) = \hat{E}^{(-)}(\boldsymbol{r}, t + \Delta t) = \mathcal{K} a^\dagger(\boldsymbol{r}, t + \Delta t)$, with $\mathcal{K}$ a constant. In this case, the second-order correlation function is [58]

$$g^{(2)}(\Delta t) = \frac{\langle \hat{a}^\dagger(t) \hat{a}^\dagger(t + \Delta t) \hat{a}(t) \hat{a}(t + \Delta t) \rangle}{\langle \hat{a}^\dagger(t) \hat{a}(t) \rangle \langle \hat{a}^\dagger(t + \Delta t) \hat{a}(t + \Delta t) \rangle}, \tag{1.70}$$

The information on the statistics of the source to its degree of second-order coherence is carried by $g^{(2)}(0)$ [59]. Indeed, taking into account the commutation rule for the creation and annihilator operator $\left[a, a^\dagger \right] = 1$, and the definition of the photon number operator $\hat{n}(t) = \hat{a}^\dagger(t) \hat{a}(t)$,

$$g^{(2)}(0) = \frac{\langle \hat{n}(t)(\hat{n}(t) - 1) \rangle}{\langle \hat{n}(t) \rangle^2} = 1 + \frac{\Delta n^2 - \bar{n}}{\bar{n}^2}, \tag{1.71}$$

where $\bar{n} = \langle \hat{n}^\dagger \hat{n} \rangle$ is the average number of photons and $\Delta n^2 = \langle \hat{n}^2 \rangle - \langle \hat{n} \rangle^2$ is the variance. The photon average number and the variance determine the photon statistics: the source is said to be Poissonian when $\Delta n^2 = \bar{n}$, super-Poissonian when $\Delta n^2 > \bar{n}$, and sub-Poissonian if $\Delta n^2 < \bar{n}$. Therefore, depending on the photon statistics, $g^{(2)}(0)$ lies in different regimes. When photons are completely uncorrelated, they exhibit a Poissonian statistics, i.e., $g^{(2)}(0) = 1$. This is the case of coherent light. When photons are generated in bunches, the statistics is super-Poissonian, and $g^{(2)}(0) > 1$, which is the case for single modes generated in a nonlinear optical sources. Sub-Poissonian light manifests an anti-bunching behavior, and $g^{(2)}(0) < 1$.

2. Induced coherence without induced emission

When the joint probability amplitudes of two distinct optical processes interfere, the interferometer is said to be nonlinear [60]. Typically, a nonlinear interferometer resembles a standard interferometer, but beam splitters and mixing elements are replaced with nonlinear parametric amplifiers. Specifically, this thesis focuses on a low-gain nonlinear interferometer that originates a phenomenon that is called "induced coherence without induced emission" [12]. In such a configuration, two distinct identical nonlinear optical sources are pumped. The paths of the identical idler photons are superposed, and, since the sources are identical, they are made indistinguishable. Even though the signal photons are not mutually coherent, interference is observed between the signal from the first and the second sources. Remarkably, the indistinguishability between the generation processes, which is achieved by superposing the paths of the idlers, induces coherence in the signals. Coherence manifests with interference in the signal photon counts [61, 62]. The interference in the signal photon counts occurs despite the fact that the idler photons, which induce the coherence, are never detected, and the process is also referred to as quantum interference with undetected photons in this thesis.

In this chapter, I extensively discuss the experiment of induced coherence without induced emission in different experimental configurations.

2.1. Induced coherence...

Consider the experiment schematized in Fig. 2.1. Two identical sources are pumped. Each source, labeled with $j = 1, 2$, can be described by the unitary transformation[1]

$$\hat{\mathcal{U}}_j = \hat{\mathbb{1}} + \hat{\mathcal{H}}_{eff\,j}, \tag{2.1}$$

with

$$\hat{\mathcal{H}}_{eff\,j} = \iint d\omega_s d\omega_i \, f_j(\omega_s, \omega_i) \hat{a}^\dagger_{s_j}(\omega_s) \hat{a}^\dagger_{i_j}(\omega_i) + h.c., \tag{2.2}$$

where $f(\omega_s, \omega_i)$ is the joint spectral amplitude, and the operator $\hat{a}^\dagger_{k_j}(\omega_k)$ creates a photon with angular frequency ω_k on the spatial mode k_j ($k = s, i$; $j = 1, 2$). Here, I consider the case in which each source generates one signal (s) and one idler (i) mode. The generalized case in which the sources generate multiple spatial modes will be taken into account in Chap. 3.

The tensor product between the unitary transformations for each source describes the generation processes in a single multi-dimensional space. The global transformation is

$$\hat{\mathcal{U}} = \hat{\mathcal{U}}_1 \otimes \hat{\mathcal{U}}_2 \simeq \hat{\mathbb{1}}_1 \otimes \hat{\mathbb{1}}_2 + \hat{\mathcal{H}}_{eff\,1} \otimes \hat{\mathbb{1}}_2 + \hat{\mathbb{1}}_1 \otimes \hat{\mathcal{H}}_{eff\,2} \simeq \hat{\mathbb{1}} + \hat{\mathcal{H}}_{eff\,1} + \hat{\mathcal{H}}_{eff\,2}, \tag{2.3}$$

where the last approximation has been done on the assumption that the probability for simultaneous generations in the two sources is negligible.

[1] Reference [12], which first analyzed this configuration, considers two SPDC sources. However, the discussion can be generalized to the case of SFWM, since Eqs (2.1) and (2.2) describe both SPDC and SFWM.

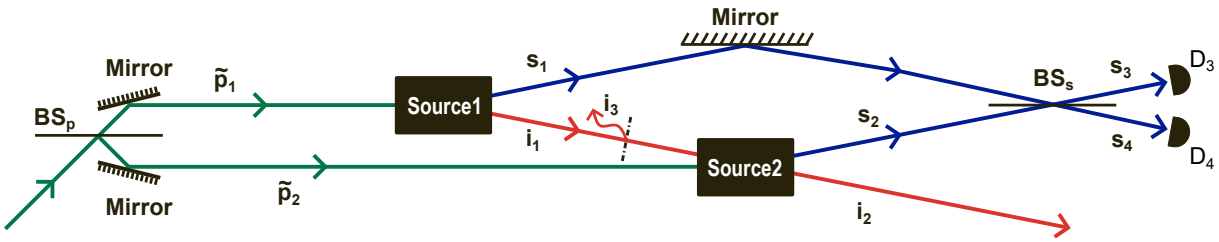

Figure 2.1.: Schematic of an experimental setup for induced coherence without induced emission. Two nonlinear optical sources, source 1 and source 2, are coherently pumped with two classical beams (green) of complex amplitudes $\tilde{p}_1$ and $\tilde{p}_2$. The source j generates two modes, s_j and i_j (blue and red, respectively). The mode i_1 is superposed with the modes i_2 and i_3. The modes s_1 and s_2 are mixed with a beam splitter BS$_s$. At the outputs of BS$_s$, two detectors, D$_3$ and D$_4$, measure the signal photons. Image adapted from [12].

Assuming the crystals to be identical, the phase matching functions $\phi_j(\omega_s, \omega_i)$ are identical for the two sources, and the joint spectral amplitudes differ just due to the contribution of the (complex) pump amplitudes $\tilde{p}_j(\omega_s, \omega_i)$. The joint spectral amplitude is

$$f_j(\omega_s, \omega_i) = \tilde{p}_j(\omega_s, \omega_j)\phi(\omega_s, \omega_i). \tag{2.4}$$

I consider the simplified case in which a single pair of spectral modes are generated at frequencies $\bar{\omega}_s$ and $\bar{\omega}_i$, i.e., $f(\omega_s, \omega_i) \propto \delta(\omega_s - \bar{\omega}_s, \omega_i - \bar{\omega}_i)$, such that

$$\hat{\mathcal{H}}_{eff\,1} = \tilde{p}_1 \hat{a}^\dagger_{s_1} \hat{a}^\dagger_{i_1} + h.c. \tag{2.5}$$

The idler mode i_1 interacts with a beam splitter that models a partially transmissive obstacle:

$$\hat{a}^\dagger_{i_1} = \tilde{t}\hat{a}^\dagger_{i_2} + \tilde{r}\hat{a}^\dagger_{i_3}. \tag{2.6}$$

The mode i_1 is transmitted on the mode i_2, that is the same mode of the photons generated in the second source, with complex probability amplitude $\tilde{t} = t\mathrm{e}^{i\gamma_i}$ $(t \in \mathbb{R})$. Indeed, the path of the idler photons generated in source 1 and source 2 are superposed. The reflected mode i_3 represents idler photons that are lost (absorbed, scattered, ...) due to the interaction with the obstacle. Without loss generality, I assume the probability amplitude for a lost photon to be real, with $\tilde{r} = r = \sqrt{1 - t^2}$. Both the modes i_2 and i_3 are discarded.

Photons in the s_1 and s_2 modes are fed at the inputs of a 50:50 beam splitter (BS$_s$), with output modes s_3 and s_4. Assuming that the reflected modes acquire a $\pi/2$ phase shift, the beam splitter can be modeled as [63]

$$\begin{pmatrix} \hat{a}^\dagger_{s_1} \\ \hat{a}^\dagger_{s_2} \end{pmatrix} = \frac{1}{\sqrt{2}} \begin{pmatrix} 1 & i \\ i & 1 \end{pmatrix} \begin{pmatrix} \hat{a}^\dagger_{s_3} \\ \hat{a}^\dagger_{s_4} \end{pmatrix} \tag{2.7}$$

Considering Eqs. (2.6) and (2.7), the transformation $\hat{\mathcal{U}}$ can be written as

$$\begin{aligned} \hat{\mathcal{U}} &= \hat{\mathbb{1}} + \tilde{p}_1 \hat{a}^\dagger_{s_1} \hat{a}^\dagger_{i_1} + \tilde{p}_2 \hat{a}^\dagger_{s_2} \hat{a}^\dagger_{i_2} + h.c. \\ &= \hat{\mathbb{1}} + \frac{\tilde{p}_1}{\sqrt{2}} \left(\hat{a}^\dagger_{s_3} + i\hat{a}^\dagger_{s_4} \right) \left(t\mathrm{e}^{i\gamma_i} \hat{a}^\dagger_{i_2} + \sqrt{1 - t^2} \hat{a}^\dagger_{i_3} \right) + \frac{\tilde{p}_2}{\sqrt{2}} \left(i\hat{a}^\dagger_{s_3} + \hat{a}^\dagger_{s_4} \right) \hat{a}^\dagger_{i_2} + h.c. \end{aligned} \tag{2.8}$$

I assume the sources to be equally pumped and the pumps to be phase shifted by a phase contribution γ_p, i.e., $\tilde{p}_1 = p$ and $\tilde{p}_2 = \mathrm{e}^{i\gamma_p} p$.

The initial state is the vacuum state, $|\psi_0\rangle = |0\rangle_{s_3} |0\rangle_{s_4} |0\rangle_{i_2} |0\rangle_{i_3} = |00\rangle_s |00\rangle_i$, and the final state $|\psi\rangle$ is

$$|\psi\rangle = \hat{\mathcal{U}} |00\rangle_s |00\rangle_i = |00\rangle_s |00\rangle_i + \tilde{a} |01\rangle_s |01\rangle_i + \tilde{b} |01\rangle_s |10\rangle_i + \tilde{c} |10\rangle_s |01\rangle_i + \tilde{d} |10\rangle_s |10\rangle_i , \quad (2.9)$$

with

$$\tilde{a} = i\tilde{c} = \frac{ip}{\sqrt{2}}\sqrt{1-t^2}, \qquad \tilde{b} = \frac{p}{\sqrt{2}} e^{i\gamma_i} \left(it + e^{i\Delta\gamma}\right), \quad \text{and} \quad \tilde{d} = \frac{p}{\sqrt{2}} e^{i\gamma_i} \left(t + ie^{i\Delta\gamma}\right), \quad (2.10)$$

where $\Delta\gamma = \gamma_p - \gamma_i$.

The density matrix $|\psi\rangle \langle\psi|$, allows calculating the reduced density matrix $\hat{\rho}_s$ by tracing out the idler states, which models the absence of any detector measuring the idler modes:

$$\hat{\rho}_s = \langle 00|_i |\psi\rangle \langle\psi|00\rangle_i + \langle 01|_i |\psi\rangle \langle\psi|01\rangle_i + \langle 10|_i |\psi\rangle \langle\psi|10\rangle_i . \quad (2.11)$$

The probabilities of detecting a signal photon on the spatial modes s_3 and s_4 are

$$\begin{aligned} p_{s_3} &= \langle 10|_s \hat{\rho}_s |10\rangle_s = |c|^2 + |d|^2 = p^2 (1 - t \sin\Delta\gamma) , \\ \text{and} \quad p_{s_4} &= \langle 01|_s \hat{\rho}_s |01\rangle_s = |a|^2 + |b|^2 = p^2 (1 + t \sin\Delta\gamma) . \end{aligned} \quad (2.12)$$

From Eqs (2.12), it derives that the signal counts at detectors D_3 and D_4 exhibit interference with visibility $v = t$, and the interference pattern carries the phase γ_i trough $\Delta\gamma$. The visibility can be derived experimentally by the comparison between the minimum and maximum signal count rate R_s, when varying the phase shift $\Delta\gamma$:

$$v = \frac{\max(R_s) - \min(R_s)}{\max(R_s) + \min(R_s)}. \quad (2.13)$$

Two interesting phenomena occur here. First, single-photon interference occurs between two alternative events that were not generated as mutually coherent. Coherence is induced between the signal modes by superposing the idler photon paths, which makes the sources indistinguishable, even in principle [13]. Second, the interference pattern observed in the signal photon counts carries the information about the object the idler photon interacted with. Indeed, the visibility of the interference is the modulus of the probability amplitude for the transmission of the idler photons, t, and the interference pattern in the signal photon counts is phase shifted by γ_i with respect to a reference interference pattern in which $\gamma_i = 0$. If the object interacting with the idler photon is unknown, its properties (t and γ_i) can be retrieved by detecting photons that never interacted with it. This allows decoupling the probing and the detection stage in any degree of freedom, e.g., their spectral degree of freedom: one can choose a non-degenerate nonlinear optical source such that the idler photon is in a spectral region suitable for the interaction with the object, and the signal photon is in a spectral region where the detection technologies are efficient.

2.2. ...without induced emission

The idler photons generated in the first source do not stimulate the emission in the second source, as was demonstrated by Wang et al. [11]. They calculated the photon emission rate from source 2 in the signal mode and demonstrated (Eq. (22) in [11]) that it does not depend on the idler transmission amplitude $\tilde{t}$. If this were not the case, the approximation in Eq. (2.3) would no longer be valid.

An intuitive way to show that the idler photons generated in source 1 do not act as a seed for the generation SPDC process in source 2 can be based on the work of Liscidini et al. [64]. In their work, they considered a nonlinear optical source pumped and seeded with a mode that matches one of the modes of the SPDC source. In this scenario, both spontaneous and stimulated processes occur. They demonstrated that the ratio between the average photon number for the stimulated process ($N_{\text{stimulated}}$) and the average photon number for the spontaneous process ($N_{\text{spontaneous}}$) is approximately equal to the average photon number of photons in the seed (N_{seed}):

$$\frac{N_{\text{stimulated}}}{N_{\text{spontaneous}}} \simeq N_{\text{seed}} \tag{2.14}$$

Therefore, if source 2 is seeded by the idler photons generated via SPDC, the relation $N_{\text{seed}} \ll 1$ holds, and the stimulated contribution to the emission in source 2 is negligible.

2.3. Maximum distance between the sources

Interference can be observed in the signal photon rates even if the distance between the sources is way longer than the coherence length of the generated photons. In Sect. 2.1, I reproduced a simplified version in which I considered the pump beam to have unlimited coherence length. The coherence length $\mathcal{L}_{\text{coh}}$ and the coherence time $\mathcal{T}_{\text{coh}}$ are limited by the bandwidth $\Delta\nu$ as [53]

$$\mathcal{L}_{\text{coh}} = c\mathcal{T}_{\text{coh}} = \frac{c}{\Delta\nu}, \tag{2.15}$$

where c is the speed of light. However, the limited coherence time of the pump affects the visibility of the interference. Specifically, if τ_1^i is the propagation time from source 1 to source 2 of the idler mode generated in source 1, assuming that the sources are equally pumped, the visibility of the interference is [12]

$$v = t\left|\gamma_{12}(\tau_1^i)\right|, \tag{2.16}$$

with

$$\gamma_{12}(\tau_1^i) = \frac{\langle \tilde{p_1}^*(\tau)\tilde{p_2}(\tau+\tau_1^i)\rangle}{\left(\langle \tilde{p_1}^*(\tau)\tilde{p_1}(\tau)\rangle\langle \tilde{p_2}^*(\tau+\tau_1^i)\tilde{p_2}(\tau+\tau_1^i)\rangle\right)^{1/2}} = \frac{\langle \tilde{p}^*(\tau)\tilde{p}(\tau+\tau_1^i)\rangle}{\langle \tilde{p}^*(\tau)\tilde{p}(\tau)\rangle} \tag{2.17}$$

the mutual coherence function for the pumps between the two generation processes. The time variable here is indicated with τ, as t is the transmittance of the object interacting with the mode i_1.

To observe interference, the distance between the sources must be within the coherence length of the pump. The experimental work conducted in this thesis used pumps characterized by a coherence length that is of the order of hundreds of meters ($\Delta\nu$ <3 MHz), and distances between the sources do not exceed 80 cm. For this reason, the pumps will be considered mutually coherent such that $\left|\gamma_{12}(\tau_1^i)\right| = 1$. However, for other applications, this approximation could not hold.

2.4. Signal and idler relative path length

Another relevant quantity for the interference visibility is the relative path length between the idler and signal photons. Since the propagation length and the propagation time differ by a multiplication constant that is the speed of light, here I will discuss the propagation time difference rather than the path difference. To achieve maximum visibility, it is required that $\tau_1^i = \tau_1^s - \tau_2^s$ [14], where τ_1^i is the propagation time of the idler from source 1 to source 2, and

τ_1^s and τ_2^s are the propagation times of the signal to the detector from source 1 and source 2, respectively. A mismatch between τ_1^i and $\tau_1^s - \tau_2^s$ induces distinguishability between the generation processes and degrades the degree of induced coherence between the signal photons. This occurs due to the temporal correlation between the generated photons in a nonlinear optical source. Assume that a detector for the idler mode i_2 is placed in the setup schematized in Fig. 2.1. The propagation time for the idler generated in source 2 from the source to the detector is τ_2^i, and the propagation time for the idler generated in source 1 from source 1 to the detector is $\tau_1^i + \tau_2^i$. Now consider timing electronics that measure the relative arrival time between the signal and idler photons. The photons generated in source 1 will click at the detectors, yielding a distribution centered at time delay $\tau_1 = \tau_1^s - \tau_1^i - \tau_2^i$, with the standard deviation being the coherence time of the photons. The photons of the pair generated in source 2 will give a distribution centered at $\tau_2 = \tau_2^s - \tau_2^i$, with the same deviation, if the sources are identical. Unless $\tau_1 = \tau_2$, the two generation processes are in principle distinguishable. Therefore, the relative path of the photons must satisfy the condition $\tau_1^i = \tau_1^s - \tau_2^s$.

Fig. 2.2 provides a graphical representation of such distinguishability, depending on the photons' relative path and their coherence time.

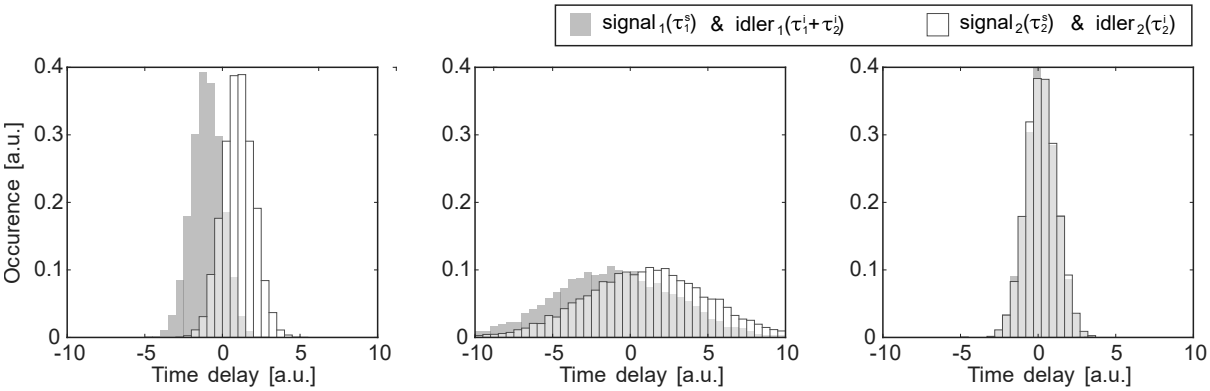

Figure 2.2.: Graphical representation of the dependence of the indistinguishability on the time delays in the setups. These are not experimental data but a graphical explanatory representation. Two identical sources, source 1 and source 2, generate idler and signal photons. The source j generates photons that coincide at time delay τ_j, with $\tau_1 = \tau_1^s - \tau_1^i - \tau_2^i$ and $\tau_2 = \tau_2^s - \tau_2^i$. The histograms represent the occurrence of clicks in the signal detectors and a detector measuring the idler modes. The gray (white) histogram would be obtained with the configuration in Fig. 2.1, with the source 2 (1) removed. (Left) $\tau_1 = -1$, $\tau_2 = 1$. Due to the low coherence time of the signal and the idler, the coincidence peaks are resolvable. Therefore, generations in sources 1 and 2 are not indistinguishable (Center) $\tau_1 = -1$, $\tau_2 = 1$. The coherence time of the photons is long (the spectral bandwidth of the photons is narrow), and the coincidence peaks are not well resolvable. The generation processes in source 1 and source 2 are partially indistinguishable. (Right) $\tau_1 = \tau_2$. The peaks are not resolved, and the processes are indistinguishable.

2.5. Phase shift in all modes

I consider the generic case in which not only the pump and the idler mode i_1, but also the mode s_1 acquires a phase. It is easy to demonstrate (see Appx. A.1.2) that the phases applied to any mode between the sources affect the interference pattern. Intuitively, the joint probability amplitude of generating photons in source 1 carries the phase information of any phase shifter located on the modes s_1 and i_1. On the other hand, the probability amplitude of generating

the photons in source 2 carries the phase of the pump $\tilde{p}_2$[2]. Therefore, the signal counts exhibit interference as in Eq. (2.12), where [15]

$$\Delta\gamma = \gamma_p - \gamma_s - \gamma_i. \tag{2.18}$$

Practically, to retrieve the phase information γ_i of the object interacting with the idler, one can explore the interference pattern in the signal counts by varying the relative phase between the pump and the signal. One expects to observe an interference pattern that is phase-shifted by the amount γ_i with respect to a reference interference pattern obtained in an experimental configuration in which the object is not present ($\gamma_i = 0$). The expected interference patterns for a purely phase object ($\tilde{t} = e^{i\gamma_i}$), for a real object ($\tilde{t} = t$) and in the case of a generic complex object ($\tilde{t} = te^{i\gamma_i}$) are shown in Fig. 2.3.

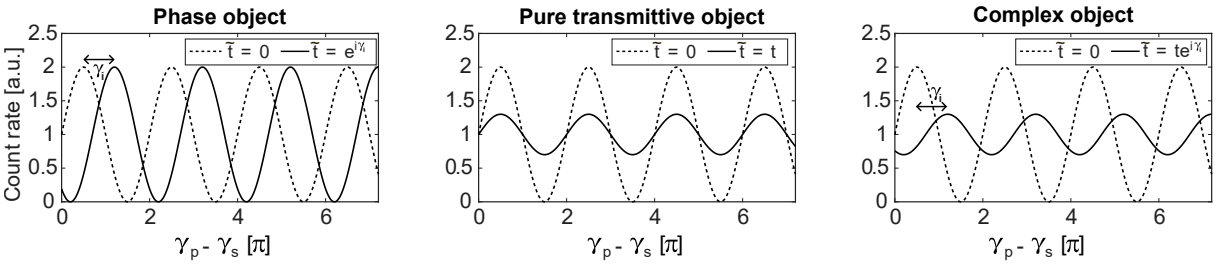

Figure 2.3.: Examples of interference patterns in an experiment of induced coherence without induced emission, for different types of objects interacting with the idler generated in the first nonlinear optical source. Each interferogram (solid line) is compared with a reference interference pattern (dashed line) that reproduces the interference pattern without any object interacting with the idler. (Left) Phase object, i.e., $\tilde{t} = e^{i\gamma_i}$. The interference pattern has maximum visibility and is phase-shifted by γ_i with respect to the reference. (Center) Pure transmitting object, i.e., $\tilde{t} = t$. Only the visibility of the interference is affected. (Right) Complex object, i.e., $\tilde{t} = te^{i\gamma_i}$. The interference pattern has both reduced visibility and is phase-shifted by γ_i with respect to the reference.

2.6. Cascaded and folded configurations

In the configuration discussed above, the signal modes s_1 and s_2 are mixed by means of a beam splitter. However, this superposition can be achieved also by spatially superposing the signal modes [13], as it is schematized in Fig. 2.4(a). In this cascaded configuration, the probability of measuring a signal photon depends on the phase difference between the modes and on the absolute value of the transmittance t of the object interacting with the idler as (see Appx. A.1.1)

$$p_s \propto 1 + t\cos(\Delta\gamma). \tag{2.19}$$

As before, the visibility of the interference pattern, for equally pumped sources, is the transmittance t.

Excluding the object interacting with the idler, the cascaded configuration presents a symmetry [65] such that the setup can be folded on itself, as it is schematized in Fig. 2.4(b). In this configuration, the idler interacts with the object twice, and the interference pattern results in (see Appx. A.1.2)

$$p_s \propto 1 + t^2\cos(2\Delta\gamma), \tag{2.20}$$

[2]If a phase shifter were located on the spatial mode s_2, the joint probability amplitude of generating a photon in source 2 would carry the phase applied to s_2 as well. On the contrary, due to the spatial superposition of modes i_1 and i_2, a phase applied to i_2 is a global phase that does not participate in the interference.

with visibility of the interference $v = t^2$.

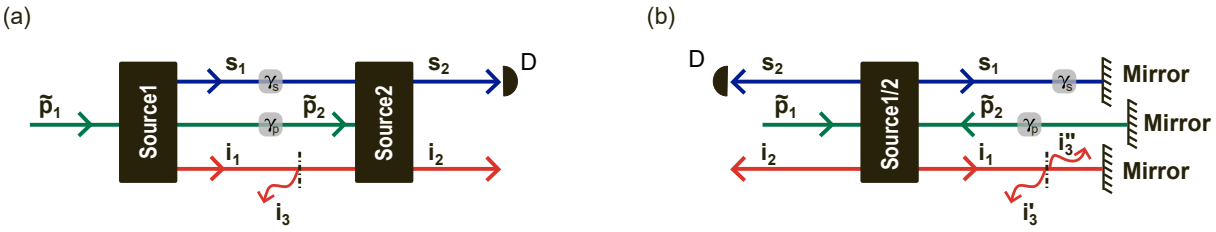

Figure 2.4.: Variations of the schematic of the experimental setup for induced coherence without induced emission. Both configurations employ nonlinear optical sources that, when pumped with a classical pump (green), generate signal (blue) and idler (red) modes. (a) Cascaded configuration. A classical beam with amplitude $\tilde{p}_1$ pumps a nonlinear optical source, and signal and idler are generated in the modes s_1 and i_1, respectively. Photons in the mode s_1 acquire a phase γ_s. A phase γ_p is applied to the residual pump, which is used to pump a second nonlinear source. In the second source are generated the signal and idler modes s_2 and i_2. The idler i_1 interacts with a beam splitter, and the transmitted modes are superposed with i_2. Lost idler modes are labeled as i_3. Photons in the mode s_2 are measured with a photodetector (D). (b) Folded configuration. A classical beam with amplitude $\tilde{p}_1$ pumps a nonlinear optical source from left to right. The modes s_1 and i_1 are generated. A phase γ_p is applied to the residual pump, which is reflected by a mirror. The pump beam interacts again with the phase shifter and pumps the nonlinear source from right to left with complex amplitude $\tilde{p}_2$. The mode s_1 interacts with a phase shifter characterized by γ_s, is reflected by a mirror, and interacts with the phase shifter again, acquiring a global phase $2\gamma_s + \pi$. The idler mode i_1 is transmitted with complex amplitude $te^{i\gamma_i}$. The transmitted mode is reflected by a mirror and experience the interaction with the beam splitter characterized by complex transmittance $te^{i\gamma_i}$. The transmitted modes are superposed with the modes s_2 and i_2, that are the modes generated by the reflected pump from right to left. The lost idler modes in the propagation from left to right are labeled as i_3', and i_3'' from right to left. Photons in the mode s_2 are detected with a photodetector.

2.7. Losses in all modes

Here, I consider a folded configuration in which all modes are subjected to losses [66]. The analysis is restricted to the configuration in which losses affect the interferometer between the first and the second generation processes. Indeed, losses before source 1 and after source 2 do not affect the visibility of the interference pattern. It can be demonstrated (see Appx. A.1.2) that the visibility of the interference pattern is not affected by balanced losses in the signal and pump modes. Indeed, if the mode j, with $j = p, s, i$ for the pump, signal and idler, respectively, interacts with an object characterized by a transmittance with absolute value t_j, the visibility of the interference pattern in the signal counts is

$$v = t_i^2 \frac{2t_s^2 t_p^2}{t_s^4 + t_p^4} \leq t_i^2, \tag{2.21}$$

where the equality holds for $t_s = t_p$.

3. Imaging with undetected photons

In the previous chapter, I discussed induced coherence without induced emission to access a global property of a homogeneous sample. Nevertheless, entangled photon sources exhibit a finite spatial distribution, which can be exploited to obtain a set of information on local properties of the sample in two dimensions, e.g., its image. In fact, the spatial distribution of the idler is correlated with the spatial distribution of the signal, enabling imaging.

Here, I present the application of induced coherence without induced emission to imaging in a scenario in which the interaction of the idler photon with a sample affects the interference on the signal. The position of the signal on a camera is correlated to the position of the idler on the sample, such that the interference pattern is locally affected by the presence on the target, allowing for retrieving its image. In this chapter, I highlight how imaging is enabled by position correlation or momentum anti-correlation and describe the experimental setups that exploit these two regimes in a near-field configuration and a far-field configuration. I show the experimental results I obtained with a far-field configuration that I built exploiting the momentum anti-correlation of a non-degenerate SPDC source. Experimental results are compared with simulations.

3.1. Active imaging

Imaging aims to reconstruct the image of an object. This object is referred to as *source* in passive imaging and *target* in active imaging setups. Indeed, in passive imaging scenarios, the image is typically reconstructed by analyzing the radiation that a source emits[1], while in active imaging applications, a target is probed with light. This thesis deals with active imaging configurations.

An active imaging system can be described by two processes: the interaction between the target and the illuminating beam and the interaction of the beam with a detection device, e.g., a camera. In an ideal system, each point on the target is imaged as a distinct point on the image plane. However, real optical systems are limited such that the object-camera map is not a one-to-one correspondence, which affects the quality of the image. This is characterized by the point spread function (PSF), which is the image of a point-like object as measured by the system. In a linear system[2], knowing the PSF is sufficient to simulate the image reconstruction of a known object. Practically, the PSF is the impulse response of a linear imaging system: for an extended object, each point of the object contributes to the image through the PSF, and each point on the image is the integral of each single-point contribution, i.e., the image is the convolution of the object with the PSF.

The PSF of the imaging system affects the spatial resolution of the image, which refers to the minimum separation between two point-like objects such that their images are distinguishable [67]. According to the Rayleigh criterion for incoherent light[3] [68], two identical point-like

[1] As an example, this is the case of thermal cameras.

[2] A linear system satisfies the properties of homogeneity and additivity [43].

[3] This is the case in this thesis, as the coherence time of the photons used as a probe is shorter than the reciprocal of the photon rate.

objects are just resolved when the maximum of the PSF of the first object lies in the first minimum of the PSF of the second object. For a PSF represented by the Airy function, which is a frequent condition for diffraction-limited systems [53], this happens when the PFSs cross when their value is approximately 1/e of their maximum. In the case of interest, the PSFs are approximated to Gaussian functions, which do not exhibit local minima. This thesis adapts the same criteria as the relevant related work in this field [69, 70], which consider two identically illuminated point-like objects to be just resolved when their PSFs cross when their value is 1/e of their maximum.

The quality of an image can be quantified by the contrast c, which is defined as

$$c = \frac{\max(I) - \min(I)}{\max(I) + \min(I)}, \tag{3.1}$$

where I is the intensity of the measured light, and $\max(I)$, $\min(I)$ denote the maximum and minimum intensity values, respectively.

Fig. 3.1 shows the images and the relative contribution to the total intensity when two point-like objects are resolved (a), just resolved (b) or unresolved (c) for a Gaussian-shaped PSF.

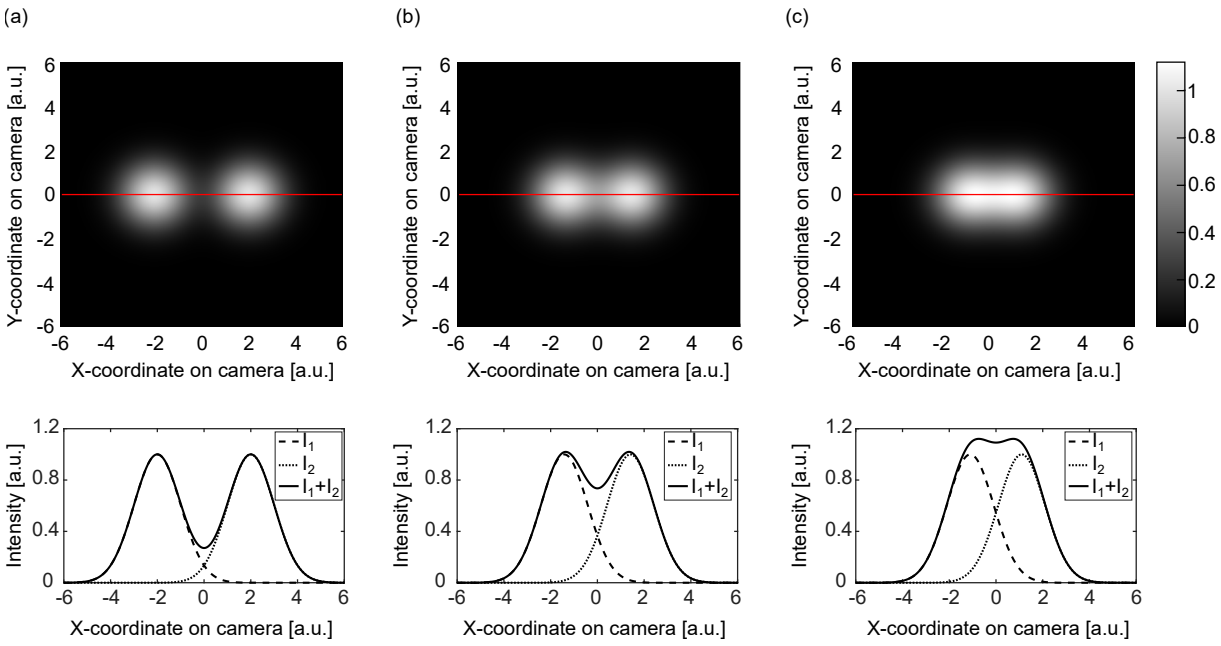

Figure 3.1.: Simulation of imaging of two point-like objects at different relative distances. (top) In gray scale is shown the intensity as a function of the camera coordinates. The red cut line at $y = 0$ indicates the selected area used for the plots at the bottom. (bottom) Intensity as a function of the x-coordinate on the camera along the cutline. The dashed lines show the intensity of the individual objects, I_1 and I_2, and the solid line shows the resulting intensity, that is $I_1 + I_2$ for incoherent sources. The objects are resolved with contrast $c = 0.57$ (a), just resolved with contrast $c = 0.16$ (b), and not resolved, with contrast $c = 0.01$ (c).

Active imaging applications that employ correlated photon pairs, as photons generated via SPDC, allow decoupling the probing phase from the detection phase. The idler interacts with the target, and the signal is detected. When the signal and the idler are highly nondegenerate, employing correlated photon pairs offers the great advantage of a measurement enhanced sensitivity, in which the required trade-off between the detector's efficiency and the sample's spectral responsivity of standard active imaging setups is overcome. However, in this case, intrinsic limi-

tations of the SPDC generation process affect the resolution of the image. In particular, the PSF is determined either by the signal and idler position correlation or momentum anti-correlation.

3.2. Position correlation and momentum anti-correlation

In SPDC, the state $|\psi\rangle$ for a signal-idler pair is characterized not only by a distribution of longitudinal momenta components but also by a transverse momenta distribution, as discussed in Sect. 1.2.1. In the following, I will refer to the transverse momentum component ($\boldsymbol{q}$) simply as "momentum", and the longitudinal component will be indicated with k_z. The signal-idler photon state can be written as the integral over all possible states $|\boldsymbol{q}_s\rangle\,|\boldsymbol{q}_i\rangle$, where each contribution is weighed by their joint transverse-momenta amplitude function $C(\boldsymbol{q}_s, \boldsymbol{q}_i)$, that characterizes the momentum correlation

$$|\psi\rangle = \int d\boldsymbol{q}_s d\boldsymbol{q}_i\, C(\boldsymbol{q}_s, \boldsymbol{q}_i)\,|\boldsymbol{q}_s\rangle\,|\boldsymbol{q}_i\rangle\,. \tag{3.2}$$

A function that affects $C(\boldsymbol{q}_s, \boldsymbol{q}_i)$ is the transverse momenta distribution carried by the pump, which allows phase-matching at different angles [71]. The pump momenta distribution is characterized by the function $\xi(\boldsymbol{q}_p)$. Assuming that the pump is focused in the crystal center and that it carries a Gaussian profile characterized by waist w_p, and considering the momentum conservation condition $\boldsymbol{q}_p = \boldsymbol{q}_s + \boldsymbol{q}_i$, the function ξ is [50]

$$\xi(\boldsymbol{q}_s + \boldsymbol{q}_i) \propto \exp\left(-\frac{1}{4}|\boldsymbol{q}_s + \boldsymbol{q}_i|^2 w_p^2\right). \tag{3.3}$$

According to Eq. (3.3), a pump beam tightly focused carries a broader momenta distribution, as it is characterized by a smaller waist. Therefore, a smaller pump waist in the crystal will lead to a broader joint transverse momenta amplitude function.

Another function that affects the momenta distribution for the generated photons is the phase matching function $\phi(\boldsymbol{q}_s, \boldsymbol{q}_i)$. In the paraxial approximation, the phase matching function can be written as a function of the transverse signal and idler momenta components as

$$\phi(\boldsymbol{q}_s, \boldsymbol{q}_i) \propto L\mathrm{sinc}\left(\frac{\Delta k_z L}{2}\right) = L\mathrm{sinc}\left(\frac{L\lambda_p\lambda_s}{8\pi\lambda_i}\left|\boldsymbol{q}_s - \frac{\lambda_i}{\lambda_s}\boldsymbol{q}_i\right|^2\right), \tag{3.4}$$

where $\Delta k_z L$ is the phase mismatch. For a full derivation of Δk_z as a function of the transverse momenta components, see Appx. A.3.

Therefore, $C(\boldsymbol{q}_s, \boldsymbol{q}_i)$ depends on the pump waist and the crystal length and is found as the product of the pump momenta distribution function and the phase matching function [72]:

$$C(\boldsymbol{q}_s, \boldsymbol{q}_i) = \xi(\boldsymbol{q}_s + \boldsymbol{q}_i)\phi(\boldsymbol{q}_s, \boldsymbol{q}_i) \tag{3.5}$$

The inverse Fourier transform of the joint amplitude function in the transverse-momenta coordinates gives its representation in the transverse-position coordinates $\breve{C}(\boldsymbol{x}_s, \boldsymbol{x}_i)$:

$$\breve{C}(\boldsymbol{x}_s, \boldsymbol{x}_i) \propto \int d\boldsymbol{q}_s d\boldsymbol{q}_i\, C(\boldsymbol{q}_s, \boldsymbol{q}_i)\, \mathrm{e}^{i(\boldsymbol{q}_s\boldsymbol{x}_s + \boldsymbol{q}_i\boldsymbol{x}_i)} \tag{3.6}$$

with $\boldsymbol{x} = (x, y)$ indicating the transverse coordinate.

The square modulus of the joint probability amplitudes $C(\boldsymbol{q}_s, \boldsymbol{q}_i)$ and $\breve{C}(\boldsymbol{x}_s, \boldsymbol{x}_i)$ are the corresponding probability densities, which are measurable quantities. Specifically, $|C(\boldsymbol{q}_s, \boldsymbol{q}_i)|^2$ and

$\left|\breve{C}(\boldsymbol{x}_s, \boldsymbol{x}_i)\right|^2$ are strongly related to the PSF of the imaging system, as it will be detailed in Sects. 3.4 and 3.5. Approximating the sinc function in Eq. (3.4) to a Gaussian function, it follows that [69]

$$|C(\boldsymbol{q}_s, \boldsymbol{q}_i)|^2 = A \exp\left(-\frac{1}{2}|\boldsymbol{q}_s + \boldsymbol{q}_i|^2 w_p^2\right) \exp\left(-\frac{L\lambda_p\lambda_s}{4\pi\lambda_i}\left|\boldsymbol{q}_s - \frac{\lambda_i}{\lambda_s}\boldsymbol{q}_i\right|^2\right) \tag{3.7}$$

and

$$\left|\breve{C}(\boldsymbol{x}_s, \boldsymbol{x}_i)\right|^2 = \breve{A} \exp\left(-\frac{2}{w_p^2(\lambda_s+\lambda_i)^2}|\lambda_s\boldsymbol{x}_i + \lambda_i\boldsymbol{x}_s|^2\right) \exp\left(-\frac{4\pi}{L(\lambda_s+\lambda_i)}|\boldsymbol{x}_s - \boldsymbol{x}_i|^2\right), \tag{3.8}$$

where A and $\breve{A}$ are normalization constants such that

$$\iint |C(\boldsymbol{q}_s, \boldsymbol{q}_i)|^2 d\boldsymbol{q}_s d\boldsymbol{q}_i = 1 \qquad \text{and} \qquad \iint \left|\breve{C}(\boldsymbol{x}_s, \boldsymbol{x}_i)\right|^2 d\boldsymbol{x}_s d\boldsymbol{x}_i = 1. \tag{3.9}$$

Whether imaging is enabled by position correlation or momentum anti-correlation depends on the experimental configuration: position correlation and momentum anti-correlation are accessed in a near-field configuration and in a far-field configuration, respectively. Fig. 3.2 schematizes and distinguishes these regimes.

In Fig. 3.2(a), a pair is generated approximately at the same transversal coordinate at the same time. In the **near-field** of the source, the photons of the pair are correlated in position, and they are found approximately at the same transversal coordinate (Fig. 3.2(b)).

In the **far-field** of the source, photons that have been generated in the crystal have been subjected to a spatial evolution that mimics the evolution of a Gaussian beam. The sum of the signal and idler momenta gives the momentum of the parent pump photon, and photons are located in opposite transverse positions[4] (Fig. 3.2(c)).

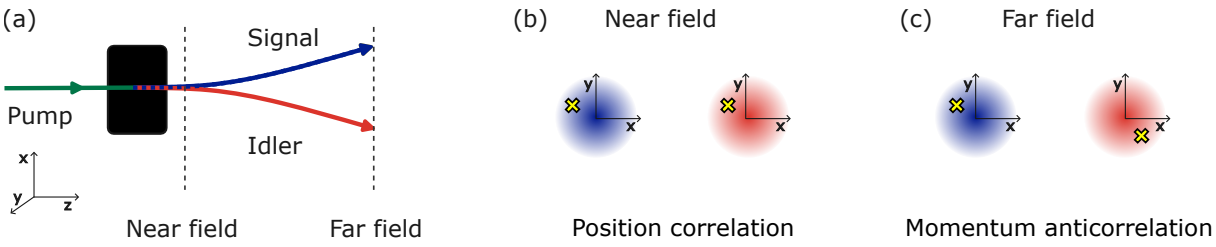

Figure 3.2.: Near-field and far-field in a collinear SPDC source. (a) A pump photon spontaneously annihilates to create a signal-idler pair. In proximity of the source, the photons are correlated in position (near-field). Far from the source, the photons of the pair exhibit anti-correlation in momentum (far-field). (b) Position correlation. The photons of the pair are generated at the same transverse coordinate in the crystal. (c) Momentum anti-correlation. The photons of the pair are generated with opposite transverse components of the momentum, which translates into flipped positions in the far-field regime. The yellow "x"s indicate, as an example, the positions of two correlated (b) or anti-correlated (c) photons.

3.3. Imaging systems

Fig. 3.3 schematizes an imaging system for imaging with undetected photons in a cascaded configuration. To keep the schematic as general as possible, I schematized the imaging system

[4] This is exactly true for a degenerate process. In the non-degenerate case, it must be taken into account that modes at different wavelengths are subject to different divergence, and the size of the signal beam and the size of the idler beam are different.

without any assumption on the spatial distribution of the photon of the pair or the type of correlation exploited for the imaging. For this reason, Fig. 3.3 reports the system as a series of transformations applied to three generic modes, pump, signal, and idler. In the scheme, two identical photon-pair sources are coherently pumped by a classical beam. The idler photon generated in the first source interacts with an extended object of complex transmittance $\tilde{t}$, and to optimize the interaction, the idler spatial distribution is manipulated with the optical system S_i^1, characterized by magnification M_i. The transmitted idler is superposed with the idler mode generated in the second source. To guarantee indistinguishability between the generation processes, the idler photons transmitted by the object are subjected to an optical system S_i^2 with magnification M_i^{-1}. Even though it is not schematized in Fig. 3.3 to maintain clarity to the schematic, indistinguishability must be kept to the signal photons as well, such that if their spatial distribution is manipulated between the sources, it must be restored before being fed into source 2. Similarly, the spatial distribution of the pump when pumping source 1 and source 2 must be identical. Between the sources, the signal and the pump acquire a phase γ_s and γ_p, respectively. To perform imaging, the signal photons are measured with a camera. To optimize the detection stage, the signal photons are magnified through the system S_s, with magnification M_s.

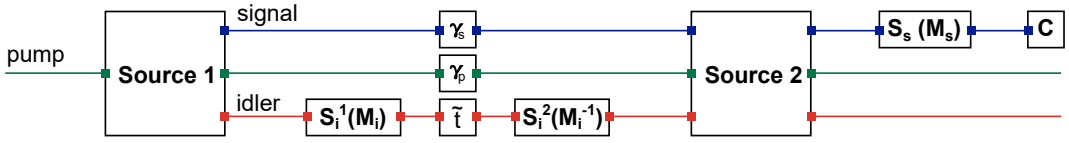

Figure 3.3.: Schematic of an experimental setup for imaging with undetected photons. Source 1 and source 2 are identical systems that, when fed with a pump beam, generate signal and idler photons. The idler generated in source 1 interacts with an imaging system S_i^1, which is characterized by magnification M_i. Then it interacts with a system characterized by complex transmittance $\tilde{t}$. The transmitted photons are fed into the imaging system S_i^2, and superposed with the idler mode generated in source 2. The residual pump from source 1 and the signal mode generated in source 1 acquire a phase γ_p and γ_s, respectively. The signal is superposed with the mode generated in source 2 and is fed into an imaging system S_s with magnification M_s, and is measured with a camera (C).

3.4. Near-field imaging

If imaging is enabled by **position correlation**, the probability $p(\boldsymbol{x}_c)$ of detecting a photon on the camera at the transverse position $\boldsymbol{x}_c$ carries the information on the target complex transmittance at the coordinates $\boldsymbol{x}_t$, weighted with the correlation density function for the signal position on the camera and the idler position on the target. The functions that associate the signal and idler transverse coordinates at the source plane $\boldsymbol{x}_s$ and $\boldsymbol{x}_i$ to the signal coordinates at the camera plane $\boldsymbol{x}_c$ and the idler coordinates at the target plane $\boldsymbol{x}_t$ are determined by the magnifications M_s and M_i of the systems S_s and S_i^1, respectively:

$$\boldsymbol{x}_c = M_s\,\boldsymbol{x}_s \qquad \text{and} \qquad \boldsymbol{x}_t = M_i\,\boldsymbol{x}_i. \tag{3.10}$$

In a near-field configuration, the probability of measuring a signal photon at position $\boldsymbol{x}_c$ on the camera is [73]

$$p(\boldsymbol{x}_c) = \frac{1}{2}\breve{B}\int d\boldsymbol{x}_t \left|\breve{C}\left(\frac{\boldsymbol{x}_c}{M_s},\frac{\boldsymbol{x}_t}{M_i}\right)\right|^2 \{1 + t(\boldsymbol{x}_t)\cos\left[\gamma_p - \gamma_s - \gamma_t(\boldsymbol{x}_t)\right]\}, \tag{3.11}$$

where $\tilde{t}(\boldsymbol{x}_t) = t(\boldsymbol{x}_t)\exp(i\gamma_t(\boldsymbol{x}_t))$ is the complex transmittance at the target coordinate $\boldsymbol{x}_t$, and $\breve{B}$ is a normalization constant

$$\breve{B} = \left[\int d\boldsymbol{x}_t \left|\breve{C}\left(\frac{\boldsymbol{x}_c}{M_s}, \frac{\boldsymbol{x}_t}{M_i}\right)\right|^2\right]^{-1}. \tag{3.12}$$

At the camera coordinate $\boldsymbol{x}_c$, the probability of detecting a signal photon carries the (incoherent) sum of the contribution of the target at a positions $\boldsymbol{x}_t$, weighted by the position correlation density function at the corresponding coordinates on the source plane.

The visibility of the resulting interference at the camera coordinate $\boldsymbol{x}_c$ is

$$v(\boldsymbol{x}_c) = \breve{B}\int d\boldsymbol{x}_t \left|\breve{C}\left(\frac{\boldsymbol{x}_c}{M_s}, \frac{\boldsymbol{x}_t}{M_i}\right)\right|^2 t(\boldsymbol{x}_t). \tag{3.13}$$

If the object is a point-like object located at coordinate $\boldsymbol{x}'_t$, i.e., $t(\boldsymbol{x}_t) \propto \delta^2(\boldsymbol{x}_t - \boldsymbol{x}'_t)$, the visibility of the interference is proportional to the probability density $|\breve{C}(\boldsymbol{x}_c/M_s, \boldsymbol{x}'_t/M_i)|^2$: the probability density function $|\breve{C}(\boldsymbol{x}_s, \boldsymbol{x}_i)|^2$ is intimately connected with the PSF of the imaging system.

A complete derivation of Eqs. (3.11) and (3.13) can be found in [73]. In Appx. A.2, I structure their calculation coherently with the notation of this thesis.

3.4.1. Experimental configuration

An example of setup with imaging with undetected photons in the near-field regime is schematized in Fig. 3.4 [70]. The schematic presents a folded configuration for imaging with undetected photons, in which the same source is employed twice. In such a configuration, two $4f$ imaging systems image the source plane on the target plane (idler) and the camera plane (signal). Indeed, in Fig. 3.4 a nonlinear crystal is pumped from left to right (source 1). Idler and signal propagate and are collimated with the lens L_1 of focal length f_1 (in the following, I will indicate the focal length of any lens L_j as f_j and, unless otherwise specified, the lenses considered are convex lenses). The distance between the source plane and L_1 is f_1. The idler is separated from the pump and the signal with a dichroic mirror, and the source plane is imaged on the target plane with the lens L_t. The distance between L_1 and L_t is $f_1 + f_t$, and the distance between L_t and the target is f_t. The signal photons are imaged on a mirror placed at distance f'_1 from lens L'_1. The distance between L_1 and L'_1 is $f_1 + f'_1$. The signal is reflected by the mirror, and it is imaged on the source plane with magnification equal to 1. The same occurs for the idler transmitted by the target. Similarly, the pump is reflected in the source such that its spatial distribution is kept unchanged with respect to the generation process in source 1. The crystal is pumped from right to left (source 2), and signal and idler photon pairs are generated. Their path is superposed to the path of the pairs generated in source 1. The idler and the pump are discarded, and the signal is imaged on the camera plane with lenses L_2 and L_c. The distance between source 2 and L_2 is f_2, the distance between L_2 and L_c is $f_2 + f_c$, and the distance between L_c and the camera is f_c. Since the optical path of the idler and the signal generated in source 1 must be equal within the signal and idler coherence length (see Sect. 2.4), L'_1 and L_t should be chosen accordingly, such that $f'_1 = f_t$.

On the camera plane, at coordinate $\boldsymbol{x}_c$, are imaged the signal photons generated at position $\boldsymbol{x}_s$ on the source plane, which are correlated through $\breve{C}(\boldsymbol{x}_s, \boldsymbol{x}_i)$ with the idler photons at coordinate $\boldsymbol{x}_i$ on the source plane, which are imaged on the position $\boldsymbol{x}_t$ on the target plane.

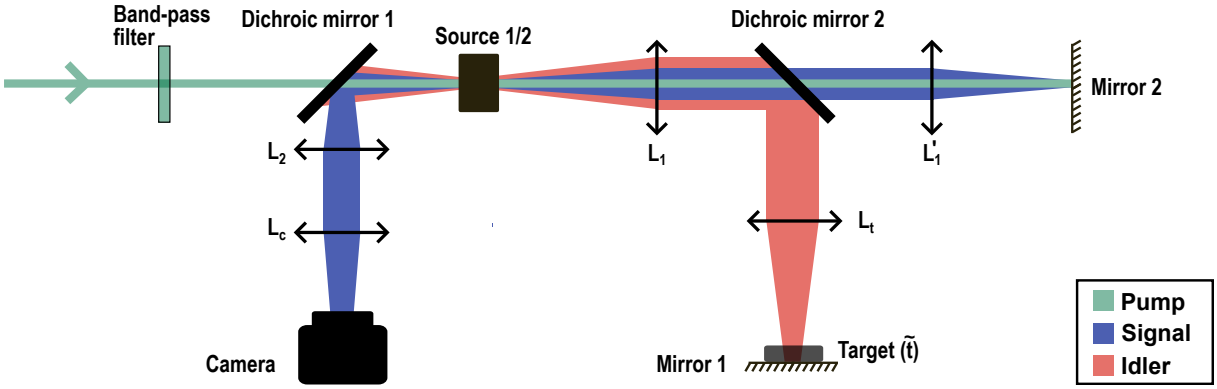

Figure 3.4.: Example of a near-field setup for imaging with undetected photons. L_j: convex lens with focal length f_j. Source 1 (2): signal and idler photon source with generation direction from left (right) to right (left). $L_1 - L_t$: $4f$ imaging system for the idler generated in source 1, such that the idler photons at the source plane are imaged on the mirror labeled as mirror 1. A target with complex transmittance $\tilde{t}$ is positioned on mirror 1. $L_1 - L_1'$: $4f$ imaging system for the signal generated in source 1, such that the signal photons at the source plane are imaged on the mirror labeled as mirror 2. $L_2 - L_c$: $4f$ imaging system for the signal photons, such that the signal photons at the source plane are imaged on the camera plane.

3.4.2. Point spread function, magnification and resolution

A typical near-field imaging setup with SPDC sources employs a large pump waist w_p, such that the condition

$$w_p^2 \gg \frac{\lambda_i L}{4\pi} \tag{3.14}$$

is satisfied. λ_i is the longer wavelength among the generated photons and L the length of the crystal. Under this condition, the joint probability density function for the position correlation $\left|\breve{C}(\boldsymbol{x}_s, \boldsymbol{x}_i)\right|^2$ is strongly dependent on L. Indeed, if the condition (3.14) is satisfied, the term dependent on the pump waist in Eq. (3.8) varies slowly enough with respect to the term dependent on the crystal length to be considered as a constant. Taking into account that the idler photon on the target is magnified with magnification M_i, and the signal on the camera is magnified with magnification M_s, Eq. (3.8) can be written as [73]

$$\left|\breve{C}(\boldsymbol{x}_c, \boldsymbol{x}_t)\right|^2 = \breve{A}' \exp\left(-\frac{4\pi}{L(\lambda_s + \lambda_i)}\left|\frac{\boldsymbol{x}_c}{M_s} - \frac{\boldsymbol{x}_t}{M_i}\right|^2\right) \tag{3.15}$$

with $\breve{A}'$ a normalization constant.

According to Eq. (3.13), the visibility of the image on the camera for a point-like object such that $\tilde{t}(\boldsymbol{x}_t) \propto \delta^2(\boldsymbol{x}_t)$ is its PSF

$$PSF(\boldsymbol{x}_c) = \exp\left(-\frac{4\pi}{L(\lambda_s + \lambda_i)}\frac{|\boldsymbol{x}_c|^2}{M_s^2}\right). \tag{3.16}$$

The minimum resolvable distance σ_c on the camera is found when the PSF drops to 1/e its maximum value, multiplied by a factor of 2 that takes into account the relative position of a second point-like object:

$$\sigma_c = \frac{M_s}{\sqrt{\pi}}\sqrt{L(\lambda_s + \lambda_i)}. \tag{3.17}$$

The corresponding minimum resolvable distance on the target plane, i.e., the system resolution σ, is found by dividing σ_c by the relative magnification between the idler and the signal $M = M_s/M_i$.

$$\sigma = \frac{M_i}{\sqrt{\pi}}\sqrt{L(\lambda_s + \lambda_i)}. \tag{3.18}$$

Consider the experimental setup schematized in Fig. 3.4. The magnifications M_i and M_s are wavelength independent. This can be easily demonstrated applying Eq. (1.14) for the collimation and focusing of Gaussian beams[5]. The resulting magnifications are

$$M_s = \frac{f_c}{f_2} \qquad \text{and} \qquad M_i = \frac{f_t}{f_1}. \tag{3.19}$$

It follows that resolution in near-field imaging setups for imaging with undetected photons is limited by the square root of the crystal length and by the square root of the sum of the generated wavelengths. A smaller magnification on the idler beam in the target plane leads to a smaller minimum resolvable distance, i.e., to better resolution. The choice of M_s does not affect the resolution of the imaging system, and it can be chosen to optimize the spot on the camera size without affecting the resolution.

3.5. Far-field imaging

If imaging is enabled by **momentum anti-correlation**, the optical systems S_i^1 and S_s allows to univocally associate the momenta components $\boldsymbol{q}_s$ and $\boldsymbol{q}_i$ to a position on the camera plane $\boldsymbol{x}_c$ and on the target plane $\boldsymbol{x}_t$, respectively:

$$\boldsymbol{q}_s \xrightarrow{S_s} \boldsymbol{x}_{\boldsymbol{q}_s} = \boldsymbol{x}_c \qquad \text{and} \qquad \boldsymbol{q}_i \xrightarrow{S_i^1} \boldsymbol{x}_{\boldsymbol{q}_i} = \boldsymbol{x}_t. \tag{3.20}$$

In a far-field configuration, the probability of measuring a photon at the camera transverse position $\boldsymbol{x}_c = \boldsymbol{x}_{\boldsymbol{q}_s}$ is the sum of the contribution at the target transverse position $\boldsymbol{x}_t = \boldsymbol{x}_{\boldsymbol{q}_i}$, weighted by the joint momentum correlation density function [74]:

$$p(\boldsymbol{x}_{\boldsymbol{q}_s}) = \frac{1}{2}B \int d\boldsymbol{q}_i \left|C(\boldsymbol{q}_s, \boldsymbol{q}_i)\right|^2 \left\{1 + t(\boldsymbol{x}_{\boldsymbol{q}_i}) \cos\left[\gamma_p - \gamma_s - \gamma(\boldsymbol{x}_{\boldsymbol{q}_i})\right]\right\}. \tag{3.21}$$

The quantity $\tilde{t}(\boldsymbol{x}_{\boldsymbol{q}_i}) = t(\boldsymbol{x}_{\boldsymbol{q}_i}) \exp(i\gamma_t(\boldsymbol{x}_{\boldsymbol{q}_i}))$ is the complex transitivity at the target coordinate $\boldsymbol{x}_c = \boldsymbol{x}_{\boldsymbol{q}_i}$, and B is a normalization constant:

$$B = \left[\int d\boldsymbol{q}_i \left|C(\boldsymbol{q}_s, \boldsymbol{q}_i)\right|^2\right]^{-1}. \tag{3.22}$$

The interference visibility at the camera carries information on the amplitude of the transmittance:

$$v(\boldsymbol{x}_{\boldsymbol{q}_s}) = B \int d\boldsymbol{q}_i \left|C(\boldsymbol{q}_s, \boldsymbol{q}_i)\right|^2 t(\boldsymbol{x}_{\boldsymbol{q}_i}). \tag{3.23}$$

For a full derivation of Eq. (3.21), see Appx. A.2.

[5] According to Eq. (1.14), when focusing (collimating) a collimated (diverging) beam with waist w_0^A, the output beam waist w_0^B in the thin-lens approximation is $w_0^B = (f\lambda)/(\pi w_0^A)$, where f is the focal length of the lens.

3.5.1. Experimental configuration

In this section I present an experimental setup for imaging with undetected photons in a far-field configuration that I designed and implemented experimentally. A schematic of the setup is shown in Fig. 3.5. While the geometry is based on the folded configuration introduced by Kviatkovsky et al. [75], I designed the setup to operate at different wavelengths and at a different pump focusing condition, selecting the appropriate optical components. Then, I built the setup. In this experimental setup, a nonlinear crystal is pumped from left to right (source 1) with a pump Gaussian beam with a wavelength λ_p of 532 nm, which is focused with a lens L_p at the center of the nonlinear crystal with a pump waist w_p of 342 μm. The nonlinear crystal is a ppKTP crystal with a length L of 20 mm. The nominal poling period is 9.675 μm at room temperature. Photons are generated via collinear type-0 SPDC, exploiting the z-axis of the KTP. Phase matching is met at a temperature T of 73°C with signal and idler photons at wavelengths λ_s and λ_i of 810 nm and 1550 nm, respectively. Such a generation process has been extensively discussed in Sect. 1.2.1.

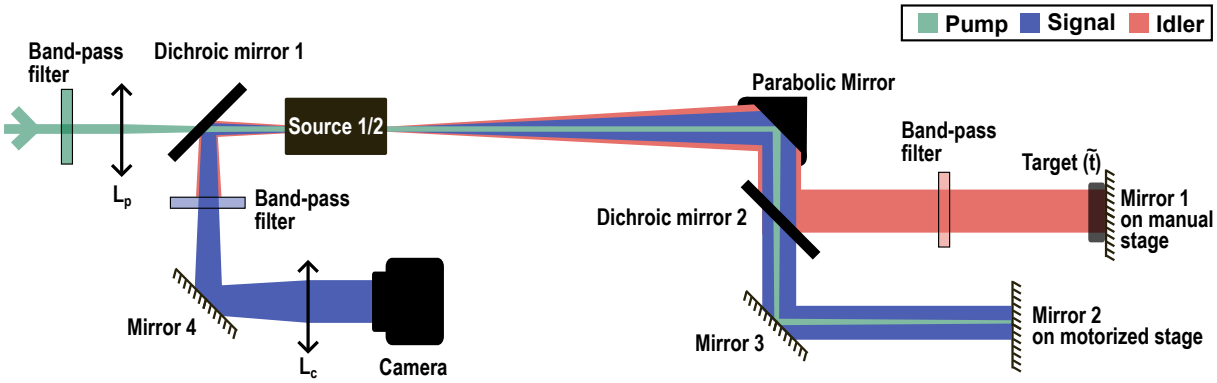

Figure 3.5.: Schematic of the experimental setup used for far-field imaging with undetected photons. L_j: convex lens with focal length f_j. Source 1 (2): signal and idler photon source from left (right) to right (left). The signal and idler transverse momenta components are anti-correlated in the far-field of the source. A target of complex transmittance $\tilde{t}$ is positioned in the far-field of the source, interacting with the idler generated in source 1. The transmitted idler is reflected by a mirror (Mirror 1) and induces coherence in the signal, which is in the far-field of the source and imaged on a single-photon resolving camera (Camera).

Signal and idler are collimated with an off-axis silver-coated parabolic mirror, characterized by a focal length f_{pm} of 200 mm. The distance between the crystal center and the parabolic mirror is f_{pm}, which is in the far field of the source. Indeed, the Rayleigh range for the photons generated in the SPDC source (see Sect. 1.2.1) is

$$z_R = \frac{w_p\sqrt{Lk_p}}{2\sqrt{2.84}} \approx 50 \text{ mm}. \tag{3.24}$$

On the contrary, the pump waist is large enough to consider the pump as collimated. Indeed, the Rayleigh range for the pump is approximately 690 mm. The pump is focused by the parabolic mirror at a distance equal to f_{pm}. The idler is spectrally isolated with a short-pass dichroic mirror (dichroic mirror 2), with a cut-off wavelength of 950 nm. The idler interacts with a target characterized by complex transmittance $\tilde{t}$, and it is back-reflected by a mirror (mirror 1). The distance between the parabolic mirror and mirror 1 is f_{pm}. To avoid back reflection in the residual pump reflected at the dichroic mirror, the spurious pump is suppressed with a band-pass filter centered at a wavelength of 1550 nm and with 40 nm bandwidth. The bandwidth

of the band-pass filter is large enough to not affect the transmission of the idler. The signal and the pump transmitted at the dichroic mirror are reflected by a mirror (mirror 2), which is at distance f_{pm} from the parabolic mirror. Mirror 1 is mounted on a linear translation stage, which allows adjusting its position along the optical axis (travel length of 25 mm, resolution of 10 μm). Similarly, the position of mirror 2 can be adjusted with a motorized translational stage (resolution of 50 nm).
The nonlinear crystal is pumped from right to left (source 2). Signal and idler are separated from the pump with a short-pass dichroic mirror (dichroic mirror 1) with a cut-off wavelength of 650 nm. The spurious reflected pump at the dichroic mirror and the idler are suppressed with two band-pass filters centered at wavelength 810 nm with 10 nm bandwidth. Considering the dichroic mirror and the pass-band filters, the total suppression on the pump is approximately 160 dB. The signal photons are collimated with a lens L_c of focal length f_c. The distance between the source 2 and L_c is f_c. The signal is measured with a single-photon resolving camera positioned at a distance f_c from L_c. In the setup, I varied the focal length f_c, using two lenses with focal lengths of 250 mm and 300 mm. The camera is a CMOS camera with photon-resolving capabilities [76]. The active area of the camera presents 2304 $\times$ 4096 pixels, with a pixel size of 4.6 μm. The quantum efficiency of the camera at the signal wavelength is of 47%. The efficiency at the pump wavelength is approximately 80%, which is the reason why it is necessary to strongly suppress any of the residual pump reflected at the dichroic mirror 1. The efficiency of the camera at wavelengths longer than 1100 nm is negligible, therefore suppression of the idler mode would not be necessary, in principle. As in the case for the standard experiment for induced coherence without induced emission (Chap. 2), the optical path of the signal and idler photons generated in source 1 must be identical within the coherence length of the photons.

3.5.2. Experimental results

Due to the spatial superposition of the idler modes at the crystal and by mixing the signal states by superposing their paths, coherence is induced in the signal photons, and interference is observed at the camera plane. Fig. 3.6(a) shows the interference fringes observed at the camera in the absence of any target, i.e., $\tilde{t}(\boldsymbol{x}_t) = 1$. The presence of fringes, rather than a larger area homogeneously subjected to interference, manifests a phase-difference profile between the pump and the generated photons that is not uniform in the plane transverse to propagation. The interference profile is a hyperbolic pattern, which is the phase profile of astigmatic Gaussian beams [77]. The possible causes of the astigmatism are not addressed in this thesis. Nevertheless, the hyperbolic interference profile does not preclude the capability of conducting imaging. Fig. 3.6(b) shows the interference at the camera when a target is positioned such that only approximately half of the idler profile is transmitted. Where the idler path is interrupted, interference is lost.

To infer the local transmittance of the target, one has to measure the local visibility of the interference at the camera. An experimental result using a target that is a cardboard cut-out placed in the idler photon path is shown in Fig. 3.7(a). A picture of the target is shown in Fig. 3.7(b). To infer the interference visibility, the relative phase between the photons is varied such that each pixel on the camera experiences destructive and constructive interference. Specifically, the relative phase between the pump and the signal is varied by controlling the position of mirror 2 in the setup with the motorized stage. Fig. 3.7(c) shows three examples of acquisitions acquired at different relative-phase conditions. Once a full set of interferograms is acquired, the maximum and the minimum counts are evaluated for each pixel to experimentally

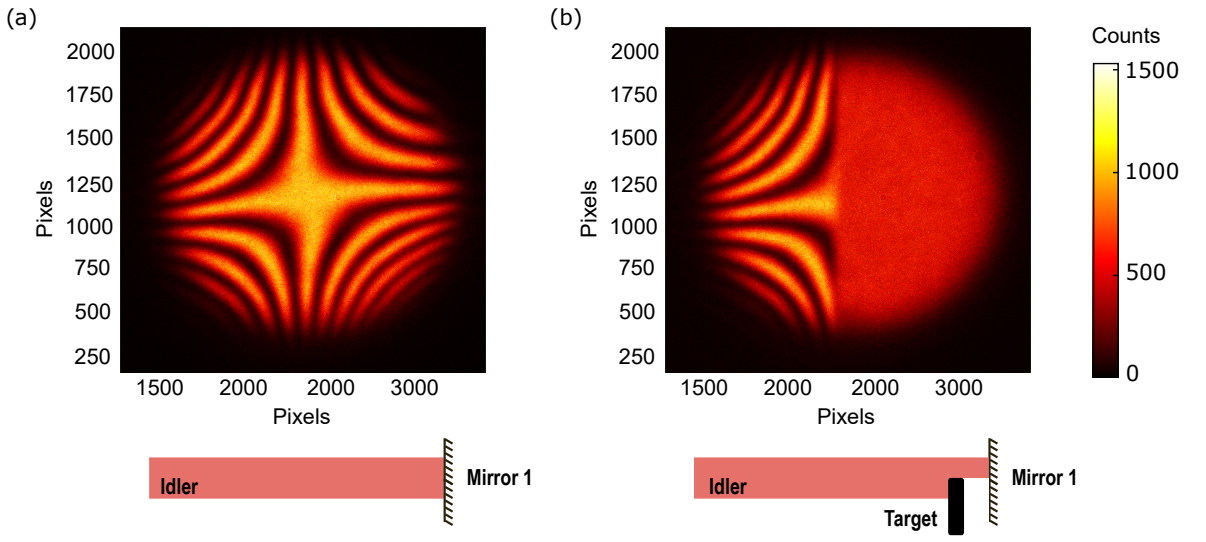

Figure 3.6.: Interference pattern in the signal counts on camera (top), with different conditions for the idler-target interaction (bottom, schematized). (a) The idler interacts with no target. (b) The idler path is locally interrupted by a target of real transmittance $t = 0$.

derive the visibility of the interference. The visibility at position $\boldsymbol{x}_c$ is calculated as

$$v(\boldsymbol{x}_c) = \frac{\max[\text{counts}(\boldsymbol{x}_c)] - \min[\text{counts}(\boldsymbol{x}_c)]}{\max[\text{counts}(\boldsymbol{x}_c)] + \min[\text{counts}(\boldsymbol{x}_c)]}, \tag{3.25}$$

where $\max[\text{counts}(\boldsymbol{x}_c)]$ ($\min[\text{counts}(\boldsymbol{x}_c)]$) selects the maximum (minimum) of the signal counts for the whole set at coordinate $\boldsymbol{x}_c$. Due to the hyperbolic phase profile in the interference pattern, a higher number of acquisitions is required with respect to the case in which the interference profile is uniform in the transverse plane. In that case, image reconstruction would require two acquisitions: uniformly constructive and destructive interference.

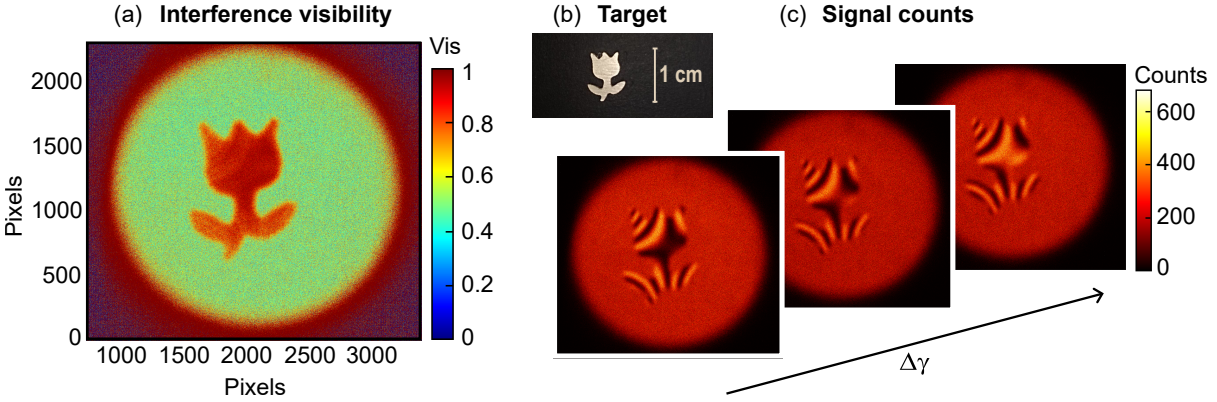

Figure 3.7.: Experimental results for imaging of a cardboard cutout. (a) Interference visibility (vis) per pixel. (b) Picture of the cardboard cutout used as a target, with a reference size indicated on the image. In the experimental setup, the target has been positioned upside down. (c) Signal counts per pixel at three different relative-phase conditions.

To mitigate the error on the visibility, one could think of performing a sinusoidal fit of the fringes and deriving the visibility from the fit results, rather than using Eq. (3.25). However, given the number of pixels of the camera, the computational time with standard computational resources would be impractical. Indeed, in the experiment, I illuminated a region of the camera

that is approximately 2000 × 2000 pixels. I measured the computational time required for a sinusoidal fit in Matlab with the typical number of data points I acquired to derive an image (50 acquisitions) and calculated the total computational time that it would be required to obtain an image by fitting the data. The average computational time per fit is $t_{\text{fit}} = (6.2 \pm 0.7)$ ms. By performing 2000×2000 fit, the total computational time for one image would be $t_{\text{image fit}} = (6.9 \pm 0.8)$ hours. By calculating the visibility as in Eq. (3.25), the computational time for one image is $t_{\text{image w/o fit}} = (12 \pm 1)\ ms$, which is significantly more convenient. Moreover, this faster approach is more suitable for imaging systems characterized by a faster temporal dynamics.

Point spread function, magnification and resolution

Typical experimental setups in a far-field configuration, including the far-field imaging setup described in this chapter, satisfy the condition

$$w_p^2 \ll \frac{\lambda_s L}{4\pi}, \tag{3.26}$$

where λ_s is the shorter wavelength of the generated photons. Under this condition, the term that depends on the crystal length L in the expression for the joint probability density for the transverse momenta in Eq. (3.7) varies slowly enough with respect to the term depending on the pump waist w_p to be considered as a constant. Therefore, the joint probability density for the transverse momenta can be simplified as

$$|C(\boldsymbol{q}_s, \boldsymbol{q}_i)|^2 = A' \exp\left(-\frac{1}{2}|\boldsymbol{q}_s + \boldsymbol{q}_i|^2 w_p^2\right), \tag{3.27}$$

where A' is a normalization constant.

In the paraxial approximation, for the experimental setup schematized in Fig. 3.5, the momenta transverse components $\boldsymbol{q}_s$ and $\boldsymbol{q}_i$ can be associated to a position on the camera $\boldsymbol{x}_c$ and a position on the target $\boldsymbol{x}_t$ respectively as

$$\boldsymbol{x}_c = \boldsymbol{x}_{\boldsymbol{q}_s} = f_c \lambda_s \frac{\boldsymbol{q}_s}{2\pi} \qquad \text{and} \qquad \boldsymbol{x}_t = \boldsymbol{x}_{\boldsymbol{q}_i} = f_t \lambda_i \frac{\boldsymbol{q}_i}{2\pi}. \tag{3.28}$$

When imaging a point-like object, such that $t(\boldsymbol{x}_t) \propto \delta^2(\boldsymbol{x}_t)$, the visibility of the image on the camera at the coordinate $\boldsymbol{x}_c$ is the PSF of the system. Therefore, the normalized PSF for the far-field imaging setup considered in this thesis is

$$PSF(\boldsymbol{x}_c) = \exp\left(-\frac{1}{2} w_p^2 \left| \frac{2\pi}{\lambda_s} \frac{1}{f_c} \boldsymbol{x}_c \right|^2\right) \tag{3.29}$$

Knowing the PSF of the system and the transmittance of the object allows simulating the imaging capabilities of the system. Fig. 3.8 shows experimental imaging data compared with a numerical simulation. The target imaged is the element (-1,4) of a 1951 USAF resolution test target, which is a slab of soda lime glass of thickness 1.5 mm, on which an absorptive and low-reflectance chrome pattern is etched. The pattern consists of equidistant vertical stripes, and the width of a stripe equals the distance between subsequent stripes. The lines density for the target considered, expressed in line-pairs per millimeter, is 0.707 lp/mm. Using this target, measurements and simulations have been compared in Fig. 3.8(right). The original code for the numerical simulation is reported in Appx. B.3. The simulation takes as inputs the setup parameters, such as photons wavelengths, the pump waist and focal length of the

lenses in the setup, and the transmittance of the target as a function of the spatial coordinate $\boldsymbol{x}_t$. Additionally, the simulation takes into account two experimental values, which are the maximum visibility that is possible to infer with the setup, i.e., the visibility in the absence of any target, and the minimum visibility, i.e., the visibility when the target is totally absorptive. The maximum visibility in the absence of a target can be lower than one due to propagation losses of the idler generated in source 1, and unbalanced losses in the pump and the signal (see Sect. 2.7). A non-zero visibility for an absorptive target is due to the statistical fluctuation in the signal counts at the camera, which affects the signal-to-noise ratio of the imaging acquisition. The issue of the signal-to-noise ratio will be further addressed in the following.

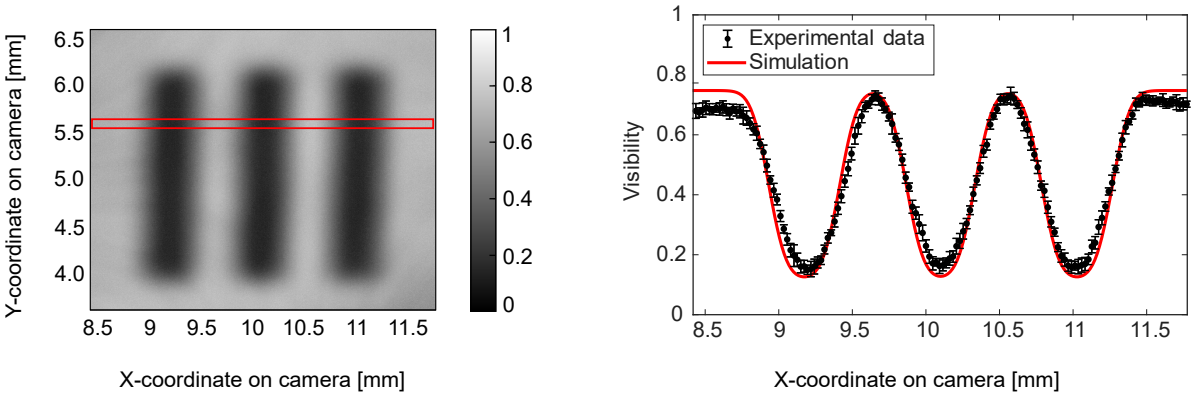

Figure 3.8.: Experimental results and simulation for imaging of a 1951 USAF resolution test target. The separation between the lines on the target is approximately 700 μm (group number -1, element number 4.) (left) Interference visibility as a function of the spatial coordinates on the camera plane. Spatial coordinates on the camera have been obtained by multiplying the pixel number by the pixel size. In red is highlighted a region used to derive the data on the right. (right) Visibility as a function of the x-coordinate on the camera. The experimental data (dots) are derived by averaging on the y-coordinate in a selected region on the image. Error bars are derived as standard deviations. For graphical clarity, only one in every five points is shown. Experimental data are compared with a simulation (line).

From the expression of the PSF in Eq. (3.29), I derive the value for $\boldsymbol{x}_c$ such that the normalized PSF drops to 1/e:

$$\Delta_c = \frac{f_c \lambda_s}{\sqrt{2}\pi w_p}. \tag{3.30}$$

The minimum distance resolved on the camera σ_c is twice Δ_c, since it takes into account that two points are resolved on camera when their PSF cross at 1/e of their maximum value:

$$\sigma_c = 2\Delta_c. \tag{3.31}$$

Experimentally, Δ_c can be derived with a knife-edge resolution test[6], in which the transmittance of the target as a function of the spatial coordinate is a step function:

$$t(x_t, y_t) = \begin{cases} 0 & \text{if} \quad x_t \leq x_0 \\ 1 & \text{if} \quad x_t > x_0 \end{cases} \tag{3.32}$$

The image produced by a knife-edge target is called the edge spread function, and in the case in which the PSF has a Gaussian shape, which is the case of interest, the edge spread function

[6]The experimental implementation of a knife-edge resolution imaging test is more feasible than the imaging of a point-like object.

has the shape of an error-function in the form

$$ESF(x_c, y_c) = v_{\min} + (v_{\max} - v_{\min}) \left[1 + \mathrm{erf}\left(\frac{x_c - x_c^0}{\Delta_c} \right) \right], \tag{3.33}$$

where $v_{\max}$ and $v_{\min}$ are the maximum and minimum visibilities that can be observed with the imaging system, and x_0^c is a coordinate offset along x_c. Approximately, Δ_c is the distance on the image such that the edge-spread function transits from 24% to 76% between its minimum and maximum values, $v_{\min}$ and $v_{\max}$.

Fig. 3.9 shows the experimental results and the results of a numerical simulation for a knife-edge resolution test. In the setup used to obtain the experimental results in Fig. 3.9, $f_c = 300$ mm, $\lambda_s = 810$ nm, and $w_p = 342$ μm. According to Eqs. (3.30), the theoretical result for Δ_c is

$$\Delta_c^{\mathrm{th}} = \frac{f_c \lambda_s}{\sqrt{2}\pi w_p} = 159.9\,\mu\mathrm{m}. \tag{3.34}$$

To derive an experimental value for Δ_c, I considered a thin section of the image (highlighted in the red square box in Fig. 3.9, on the left). I calculated the average and standard deviation along the y-axis to obtain the mean intensity profile along the x-axis, plotted on the right. Data were fitted with the function in Eq. (3.33), with Δ_c and x_0^c parameters of the fit. The resulting experimental value for Δ_c is

$$\Delta_c^{\mathrm{exp}} = 170\,\mu\mathrm{m} \pm 10\,\mu\mathrm{m}, \tag{3.35}$$

which is compatible with the theoretical result.

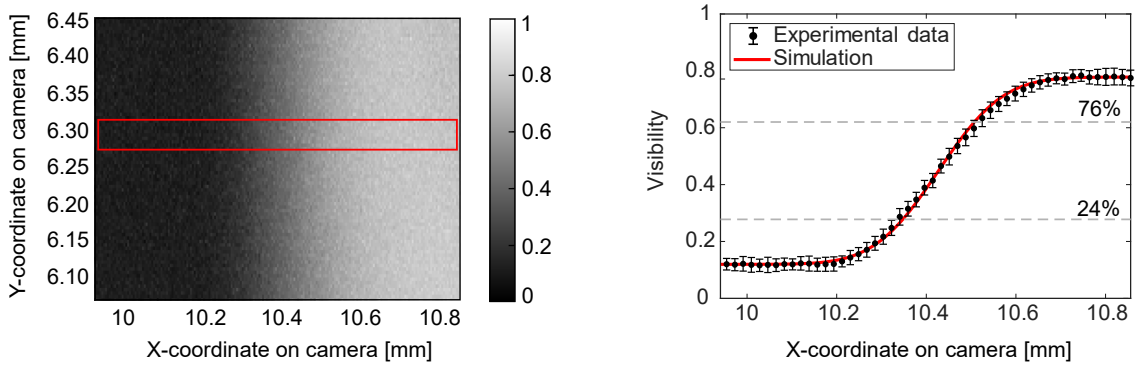

Figure 3.9.: Experimental result and simulation for a knife-edge object. (left) Visibility as a function of the spatial coordinates on the camera plane. In red is highlighted a region used to derive the data on the right. (right) Visibility as a function of the x-coordinate on the camera plane. The experimental data (dots) are derived by averaging on the y-coordinate in a selected region on the image. Error bars are derived as standard deviations. For clarity, only one in every four points is shown. Experimental data are compared with a simulation (line).

To find the resolution of the system, the minimum resolvable distance on the camera σ_c has to be divided by the magnification M of the system, which is the relative magnification between the idler and the signal.

To derive M, one has to take into account the refractive effects at the crystal [78]. The momentum conservation imposes that the condition

$$\boldsymbol{q}_s + \boldsymbol{q}_i = \boldsymbol{q}_p \tag{3.36}$$

is valid in the crystal, where $\boldsymbol{q}_j$ is the transversal component of the momentum for the photon j at the center of the crystal.

Condition (3.36) can be written as

$$\omega_s n(\omega_s)\sin(\theta'_s) = -\omega_i n(\omega_i)\sin(\theta'_i), \tag{3.37}$$

where ω_j is the angular frequency for the photon j, n is the refractive index of the material, and θ'_j is the angle in the crystal between the momentum vector $\boldsymbol{k}_j = (\boldsymbol{q_j}, k_j)$ and the momentum of the pump.

For a collinear process, the magnification M is

$$M = \frac{\boldsymbol{x}_{\boldsymbol{q}_s} - \boldsymbol{x}_{\boldsymbol{q}_s=0}}{\boldsymbol{x}_{\boldsymbol{q}_i} - \boldsymbol{x}_{\boldsymbol{q}_i=0}} = \frac{\boldsymbol{x}_c}{\boldsymbol{x}_t}, \tag{3.38}$$

where I choose the offset on the spatial coordinates such that $\boldsymbol{x}_{\boldsymbol{q}_s=0} = \boldsymbol{0}$ in the camera plane and $\boldsymbol{x}_{\boldsymbol{q}_i=0} = \boldsymbol{0}$ in the target plane.

In the paraxial approximation,

$$\boldsymbol{x}_c = \boldsymbol{x}_{\boldsymbol{q}_s} = f_c \tan(\theta_s) \simeq f_c\theta_s \quad \text{and} \quad \boldsymbol{x}_t = \boldsymbol{x}_{\boldsymbol{q}_i} = f_t \tan(\theta_i) \simeq f_t\theta_i \tag{3.39}$$

where the angle θ_j is the angle between the momentum $\boldsymbol{k}_j$ for the photon j and the optical axis.

At the crystal interface, according to Snell's law of refraction,

$$\sin(\theta_s) = n_s(\omega_s)\sin(\theta'_s) \qquad \text{and} \qquad \sin(\theta_i) = n_i(\omega_i)\sin(\theta'_i). \tag{3.40}$$

By writing Eq. (3.37) as a function of the photon wavelengths rather than as a function of their angular frequencies, and substituting the relations (3.40) in (3.39), the magnification M in Eq. (3.38) of the system results to be

$$M = -\frac{f_c\lambda_s}{f_t\lambda_i}. \tag{3.41}$$

Therefore, the resolution of the imaging system in the far-field configuration is

$$\sigma = \frac{\sigma_c}{|M|} = \frac{2\Delta_c}{|M|} = \frac{\sqrt{2}f_t\lambda_i}{\pi w_p}. \tag{3.42}$$

$$\sigma = \frac{f_t\lambda_i}{\sqrt{2}\pi w_p}. \tag{3.43}$$

Differently than in the near-field case, the magnification in the far-field configuration depends on the signal and idler wavelengths. Consequently, the dependence on the signal wavelength of the magnification M and on the minimum resolving distance σ_c cancel out, and the resolution is limited by the idler wavelength only. Moreover, as expected, a tighter pump waist degrades the transverse momentum anti-correlation between the signal and the idler: the resolution is inversely proportional to the pump waist at the crystal center.

Signal-to-noise ratio

In the imaging results, the visibility for totally absorptive elements is non-zero. As an example, this can be observed in Fig. 3.7(a): even where the cardboard is not cut out, the visibility

at the camera appears to be approximately 0.5. This occurs for short integration times or low signal photon rates, since photon number at the pixel of the camera is affected by super-Poissonian statistics (see Sect. 1.3.2). A pixel may acquire no photon counts in one frame of the interferogram set, which will lead to visibility equal to 1 in that pixel. I calculate the signal-to-noise ratio (SNR) as the ratio between the visibility obtained for a completely transmissive target and the visibility obtained for a completely absorptive target. Practically, SNR measurements are performed with a knife-edge experiment as in Fig. 3.9, and considering the ratio between the visibility on the left side and on the right side.

Fig. 3.10 shows the dependence of the SNR on the integration time at the camera (a) and pump power (b). Together with the pump power, I estimated experimentally the idler power density on the target. Specifically, for low integration time or low pump power, the SNR is affected by the statistical fluctuation in the signal photon counts per pixel at the camera. The optimal integration time and pump power depend on the target to be imaged. Short integration times enable real-time imaging, allowing for the study of the dynamics of the system. However, the SNR cannot always be recovered by increasing the pump power to increase the signal photon number at the camera, since it increases the idler intensity on the sample, which can lead to phototoxicity effects for some targets, e.g., biological samples.

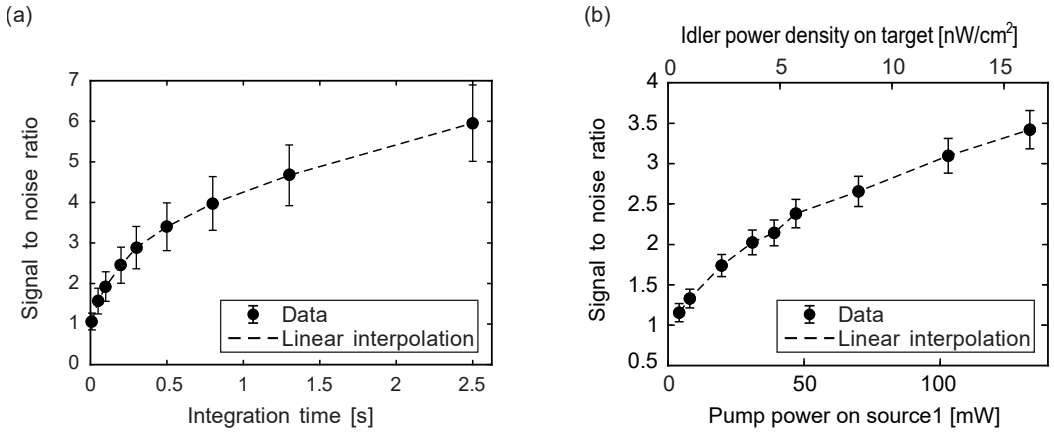

Figure 3.10.: Signal-to-noise ratio (SNR). (a) SNR as a function of the integration time on the camera. The on-crystal pump power is 50 mW. (b) SNR as a function of the on-crystal pump power for the first generation and as a function of the idler power density on the target. Integration time on the camera is 0.3 s.

To address the idler photon density as a function of the pump power, I characterized the setup by measuring at the camera the signal counts that were generated in the first generation process as a function of the pump power. Then, I corrected the measured signal counts, taking into account the propagation losses and the camera efficiency. In this way, I obtained an estimation on the generated signal photons at the crystal. I assume that every signal photon is generated in a pair with an idler photon. Then, I estimated the idler counts at the target plane, taking into account the idler propagation losses from the source to the target. The idler power was estimated as the idler photon rate at the target times the idler energy $\hbar\omega_i$. To estimate the power density, I divided the output power by the idler beam area and multiplied by a factor of two, which accounts for the Gaussian intensity profile. Indeed, the power density at the center of a Gaussian beam is twice the average power density of a top-hat beam with the same total power and area [79]. To lower the idler power density, one can think of increasing the magnification of the idler on the sample. However, this will affect the resolution capabilities of the imaging setup: as it was shown before (Eq. (3.42)), the resolution of the images is obtained by dividing

the minimum resolvable distance at the camera for the relative magnification between the signal and the idler. A larger magnification on the idler will degrade the resolution.

4. Three-dimensional imaging of diffusive targets

In the previous chapter, I discussed the two-dimensional imaging capabilities of a setup for imaging with undetected photons. However, the technique is intrinsically well suited for three-dimensional imaging as well. Indeed, the visibility of the interference pattern in the signal photon counts at the camera plane is controlled by the relative path of the idler and signal generated in the first generation process. Therefore, controlling the path of the signal allows for exploring different object planes in the idler path. If the imaging setup is in a folded configuration, one can use the idler photon as a probe towards a target located at an unknown position and tune the path of the signal photon. If interference is observed in the signal photon counts, the path length of the idler matches the known optical path of the signal, and the position of the target can be retrieved.

The main limitation of this technique is that the interaction of the idler with a realistic target induces distinguishability between the two processes, degrading the resulting interference visibility. Among the causes of this induced indistinguishability, a major role is played by the interaction of the idler with rough surfaces. Overcoming this limitation would allow the applicability of the technique to be extended to imaging diffusive targets in scenarios where aligning a target with a mirror is impractical. These applications include in vivo biological imaging, in which the probe is chosen to penetrate biological tissues, in-depth imaging for cultural heritage, and covert imaging[1]. The latter would benefit from the technological limitations in detecting the probing idler wavelength, while the visible signal is kept private.

In this chapter, I discuss the three-dimensional imaging capabilities of the technique of imaging with undetected photons. First, I show the experimental results for identifying purely reflective targets located at arbitrary positions along the optical axis. Then, I address the issue of imaging rough surfaces. Specifically, I theoretically study the maximum achievable visibility in the interference pattern under different experimental conditions and perform imaging experiments using a textured mirror as a target.

4.1. Optical coherence tomography with undetected photons

In an experiment of induced coherence without induced emission, the visibility of the interference pattern is affected by the path difference between the signal and idler photons generated in the first generation process, as discussed in Sect. 2.4. Specifically, in a folded configuration, the relative path between the signal and the idler must be equal within the coherence length of the photons [14]. Therefore, one can find the longitudinal spatial coordinate of the mirror that reflects the idler by controlling the reference mirror of the signal.

Consider the configuration schematized in Fig. 4.1(a), which represents an experiment for

[1] Covert imaging refers to imaging techniques in which the probing operation is difficult to detect or remains hidden from observation.

imaging with undetected photons in a folded configuration. The residual pump, the signal, and the idler are separated. The idler is reflected by a partially transmitting mirror, and a second mirror is aligned behind it. The distance between the idler mirrors is larger than the coherence length of the photons. The position of the signal mirror along the optical axis is controlled[2]. If one is able to finely move this reference mirror for a travel length that is larger than the coherence length of the photons, it can be observed that the interference pattern is modulated, as it is represented in Fig. 4.1(b). Indeed, a local maxima in the visibility is observed when the optical path of the signal equals the optical path of the idler. Since the configuration includes two idler mirrors at different positions along the optical axis, interference is found at two different locations by moving the reference signal mirror. In this sense, the visibility of the interference pattern observed at the camera as a function of the reference mirror position allows measuring the position of the idler mirrors. This capability enables optical coherence tomography (OCT) with undetected photons, which is also referred to as induced coherence tomography in the literature [25, 26]. In Fig. 4.1(b), the triangular shapes in the envelope functions reproduce the shape of the first-order coherence function for unfiltered photons generated via a nonlinear parametric process, which exhibit the typical sinc-square shaped spectrum[3].

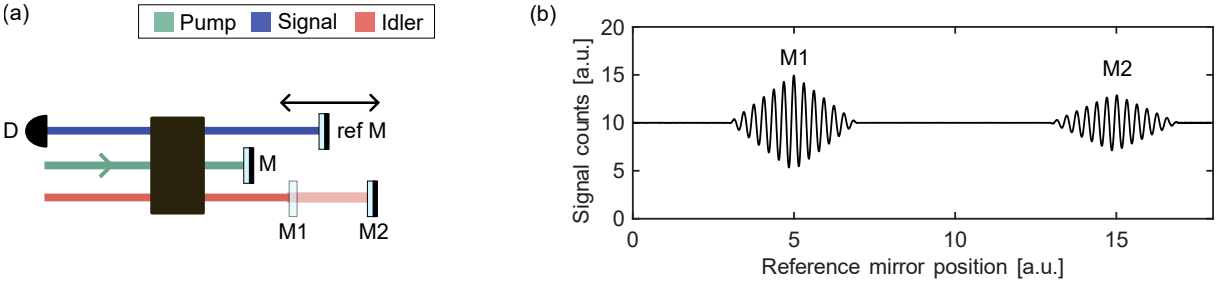

Figure 4.1.: Optical coherence tomography with undetected photons. (a) Schematic of an experimental setup in a folded configuration. First (second) generation process: from left (right) to right (left). The idler interacts with the mirror M1, which is partially transmissive, and with the mirror M2. The signal is reflected by a reference mirror (ref M), the position of which is controlled along the optical axis. The pump is reflected by the mirror M. The signal modes are measured with a single-pixel detector (D). (b) Reproduction of the signal counts at the detector. It is expected to see an interference pattern when the position of the reference mirror matches the position of M1 and M2. The visibility of the interference is maximum when the optical paths of the signal and the idler are identical.

As in standard OCT setups [24], the spatial resolution along the optical axis is increased when the coherence of the signal and idler photons is degraded. Indeed, when the coherence of the photons is low, the envelope functions for the interference patterns in Fig. 4.1(b) are sharper, enabling for more precise measurements. Photons with low coherence length can be obtained by using a short nonlinear crystal as a photon source [10]. Indeed, the length of the crystal affects the joint spectral intensity, as described in Sect. 1.2.1. However, the photon-pair generation rate exhibits a quadratic dependence on the crystal length, therefore, one has to take into account the trade-off between the in-depth resolution capabilities of the setup and the brightness of the source, which affects the integration time required for a measurement with a decent signal-to-noise ratio. In this thesis, I used a 20 mm long crystal. The reason for using such a long crystal,

[2]It is advisable to use the reference mirror to control the path of the signal photon only, without varying the path of the residual pump. Indeed, by varying the path of the pump on the macroscopic scale, the focusing condition in the second generation process varies, affecting the indistinguishability of the processes. This is the reason why the signal is spatially separated from the signal with respect to the configuration presented in Chap. 3.

[3]The first-order coherence function is the Fourier transform of the spectrum, and the Fourier transform of the sinc-square is a triangular function.

at the expense of the longitudinal resolution, is that the experimental setup was implemented with the covert imaging application of the technique in mind. The longitudinal resolution (∼0.75 mm) provided by such a long crystal is more than acceptable for this application, while offering a higher generation rate compared with setups featuring shorter crystals.

I characterized the visibility of the interference pattern as a function of the relative path between the signal and the idler [14]. The experimental setup is schematized in Fig. 4.2. In this experiment, the idler mirror is at a fixed position, and the reference mirror can be moved along the optical axis with a motorized translational stage with a resolution of 50 nm. This stage is positioned on a translational stage with 10 μm displacement resolution and 50 mm travel length. To map the visibility of the interference for different relative paths between the signal and the idler, I moved the position on the coarser translational stage and then acquired an interference pattern by varying the signal phase with the motorized translational stage. In this experiment, the coherence length is long enough such that, among the acquired periods of the interference pattern, the visibility can be considered as a constant. Since this characterization does not require two-dimensional imaging acquisitions, I coupled the signal photons to a single-pixel single photon avalanche diode (SPAD), rather than to the photon-number resolving camera used in Chap. 3. Due to the (hyperbolic) interference pattern in the signal photon counts, it is not possible to observe interference in the signal photon counts by coupling the whole interference pattern into a single pixel, since the global counts of signal photons do not change. Therefore, I coupled only the center of the interference pattern into the SPAD. Specifically, I selected the center of the interference pattern using an iris diaphragm and verified the resulting spot on the camera by using a flip mirror.

Figure 4.2.: Schematic of the experimental setup for measuring the interference visibility as a function of the reference signal mirror longitudinal coordinate. The position of the reference mirror (ref M) for the signal photons is controlled with a manual translational stage. At each position, the interference pattern in the signal modes is acquired with a single-pixel SPAD (D). To measure the interference pattern, the reference mirror is moved with a motorized stage. To access the single-pixel information, only a uniform region of the two-dimensional interference pattern is selected with an iris diaphragm (Iris). To verify that the iris is correctly centered, the signal beam is imaged on a camera (C) with a flip mirror (Flip M). The signal modes are coupled to the detector with an aspheric lens mounted on a micro-block stage (not pictured).

At different positions set with the coarse translational stage, I finely moved the motorized stage to acquire an interference pattern in the signal photon counts. Each interference pattern was fitted with a function of the form

$$\text{Counts} = a_1(1 + b_1 \cos(c_1 z + d_1)), \tag{4.1}$$

where a_1, b_1, c_1, d_1 are parameters of the fit, and z is the position of the motorized stage. From each fit result, I derived the corresponding interference visibility. Fig. 4.3(a) shows the interference visibility as a function of the path difference set with the coarse translational stage. Figs 4.3(b) and (c) show interference patterns at different positions.

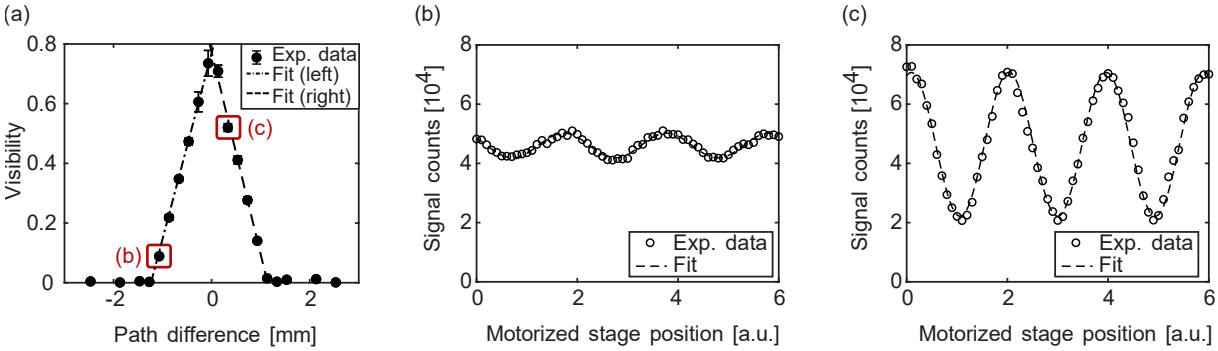

Figure 4.3.: Experimental results on the signal and idler path difference and the corresponding interference visibility. (a) Interference visibility as a function of the path difference. Dots: visibility data derived from the fit of the experimental interference patterns . Dash-dotted (dashed) line: linear fit of the data points on the left (right) side of the peak, excluding the points with visibility approximately equal to zero. The path difference has been obtained as twice the mirror position on the coarse translational stage, with the zero position chosen as the position with maximum visibility, according to ref. [14]. (b) [(c)] Interference pattern with the path difference equal to -1.07 mm [0.33 mm]. Dots: experimental data. Dashed line: result of the fit in Eq. (4.1).

The visibility as a function of the path difference ΔL reproduces the expected triangular shape of the first-order correlation function $g(\tau)$ (see Sect. 1.3), with τ the relative time delay, $\tau = \Delta L/c$. The coherence length is experimentally derived as the value such that the visibility drops from its maximum to 1/e of its maximum. The coherence length is related to the bandwidth $\Delta\nu$ of the photons as [53, 80, 81]

$$\mathcal{L}_{\text{coh}} = \frac{c}{\Delta\nu}. \tag{4.2}$$

From the result in Fig. 4.3, the coherence length for the signal and the idler is 0.75(4) mm, which corresponds to (400 ± 21) GHz bandwidth, i.e., 0.88(4) nm at 810 nm and 3.2(2) nm at 1550 nm. If the target is reflective, it is possible to identify its position by controlling the position of the reference mirror only. Fig. 4.4(a) presents an experimental implementation of imaging of two reflective elements at different positions in the idler photon path. The experimental results are shown in Fig. 4.4(b).

Such an experimental configuration finds its application for imaging reflective targets, which rarely represent the case of a real physical system.

4.2. Rough surface targets

Imaging with undetected photons is quite sensitive to scattering effects, which degrades the indistinguishability between the idler modes and therefore the degree of coherence induced in the signal. Consequently, the interference visibility is affected. Scattering processes affect the spatial superposition between the idlers. Volume scattering effects, such as the Rayleigh scattering, can be suppressed by choosing a long wavelength as a probing wavelength [26]. In fact the cross section for this scattering process strongly depends on the photon wavelength as [82]

$$\sigma_{\text{R}} \propto \frac{1}{\lambda^4}. \tag{4.3}$$

The choice of a long probing wavelength to avoid volume scattering effects fits well with the intrinsic technological advantage of imaging with undetected photons, as the probing is completely decoupled from the detection. As it has already been discussed in Chap. 3, the choice

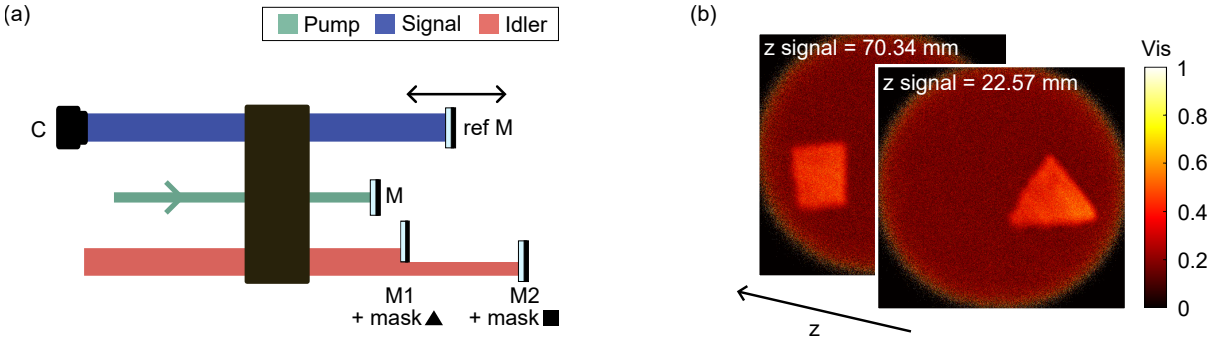

Figure 4.4.: Detection of two reflective targets at different positions along the optical axis. (a) Schematic of the experimental setup in a folded far-field configuration. First (second) generation process: from left (right) to right (left). The idler generated from left to right is partially reflected by the mirror M1, covered with a mask with a cutout triangular shape, and by the mirror M2, covered with a mask with a cutout rectangular shape. The distance between M1 and M2 is larger than the coherence length of the photons. The position of M1 and M2 is fixed. The position of the reference mirror (ref M) that reflects the signal generated in the first generation process is controlled along the optical axis. The signal modes are measured with a camera (C). (b) Experimental results at two different position (z signal) of the reference mirror. The panels show the visibility of the interference (vis) obtained at two different positions of the reference mirror, which correspond to the local maximum visibility.

of long wavelengths makes the imaging technique suitable for non-invasive imaging. Therefore, the choice of using a setup for imaging with undetected photons to perform tomography seems advantageous, as the tomographic capabilities are inherently enabled by the interferometric configuration itself.

However, surface scattering effects still represent a limitation of imaging real non-transmissive objects. As it was already mentioned, an experimental setup for imaging with undetected photons in which the idler mirror is substituted by a real object would allow for the extension of the technique to a wide range of applications. In the biological sector, the technique would allow choosing an idler wavelength to selectively penetrate biological tissues. The limited coherence of the photons allows obtaining interference at selected depths in the material, enabling three-dimensional imaging.

In the following, I will address the issue of using a rough surface as a target and how it affects the indistinguishability between the generation processes and therefore the degree of induced coherence.

4.2.1. Indistinguishability

To achieve indistinguishability between the first and the second generation processes in an imaging experiment with undetected photons, it is necessary that the idler follows the same path from the first nonlinear crystal to the target and from the target to the second nonlinear crystal. In the interaction with a diffusive target, the idler is scattered, meaning that it carries an angle that it did not carry from the crystal to the target, as it is represented in Fig. 4.5(a). This affects indistinguishability. Only the back-reflected photons induce coherence in the signal. Therefore the visibility of the interference pattern is heavily affected by the loss of indistinguishability due to the interaction with a diffusive target. To admit an angular distribution in the idler photons without losing indistinguishability, it is necessary to provide the idler photons with such distribution *before* their interaction with the target.

Consider the implementation schematized in Fig. 4.5(b). The idler photons are focused on the target such that their position at the source plane is imaged on the target with magnification M_i. In this case, $|M_i| \ll 1$ such that the field of view can be considered as a single point on the target. If the focusing lens subtends an angle α on the target, a photon generated at the source has a certain probability to impact on the target with an angle $\gamma \in [-\frac{\alpha}{2}, \frac{\alpha}{2}]$ with respect to the optical axis. Practically, the idler photons are given an angular probability distribution by using a focusing optical element. Assume the target to be partially diffusive, such that the incident photon is diffused within a cone with axis along $-\gamma$, and with a vertex angle θ, as schematized in Fig. 4.5(c). The angle θ quantifies how diffusive the target is. When $\theta = 0$, the target is purely reflective.

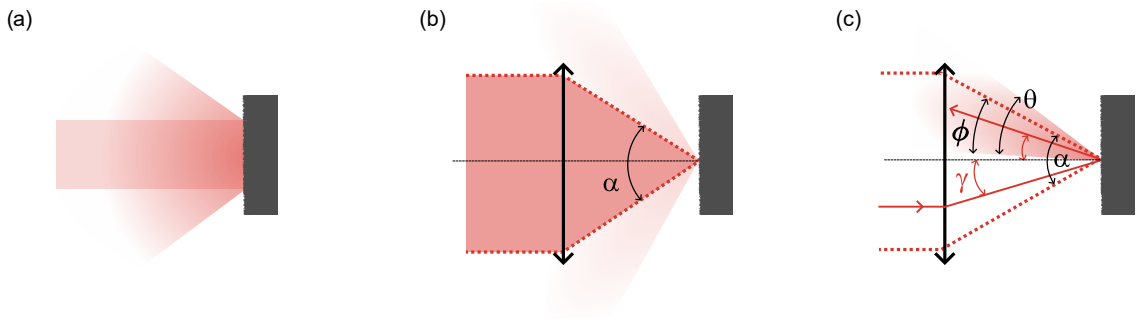

Figure 4.5.: Interaction of the idler with a rough surface. (a) Collimated beam on a diffusive target. (b) Focused beam on a diffusive target. The angle α is the angle subtended by the lens (double-sided arrow). (c) The photon is incident on the target with angle γ, and it can be diffused within the cone with vertex angle θ, centered on the reflection line at angle $-\gamma$. ϕ is the angle of the cone within the intersection between the cone with vertex angle θ and the cone with angle α (red dashed).

The photon that interacted with the target is diffused with an angle $\gamma + \theta'$, with $\theta' \in \left[-\frac{\theta}{2}, \frac{\theta}{2}\right]$. If $\gamma + \theta' \in [-\frac{\alpha}{2}, \frac{\alpha}{2}]$, the diffused photon is imaged on the crystal plane by the lens, and it is indistinguishable from the photons that could be generated in the second generation process, in the specific case of a generation process in which the spectral dependence on the transverse momentum component is not strong. Indeed, if the photons are generated with transverse momentum components that depend strongly on the frequency (as an example, see Fig. 1.11 in chapter 1), different momentum components are effectively labeled by the photon frequency. Therefore, the interaction with the target is in principle accessible, and introducing an angular distribution does not allow recovering indistinguishability.

The probability for a photon that it is incident on the target with an angle γ to be diffused within the cone with vertex angle α is

$$P(\alpha, \gamma, \theta) = \frac{2\pi\left[1 - \cos(\phi(\alpha, \gamma, \theta)/2)\right]}{2\pi\left[1 - \cos(\theta/2)\right]} \tag{4.4}$$

where ϕ is the angle of the cone formed by the intersection between the emission cone and the cone with angle α. Indeed, $2\pi(1 - \cos(x))$ is the solid angle subtended by the cone with vertex angle x. The angle ϕ varies according to the following cases:

a. $\phi = \theta$, if the emission cone is included in the α-cone, i.e.,

$$|\gamma| + \frac{\theta}{2} \leq \frac{\alpha}{2} \quad \text{and} \quad |\gamma| - \frac{\theta}{2} \geq -\frac{\alpha}{2} \tag{4.5}$$

b. $\phi = \frac{\alpha}{2} + \frac{\theta}{2} - |\gamma|$, if the emission cone is partially included in the α-cone, i.e., when

$$\begin{aligned} |\gamma| + \frac{\theta}{2} > \frac{\alpha}{2} \quad &\text{and} \quad |\gamma| - \frac{\theta}{2} > -\frac{\alpha}{2} \\ &\text{or} \\ |\gamma| + \frac{\theta}{2} < \frac{\alpha}{2} \quad &\text{and} \quad |\gamma| - \frac{\theta}{2} < -\frac{\alpha}{2} \end{aligned} \tag{4.6}$$

c. $\phi = \alpha$, if the emission cone includes completely the α-cone, i.e.,

$$|\gamma| + \frac{\theta}{2} > \frac{\alpha}{2} \quad \text{and} \quad |\gamma| - \frac{\theta}{2} < -\frac{\alpha}{2} \tag{4.7}$$

In a more compact notation,

$$\phi = \begin{cases} \theta, & \frac{\theta-\alpha}{2} \leq |\gamma| \leq \frac{\alpha-\theta}{2}, \\ \frac{\alpha}{2} + \frac{\theta}{2} - |\gamma|, & |\gamma| > \frac{\alpha-\theta}{2} \text{ or } |\gamma| < \frac{\theta-\alpha}{2}, \\ \alpha, & \frac{\alpha-\theta}{2} < |\gamma| < \frac{\theta-\alpha}{2} \end{cases} \tag{4.8}$$

Integrating on γ, I obtain the probability for a photon with the angular distribution α and interacting with a target characterized by a diffusing angle θ to be collected within α:

$$\mathcal{P}(\alpha, \theta) = \frac{\int_{-\alpha/2}^{\alpha/2} d\gamma \; |f(\gamma)|^2 P(\alpha, \gamma, \theta)}{\int_{-\alpha/2}^{\alpha/2} d\gamma \; |f(\gamma)|^2} \tag{4.9}$$

where $f(\gamma)$ is a probability amplitude that weights the distribution of the angles γ.

The collection probability is intimately connected with the visibility of the interference pattern that it will be obtained. Assuming that the losses in the signal and the pump are compensated [66] and that the coherence length of the pump is much larger than twice the optical path between the source and the target (see Sect. 2.3), the visibility is affected by the losses on the idler mode only. The visibility of the interference will be

$$v = \mathrm{e}^{-2\eta R} \rho \, \xi \, \mathcal{P}(\alpha, \theta) \, T_{sy}^2 \tag{4.10}$$

where R is the distance between the target and the source, and η represents the propagation losses per unit length. Therefore, the term $\mathrm{e}^{-2\eta R}$ takes into account the propagation losses of the idler in the roundtrip. ρ is the albedo coefficient of the target[4], and ξ is a coefficient that takes into account the probability for a diffused photon to keep its polarization. Indeed, the scrambling of the polarization in the interaction with the target can induce distinguishability between the generation processes. T_{sy} is the transmission coefficient for the idler from the source to the target, which takes into account the probability of not losing an idler photon due to intrinsic losses of the system, e.g., losses at the interface with the optical elements of the setup. It is squared to take into account the losses in a roundtrip. $\mathcal{P}(\alpha, \theta)$ is the collection probability, which is the focus of this section.

Fig. 4.6 shows $\mathcal{P}(\alpha, \theta)$ as a function of θ, for different values of α. If the target exhibits a larger diffusing angle θ, the collection probability for the idler is affected. When the target is fixed, the collection probability can be maximized by increasing the range α of the incident angular probability distribution. In this simulation, I considered the amplitude function $f(\gamma)$ to be a Gaussian, since it reproduces the spatial Gaussian amplitude function for the generation of the idler modes.

[4]The albedo quantifies the fraction of incident light that is returned by the target.

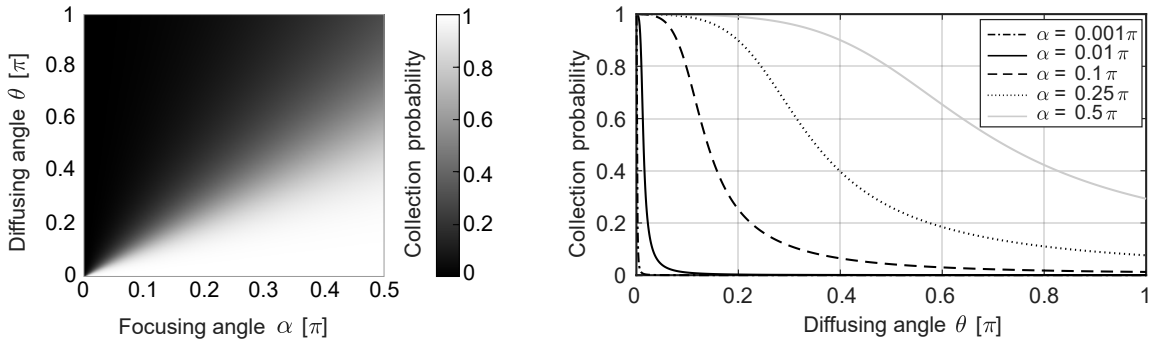

Figure 4.6.: Collection probability for the idler diffused by different rough surfaces. Simulated probability for a photon to be diffused within the cone subtended by the focusing angle α when it interacts with a target characterized by a diffusing angle θ, calculated as in Eq. (4.9). (left) Surface plot. (right) Cut lines in the surface plot at fixed values of α.

4.2.2. Practical applications

The need for large apertures α to compensate for the diffusive effects of a real target limits the practical application of such a configuration in the long-distance range. Fig. 4.7 shows the collection probability $\mathcal{P}$ as a function of the distance of the target R normalized to the diameter d of the optical element used to focus the idler on the target, in a simplified model in which

$$\alpha = \mathrm{atan}\left(\frac{d}{2R}\right). \tag{4.11}$$

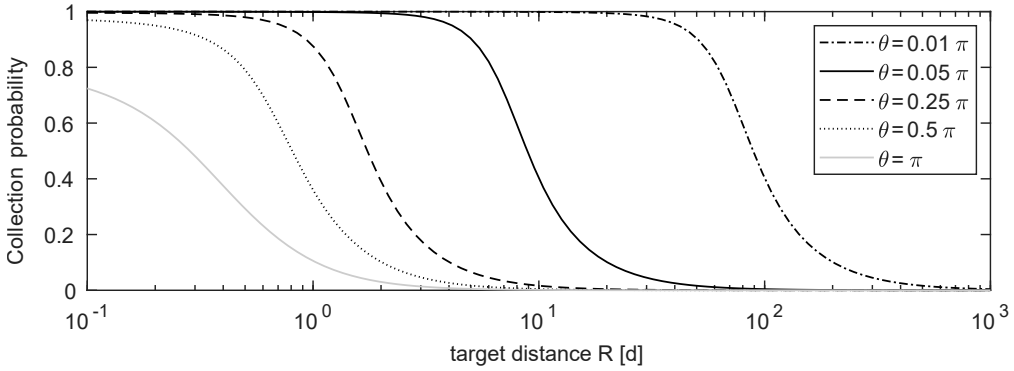

Figure 4.7.: Collection probability for the idler diffused by a target with diffusing angle θ located at a distance R, expressed in units of the dimension d, which is the diameter of the optical element used to focus the idler on the target.

In the short-range regime ($R \ll d$), α is large enough such that the collection probability is consistent even for a Lambertian surface, i.e., a surface characterized by a diffusive angle of $\theta = \pi$. This enables the technique to short-range imaging applications in which the longer wavelength of the idler photons is convenient for imaging trough opaque objects, such as in non-invasive biological imaging applications or imaging for cultural heritage diagnostics.

In the medium-rage ($R \simeq d$), the collection probability strongly depends on the nature of the target. Therefore, the technique can be applied in real-case scenarios in a controlled environment, in which the diffusivity of the target is limited and the target is aligned with the imaging setup.

In the long-range distance, R is large enough to assume $\alpha = \frac{d}{2R}$. At such a distance α is small enough to safely assume that the collection probability goes with $\phi = \alpha$ as described by Eq. (4.7) (case **c.**). In this case, the collection probability asymptotically approaches zero as

$$\mathcal{P}(\alpha,\theta) \xrightarrow{R\gg d} P(\alpha,\theta,\gamma\to 0) = \frac{1-\cos(\alpha/2)}{1-\cos(\theta/2)} = \frac{1-\cos(d/4R)}{1-\cos(\theta/2)} \propto \frac{1}{R^2}. \tag{4.12}$$

Therefore, imaging of a diffusive target at long distances may be challenging due to the reduced visibility of the resulting interference pattern.

4.3. Experimental implementation

I adapted the configuration for imaging with undetected photons to probe diffusive targets and realized the experimental setup schematized in Fig. 4.8. The idler is focused on a textured mirror. This configuration provides single-pixel information, and to reconstruct a three-dimensional image of the target, the target should be scanned in the xyz three-dimensional space. In the results presented in this thesis, I scan along the optical axis z with the reference signal mirror. The scan on the target in the xy plane is done by moving the target, rather than the idler beam. For this reason, the target is positioned on a system of translational stages on the x and y axis. The signal modes are measured with a photon-number resolving camera.

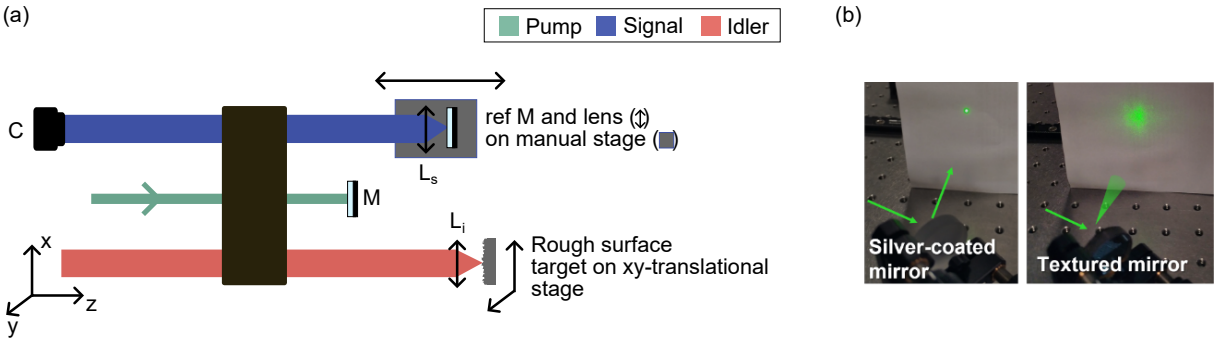

Figure 4.8.: Experimental setup for detecting diffusive targets. (a) Schematic of the experimental setup. The idler generated from left to right is focused with the lens L_i of focal length 5 mm. To compensate for the spatial-dependent path difference of the idler, the signal is focused on the reference mirror (ref M) with a lens L_s of focal length 5 mm. The signal lens and the reference mirror are positioned on a translational manual stage that allows controlling the z-coordinate of the reference mirror. The z-coordinate of the diffusive target is fixed. The target can be moved in the xy-plane. (b) Comparison between the reflection of a visible laser from a silver-coated mirror (left) and from the textured mirror used as a target (right).

4.3.1. Statistics-based visibility analysis

When an interference pattern is obtained on the camera, the visibility associated with the point probed on the target cannot be evaluated by the contrast between the constructive and destructive bands at the camera. Indeed, the interference pattern observed at the camera is not trivial for diffusive targets, since it is not uniformly distributed. Fig. 4.9 shows signal counts at the camera, minus a reference[5], in three different scenarios. In Fig. 4.9(a), no target is

[5]To remove the effect of a spurious reflection at the signal focusing lens, I acquired a reference measurement of the signal photons with the idler path heavily misaligned, i.e., without any interference pattern at the camera plane.

interacting with the idler, and no interference is observed in the signal counts at the camera. Fig. 4.9(b) shows the interference pattern obtained when illuminating an "unfortunate" point of the target: a few photons are collected, and the interference pattern is observed in a limited region of the camera. In Fig. 4.9(c), I report the interference pattern obtained when probing a highly reflective point of the target.

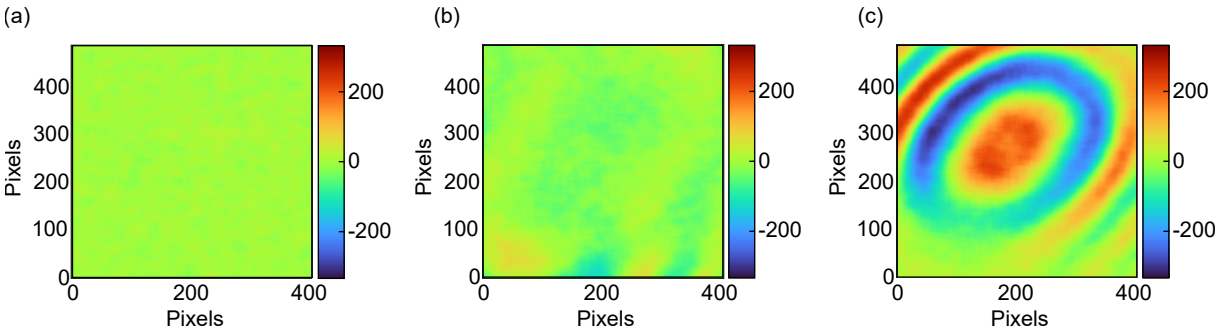

Figure 4.9.: Examples of interference patterns obtained when probing a diffusive target. The images show the signal count per pixel, minus a reference. (a) No target. (b) Low collection probability from the diffusive target. (c) High collection probability from the diffusive target. The concentric rings are due to the optical path difference between the signal and the idler that is introduced by positioning two different lenses on their path.

The acquisitions in Fig. 4.9 show that it is not feasible to derive a single value for the interference visibility at the camera by just looking at the interference pattern. One could choose to attribute to a point probed on the target the mean value for the visibility at each pixel on the camera. However, this would require performing many acquisitions to explore constructive and destructive interference in each pixel.

To automatize the visibility analysis by using a single acquisition at the camera, I experimentally derived the visibility of the interference by an analysis of the signal photon statistics on the camera plane. Although statistics-based methods for contrast estimation have already been developed in optical interferometry [83, 84], they rely on the intensity histogram of a structured interference pattern. Here, the visibility is inferred from the broadening of the statistical distribution of the camera counts, with no assumption on the structure of the fringes.

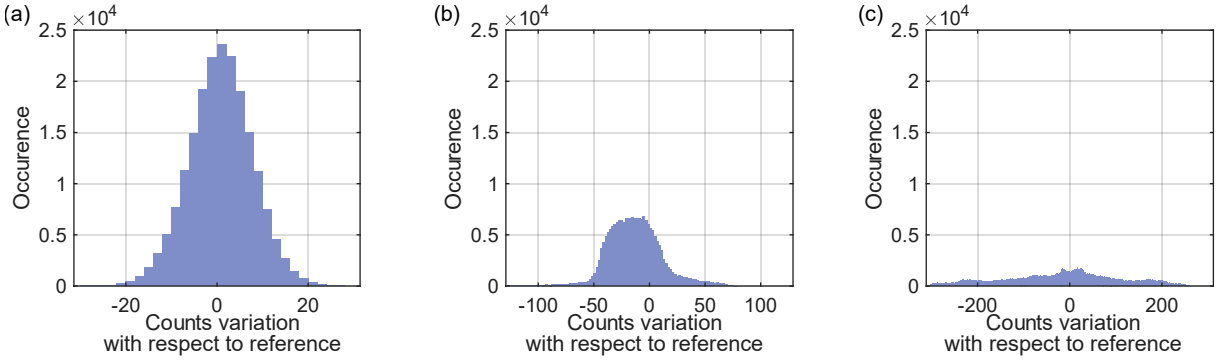

Figure 4.10.: Histograms of the occurrence of the signal counts with respect to a reference acquisition under the different interference conditions reported in Fig. 4.9. Note that the figures exhibit different scales on the x-axis, while they share the same histogram bin width.

The histograms in Fig. 4.10 report the occurrence of the counts shown in Fig. 4.9. When the idler does not interact with any target, the counts occurring at the camera reproduce a Gaussian-shaped distribution, which corresponds to the characteristic distribution of the source.

The distribution broadens when interference is observed at the camera, and the more the camera exhibits constructive and destructive interference fringes, the more the histogram will be populated with counts farther from the center at zero, since the interference pattern will differ more from the reference acquisition. Therefore, relating the visibility to the width of such a distribution seems a natural choice.

It is necessary to connect the distribution width to the visibility. A necessary condition for the validity of this map is its agreement with the experimental data in the limit of an ideal reflective target. Fig. 4.11 shows the statistical distribution in the signal counts under different visibility conditions with respect to a reference measurement. In this case, the idler is made interact with a reflective mirror. A drift of the distribution with respect to the vertical line "Counts variation" = 0 is attributed to the pump power fluctuation of the measurement with respect to the reference. Each histogram has been obtained with a single acquisition on the camera. The corresponding values for the visibility have been obtained by scanning the pump phase. In the figure, one can distinguish the peaks associated with the constructive (C) and destructive (D) bands, which are increasingly separated for stronger visibilities.

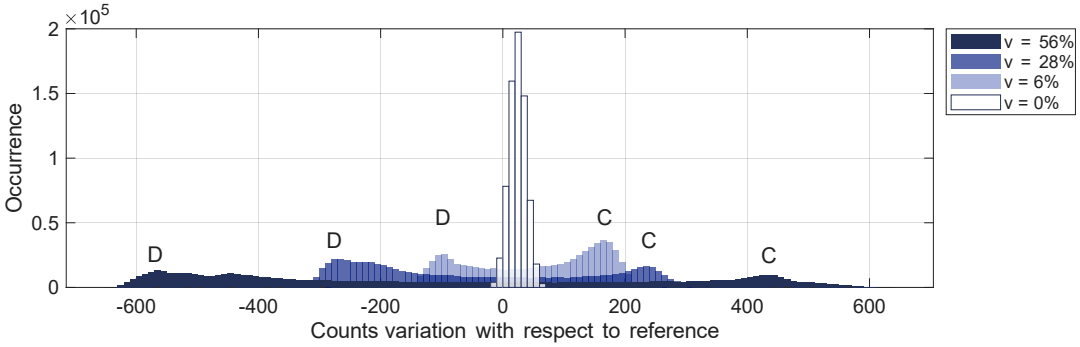

Figure 4.11.: Experimental results for the statistical distribution of the signal counts under different visibility (v) interference conditions. The target was a reflective silver-coated mirror. Different visibility conditions were achieved by positioning absorptive filters in the idler photon path. The peaks associated to the constructive (destructive) interference bands are labeled with the letter C (D).

The width of the distribution obtained in the absence of any target is characteristic of the source and depends on the statistical fluctuations of the detected photon counts. Therefore, by comparing the width of a distribution to this characteristic value, one could quantify the broadening of the distribution due to the presence of the target. I define the quantity

$$p(\sigma_{exp}) = 1 - \frac{\sigma_s}{\sigma}, \tag{4.13}$$

where σ_s is the width of the distribution characteristic of the source that must be experimentally derived under the same experimental condition of the imaging experiment. σ is the width of the distribution to which the visibility is intended to be associated. In this way, p is zero when the distribution to be analyzed coincides with the distribution characteristic of the source and approaches 1 for very large broadenings.

To map the parameter p to the visibility, I numerically simulated the width of the distribution, and therefore the parameter p, under different visibility conditions. The code for the simulation is detailed in Appx. B.4. The simulation takes as input parameters the mean photon number at the camera, σ_s, and the visibility of the interference pattern. The width σ was defined in a way such that, for a Gaussian distribution, it coincides with the standard deviation. For both the simulated and experimental distributions, I evaluated the cumulative distribution function, and defined σ as half the distance between the percentiles 15.87 and 84.13. Once I simulated p for

finely discretized values of the visibility $v \in [0, 1]$, any experimental value for p can be associated with the corresponding simulation by fitting the simulated data. The simulation was compared with experimental data acquired by using a mirror as a target. The experimental results are in good agreement with the simulation, as shown in Fig. 4.12. The evaluation of the parameter p is observed to be sensitive to small variations in the visibility for small visibility values, which makes it a good tool under low visibility conditions, as when probing diffusive targets.

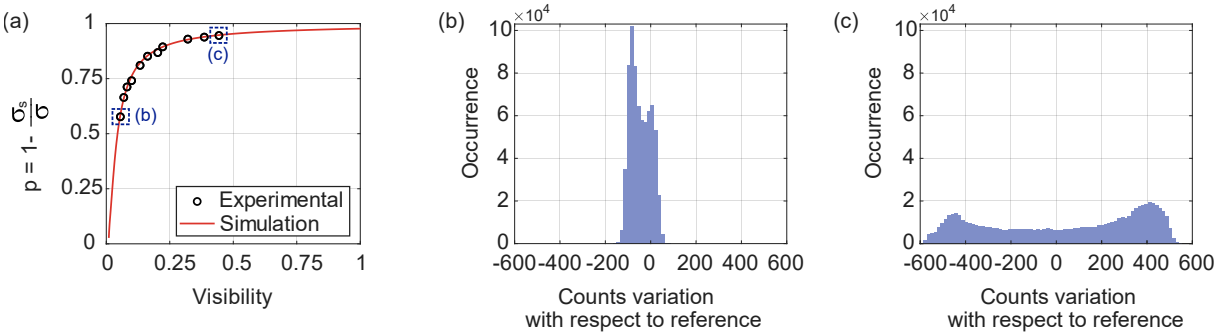

Figure 4.12.: Interference visibility and relative width of the corresponding statistical distribution. (a) p parameter as a function of the visibility. Dots: experimental data. Line: simulation. (b) [(c)] Distribution of the signal counts at visibility 5.5% [44.4%].

In the case of a diffusive target, the statistical distribution does not exhibit the almost-symmetrical shape that it has in the case of reflective targets. However, the underlying idea is to infer the distribution width and then map it to the equivalent visibility that would be obtained for an ideal, fully reflective target.

4.3.2. Experimental results

I reconstructed the image of a two-dimensional textured mirror, partially covered with a mask. The mask shape is shown in Fig. 4.13(a). To acquire each data point, I moved the target in the xy plane, acquired the corresponding interference pattern, and experimentally derived the visibility through the evaluation of the distribution width. To correctly associate the p parameter to its corresponding visibility value through the visibility simulation discussed above, I acquired two[6] reference measurements without any target in the idler photon path to derive the characteristic statistical fluctuation σ_s of the source and the average number of signal photons at the camera. The experimental result for the image reconstruction is shown in Fig. 4.13(b). For comparison, a similar measurement has been done by using the same mask, with a reflective mirror replacing the diffusive target. The results are shown in Fig. 4.13(c).

Then, I reconstructed the yz profile of a three-dimensional object. A schematic of the object is shown in Fig. 4.14(a). Its surface is made of the same textured mirror used for the imaging experiment in Fig. 4.13. Before imaging the diffusive object, the experimental configuration has been calibrated using a mirror as a target to set a reference point for the relative optical path between the signal and the idler. In this stage, the calibration is performed by aligning the focusing lenses, the signal mirror, and the idler mirror such that the maximum of the visibility is observed at the camera plane. With the calibrated setup, when moving the reference mirror, the idler lens is moved accordingly in order to maintain the focusing condition on the target. It is important to emphasize that the position of the target is initially unknown. The reference mirror is moved to investigate whether a target is located at a distance such that the relative

[6]Two measurements are required to experimentally derive the statistical fluctuation characteristic of the source.

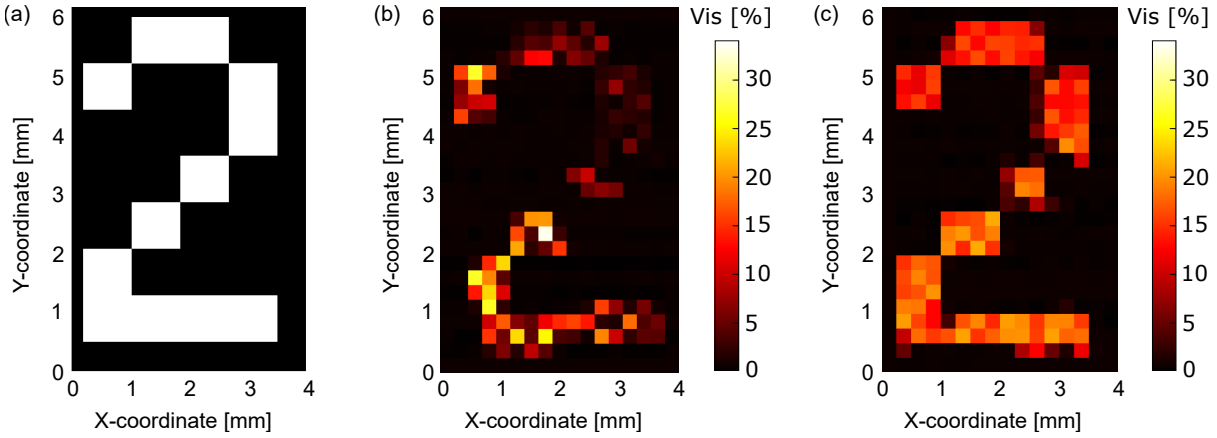

Figure 4.13.: Imaging of a two-dimensional diffusive target. (a) Mask shape. Black: absorptive region. White: Cutout. (b) Experimental results obtained with the mask positioned in front of a textured mirror. (c) Experimental results obtained with the mask positioned in front of a mirror. Vis is the visibility of the interference.

path of the signal and the idler is zero. To maximize the idler collection probability when the target is present, the focusing lens must be moved consistently with the reference mirror. Once interference is observed at the camera, only the optical path of the signal is adjusted, to find the point of maximum visibility. It is assumed that the target is located at a distance from the crystal that matches the optical distance between the crystal and the reference mirror when the visibility is maximum. The location of the maximum is found by fitting the visibility as a function of the signal reference mirror position. The experimental result obtained by following this measurement procedure is shown in Fig. 4.14(b).

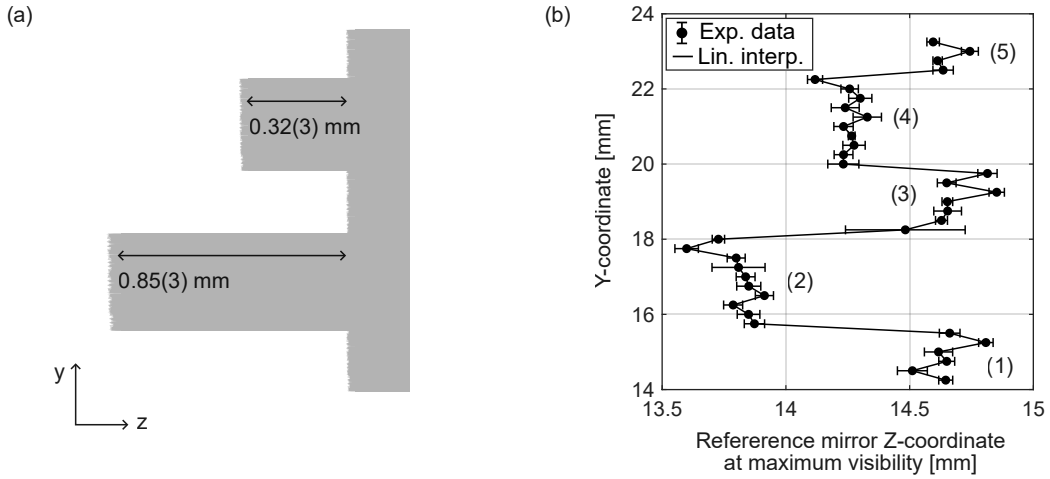

Figure 4.14.: Imaging a three-dimensional diffusive target. (a) Schematic of the target profile in the yz plane. The measurements of the depth of the target have been measured with a caliper. (b) Profile reconstruction. Dots: experimental data with corresponding error bars. Line: linear interpolation. The numbers in brackets indicate the group of data used to evaluate the average z-coordinate and standard deviation corresponding to that region.

I calculated the average and standard deviation of the group of data indicated with the number in brackets in Fig. 4.14(b). The results are summarized in Tab. 4.1.

The resulting step sizes are listed in Tab. 4.2

Dataset number	1	2	3	4	5
Average z-coordinate [mm]	14.6(1)	13.80(9)	14.7(1)	14.24(6)	14.65(7)

Table 4.1.: Average z-coordinates for the datasets indicated in Fig. 4.14(b). The number between brackets is the uncertainty on the last digit.

Compared datasets	1 and 2	2 and 3	3 and 4	4 and 5
Step size [mm]	0.8(1)	0.9(1)	0.5(1)	0.4(9)

Table 4.2.: Difference in the average z-coordinates for adjacent datasets.

All the experimental results but the step size derived by comparing datasets 3 and 4 are compatible with the measured values within their uncertainty.

I reconstructed the image of a three-dimensional target with a rough surface using undetected photons. The prospects of this work lie in the development of imaging systems for realistic targets. In a scenario where scanning is automated and densely sampled, it becomes possible to recover the three-dimensional image of a rough target without the need to align any optical element behind it.

5. On-chip undetected photon phase measurement

Up to now, in this thesis, I presented experimental setups for undetected photon measurements in free-space optical configurations. Nevertheless, free-space implementations face limitations in portability, alignment tolerance, and scalability. The ideal platform to overcome these limitations would be an integrated platform, which offers compact, scalable, and robust architectures. Additionally, integrated photonics naturally guarantees the optical superposition of the propagating modes, which is fundamental to keep a good degree of indistinguishability between the generation processes in an experiment based on undetected photons.

In this chapter, I present an implementation of undetected photon measurements using an integrated design based on silicon photonics. Silicon photonics offers the additional advantage of being compatible with the mass-manufacturable consumer electronics, making it a promising platform for commercial devices based on undetected photons. To the best of my knowledge, these results represent the first demonstration for an experiment with undetected photons in an integrated configuration.

5.1. Induced coherence without induced emission with spontaneous four-wave mixing

The results of this chapter feature a configuration for induced coherence without induced emission based on intermodal spontaneous four-wave mixing (SFWM). The general schematic for the experiment is outlined in Fig. 5.1. Two pump beams, labeled as p_0 and p_1, pump two cascaded nonlinear optical sources, generating correlated idler and signal photons (i and s) via SFWM. Between the sources, a phase γ_k ($k = p_0,\ p_1,\ i,\ s$) can be selectively applied to the pumps, the signal, and the idler. The sources are identical, and the paths of the identical modes are superposed. By varying the phase of any mode between the source, interference is observed at the signal photon counts after the second source. In particular, the interference pattern in the signal carries the information of the phase or absorption experienced by the idler. In the experiment discussed in this chapter, I retrieved the known phase applied to the idler by measuring the signal. Therefore, in the following calculations, I will neglect the discussion concerning any propagation loss in the modes, and I will only consider the phase experienced by the modes. Indeed, it is easy to demonstrate that the losses in the modes do not alter the dependence on the phase of the interference pattern.

To model the experiment schematized in Fig. 5.1, I adapt the notation that I used in Chap. 2 to the case of SFWM. The j-th generation process ($j = 1, 2$) is described by the unitary transformation

$$\hat{\mathcal{U}}_j = \hat{\mathbb{1}} + \hat{\mathcal{H}}_{eff\,j}, \tag{5.1}$$

where $\hat{\mathcal{H}}_{eff\,j}$ is the effective Hamiltonian for the SFWM generation process. In the following, I

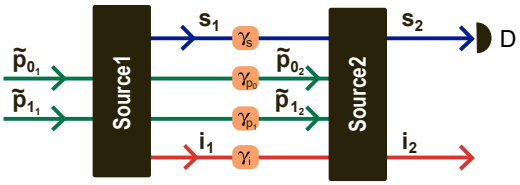

Figure 5.1.: Schematic of an experiment of induced coherence without induced emission based on intermodal spontaneous four-wave mixing. Two classical beams with amplitudes $\tilde{p}_{0_1}$ and $\tilde{p}_{1_1}$ pump a nonlinear optical source, and signal and idler are generated in the modes s_1 and i_1. Photons in the mode s_1 and i_1 acquire a phase γ_s and γ_i, respectively. Phases γ_{p_0} and γ_{p_1} are applied to the residual pumps, which are used to pump a second nonlinear source. In the second source are generated the signal and idler modes s_2 and i_2. The modes s_1 (i_1) and s_2 (i_2) are spatially superposed. Photons in mode s_2 are measured with a photodetector (D).

will consider the simple case of generation of a single pair of signal and idler modes, i.e.,

$$\hat{\mathcal{H}}_{eff\,j} = \tilde{p}_{0_j}\tilde{p}_{1_j}\hat{a}^{\dagger}_{s_j}\hat{a}^{\dagger}_{i_j} + h.c., \tag{5.2}$$

where $\tilde{p}_{0_j}$ ($\tilde{p}_{0_j}$) represents the complex pump amplitude for the mode pump mode p_0 (p_1) for the j-th source, and $\hat{a}^{\dagger}_{k_j}$ is the creation operator for the mode k_j. The whole system is described by

$$\hat{\mathcal{U}} = \hat{\mathcal{U}}_1 \otimes \hat{\mathcal{U}}_1 \simeq \hat{\mathbb{1}} + \hat{\mathcal{H}}_{eff\,1} + \hat{\mathcal{H}}_{eff\,1}, \tag{5.3}$$

where I assumed the probability for SFWM to occur to be low enough to neglect simultaneous generation processes in the sources. Without loss of generality, I assume the pump amplitudes feeding source 1 to be real quantities, then I impose the superposition of the modes generated in the first and in the second source, consider the phase manipulation stage between the sources, and neglect the propagation losses. Therefore, I write the relations

$$\tilde{p}_{0_1} = p_0, \qquad \tilde{p}_{1_1} = p_1, \qquad \tilde{p}_{0_2} = p_0 e^{i\gamma_{p_0}}, \qquad \tilde{p}_{1_2} = p_1 e^{i\gamma_{p_1}}, \tag{5.4}$$

and

$$\hat{a}^{\dagger}_{s1} = \hat{a}^{\dagger}_{s2} e^{i\gamma_s}, \qquad \hat{a}^{\dagger}_{i1} = \hat{a}^{\dagger}_{i2} e^{i\gamma_i}. \tag{5.5}$$

By substituting these in Eq. (5.3), one finds

$$\hat{\mathcal{U}} = \hat{\mathbb{1}} + p_0 p_1 e^{i(\gamma_s+\gamma_i)} \left(1 + e^{i\Delta\gamma}\right) \hat{a}^{\dagger}_{s_2}\hat{a}^{\dagger}_{i_2} + h.c., \tag{5.6}$$

where $\Delta\gamma$ is the phase difference

$$\Delta\gamma = \gamma_{p_0} + \gamma_{p_1} - \gamma_s - \gamma_i. \tag{5.7}$$

By following the same steps as for the SPDC experiment in the same configuration (see Appx. A.1.1), one finds that the probability of detecting a signal photon at the detector carries the information of the phase difference applied between the sources:

$$p_s = 2p_0^2 p_1^2 \left(1 + cos\Delta\gamma\right). \tag{5.8}$$

5.2. Experimental configuration

A schematic of the photonic integrated circuit (PIC) designed for phase measurements with undetected photons is detailed in Fig. 5.2. The sources used in this experiment are the multimode waveguides described in Sect. 1.2.2. The pumps p_0 and p_1 are beams on the transverse electric fundamental (TE0) and first excited (TE1) optical modes at wavelength 1561 nm, and phase matching is met with the signal and idler photons in the TE0 and TE1 modes, respectively, at 1291.6(5) nm and 1972(1) nm.

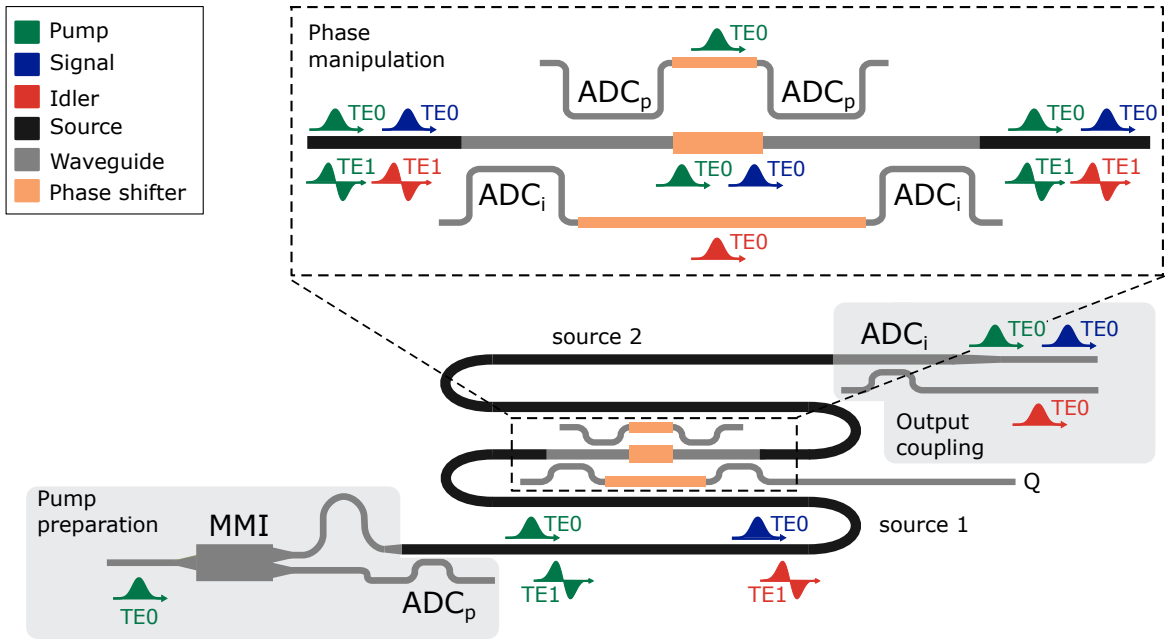

Figure 5.2.: Chip design. Schematic of the integrated circuit. MMI: multimode interferometer. ADC: asymmetric directional coupler. The subscript $j = p$ ($j = i$), indicates the ADC designed to couple efficiently in the spectral region of the pump (idler). Q indicates an additional output used for the phase characterization. This scheme is not in scale.

To prepare the pump beams in the TE0 and TE1 optical modes, a tapered lensed fiber is edge-coupled to the chip to couple a CW laser beam. The on-chip power is 5 mW. The laser beam is split on-chip with a 1×2 50:50 multimode interferometer (MMI).

An MMI [85] is a broad multimode waveguide that supports a large number of modes, each of which propagates independently. The modes interfere in the structure. Since modes are characterized by different effective refractive indexes n_{eff}, they propagate with different phase velocities $v_p = c/n_{\text{eff}}$. Therefore, the resulting interference exhibits a dependence on the propagation length. By designing an MMI of a specific length and locating the output port at the maximums of the interference, one can split the input mode into as many modes as needed. In the case of interest of the design pictured in Fig. 5.2, the length and width of the MMI are 55.4 μm and 12 μm, respectively, and it is designed to behave as a 3 dB power splitter in the C-band.

At the MMI output, in the design, two coherent identical beams are collected by two single-mode waveguides, one of which adiabatically broadens to a multimode waveguide. With an asymmetric directional coupler [86] (ADC), the TE0 pump beam propagating in the single-mode waveguide is coupled to the TE1 optical mode supported by the multimode waveguide.

As it was already introduced in Sect. 1.1.2, a directional coupler allows coupling light from one

waveguide to another through the evanescent field. Under the phase matching condition, the mode propagating in one waveguide excites the mode of a waveguide located in close proximity, and the mode can be transferred from one waveguide to the other. In an ADC, the coupling occurs between modes of different order. In the case of this specific design, the coupling occurs between the fundamental transverse-electric mode TE0 in a single-mode waveguide and the first-excited mode TE1 of a multimode waveguide. The length of an (A)DC can be chosen to implement a desired power splitting ratio. In this work, ADCs are designed such that the power is totally transferred from one waveguide to another.

The pumps propagate in the first nonlinear optical source, which is a 7.5 mm long multimode channel waveguide made of silicon embedded in silica, with a cross-section of 220 nm $\times$ 2 μm. After the first source there is a phase manipulation stage, where the pump p_1 and the generated idler photons are individually separated with a system of ADCs. Phases on-chip are selectively applied by using thermo-optic phase shifters. The geometries of the ADC used in this work are listed in Tab.5.1.

	Width SM	Width MM	Height	Coupling length
ADC pump	0.45 μm	0.935 μm	0.22 μm	28.6 μm
ADC idler	0.8 μm	1.85 μm	0.22 μm	58.3 μm

Table 5.1.: Design specifics for the ADCs. The width and the height refer to the cross-section dimensions of the core of a channel waveguide, while the length corresponds to the dimension along the modes' propagation direction. For the ADCs, phase matching is met between the mode propagating in the single-mode waveguide and the first excited optical mode in the multimode waveguide. The coupling distance, i.e., the distance between the waveguides of the ADC, is of 0.2 μm. SM: single-mode waveguide. MM: multimode waveguide.

After the phase manipulation stage, the pumps, the signal, and the idler are recombined and fed into the second source. With this spatial superposition, the path indistinguishability of the generated photons is preserved. Finally, at the output coupling stage, the signal and idler are separated by means of an ADC. The multimode waveguide in which the pumps and the signal propagate tapers off to a single-mode waveguide to radiate the TE1 pump mode in the cladding of the integrated circuit. The idler and the residual p_0 pump are out-coupled with a tapered lensed fiber. The signal is isolated from the pump, the idler, and the Raman noise by cascading two fiber-based notch filters with a center wavelength of 1550 and a bandwidth of 30 nm and two fiber-based band-pass filters with a 1290 nm center wavelength and 15 nm bandwidth, achieving more than 40 dB and 100 dB suppression for Raman and pump noise, respectively. The signal is detected by an InGaAs single-photon avalanche diode in free-running with 10 % detection efficiency and 1 μs dead time, which also provides further suppression of idler photons, being sensitive up to 1700 nm wavelengths only.

5.3. Phase measurement procedure

The objective of this experiment is to retrieve the phase applied to the idler by only detecting the signal. In order to do so, it is necessary to perform a calibration measurement of the setup with no phase applied to the idler. By varying any other phase, an interference pattern in the signal photon counts is observed. This is the case I already discussed for SPDC in Sect. 2.5. In this experiment, I varied the phase γ_{p_1}. The interference observed in the signal photon counts (C) in this reference measurement (ref) is

$$C_{\text{ref}} \propto 1 + cos(\gamma_{p_1} + \bar{\gamma}), \tag{5.9}$$

with $\bar{\gamma}$ a constant. By performing a similar measurement when a phase γ_i is applied to the idler, the interference observed in the signal counts is

$$C \propto 1 + cos(\gamma_{p_1} - \gamma_i + \bar{\gamma}). \tag{5.10}$$

Therefore, the interference pattern should be phase-shifted with respect to the calibration target by the amount γ_i. By comparing the two measurements, one derives γ_i.

5.4. Current-phase characterization

In this experiment, phases are applied by means of thermo-optic phase shifters using current-controlled metallic heaters. The heaters are placed above the waveguide, and when a current is flown through them, their temperature increases due to the Joule effect. The variation in temperature leads to a change in the refractive index experienced by the modes in the nearby waveguides, and the modes acquire an additional phase contribution due to the variation in the refractive index. Specifically, a variation Δn in the refractive index leads to a variation in the wavevector of the propagating photons. If the length of the resistor is L, the photons experience the variation of refractive index in the path L. It follows that the phase γ acquired by the photons is directly proportional to Δn, and linearly increases with L. The refractive index depends linearly on the temperature [87], therefore a variation in the refractive index is proportional to the temperature variation, which is proportional to the power P dissipated by the resistor. Therefore, γ is proportional to P:

$$\gamma \propto \Delta n \propto \Delta T \propto P. \tag{5.11}$$

My main contribution to the experiment discussed in this chapter was to find a way to correctly associate the current applied at the thermo-optic shifters to the phase acquired by the photons propagating in the nearby waveguide, since the PIC did not include a phase-characterization structure. Nevertheless, even with a dedicated structure to characterize the phase shifters, e.g., a separated integrated Mach-Zehnder interferometer featuring phase shifters identical to those in the design, the idler is in a spectral region where the efficiency of the detectors is limited or they do not exist yet, and therefore a direct wavelength-dependent characterization of the phase shifters would be challenging. Therefore, I experimentally characterized the resistivity of the heaters as a function of the applied current and simulated the local variation in the refractive index due to the Joule effect at the desired wavelength.

The power dissipated via the Joule effect depends on the current as [88]

$$P = R(T) \times I^2, \tag{5.12}$$

where the temperature-dependent resistance R of the resistor can be written as a function of its geometrical parameters and as a function of the resistivity of the material ρ:

$$R(T) = \frac{L}{w \times h}\rho(T). \tag{5.13}$$

L, w and h are respectively the length, the width, and the height of the resistor. Here I neglect the dependence of the geometry on the temperature, as the low thermal expansion coefficient is one of the primary requirements for embedding the resistor in the PIC to avoid local stress and damage. In limited temperature ranges, the resistivity depends linearly on the temperature

$$\rho(T) = m'T + q', \tag{5.14}$$

where m' and q' are constants. The temperature variation ΔT, which is the variation with respect to the case in which $I = 0$, is proportional to P [88], therefore the temperature depends linearly on the dissipated power:

$$\Delta T = T(I) - T(0) \propto P(I) \qquad \longrightarrow \qquad T(I) = \alpha P(I) + \beta, \tag{5.15}$$

where α and β are some constants. At the first-order approximation, I assume the dissipated power to be proportional to the square of the current, i.e., I assume $P \propto I^2$, neglecting the dependence of the resistance on the temperature in Eq. (5.12). Therefore, Eq. (5.15) transforms into

$$T = \alpha' I^2 + \beta' \qquad \text{(first-order approximation)}, \tag{5.16}$$

with α' and β' constants. Therefore, Eq. (5.14) transforms to

$$\rho(I) = mI^2 + q, \tag{5.17}$$

where m and q are constants.

In a recursive approach, I feed Eq. (5.17) into Eqs (5.12) and (5.13), and I derive the dissipated power as a function of the current

$$P = \frac{L}{w \times h}(mI^2 + q) \times I^2. \tag{5.18}$$

According to the arguments above, the phase γ acquired due to the phase shifters is proportional to P. If γ were the phase acquired by a beam in a branch of a Mach-Zehnder interferometer, I would expect to observe at the output of the interferometer an interference pattern in the intensity $\mathcal{I}$ that depends on the current I as[1]

$$\mathcal{I} = A\left\{\sin\left[\left(bI^2 + c\right)I^2 + \varphi_0\right] + 1\right\}, \tag{5.19}$$

where A, b, c, and φ_0 are constants.

Fig. 5.3(a) shows a schematic of the phase manipulation stage. It labels the phase shifters as "1", "2", and "3" and it shows an additional output that can be accessed (Q). The pump contributions at Q are highlighted in Fig. 5.3(b). Indeed, the pump contributions at Q are given by the pump component p_1 that spuriously couples to the idler ADC. Each pump path is located close to a distinct heater in the phase manipulation stage: when varying the current at any phase shifter, an interference pattern in the residual pump is observed at the output. If only one phase is varied, the structure is a Mach-Zehnder interferometer.

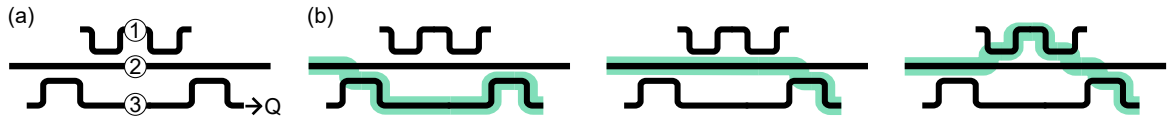

Figure 5.3.: Schematic of the phase manipulation stage. (a) The circles represent the phase shifters, with the corresponding labels. Q labels a secondary output on the PIC. (b) Schematic of the phase manipulation stage qualitatively showing the contributions of the pump p_1 at the secondary output. p_1 partially couples with the idler ADC (left), propagates along the central waveguide (middle), and couples with the pump ADC (right).

[1]The interference pattern, as a function of γ, is expected to be $\mathcal{I} = A\sin^2\frac{\gamma}{2}$. Here I used the identity relation $\sin^2\frac{\gamma}{2} = \frac{1}{2}\left[\sin\left(\gamma - \frac{\pi}{2}\right) + 1\right]$. This choice has been done due to the convenience of performing data fits that goes as a sinusoidal rather than a sinusoidal squared.

The experimental results for the residual pump intensity at the output Q are shown in Fig. 5.4(a), minus a DC component that has been experimentally derived. The data shown in Fig. 5.4(a) have been obtained by varying the current at the phase shifter 1, with the PIC fed with a CW laser at a wavelength of 1568 nm.

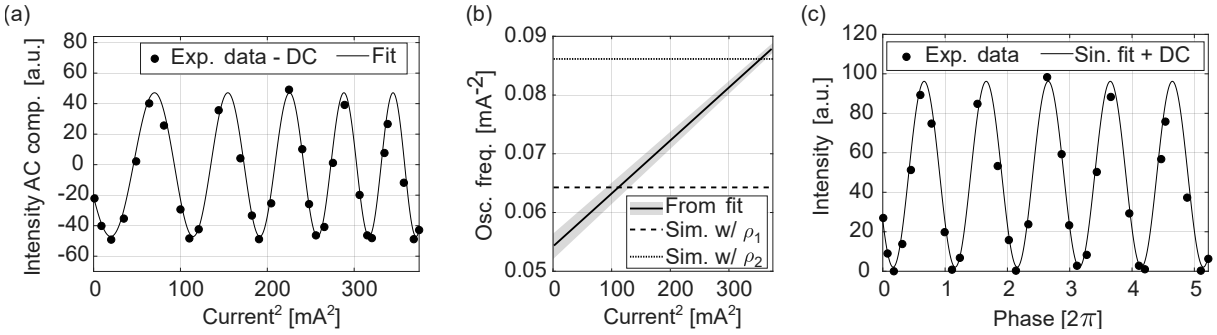

Figure 5.4.: Experimental data for the characterization of the resistor 1. (a) Pump intensity at output Q, minus a DC component, as a function of the current squared applied at the resistor 1. Dots: experimental data. Line: fit results with fitting function $A \sin\left[\left(bI^2 + c\right) I^2 + \varphi_0\right]$, with A, b, c and φ_0 parameters of the fit. (b) Oscillation frequency as a function of the current squared. Solid line: result of the fit (black line) with its uncertainty (gray area, solid). Dashed line: results of a simulation with resistivity $\rho_1 = 0.18\,\Omega\mu m$. Dotted line: results of a simulation with resistivity $\rho_2 = 0.24\,\Omega\mu m$. (c) Pump intensity at output Q as a function of the phase γ, with γ characterized from the oscillation frequency in the interference pattern. Dots: experimental data. Line: fit result with fitting function $A' \sin\left(b'\gamma + \varphi_0'\right) + \mathrm{DC}$, with A', b' and φ_0' fit parameters and DC the DC component of the experimental data. The resulting oscillating period is $0.996(8) \times 2\pi$.

I fitted the AC component in the interference pattern with the AC component of the function in Eq. (5.19) and derived the fit parameters A, b, c, and φ_0. From the coefficients b and c, I derived the current-dependent oscillation frequency $f(I) = bI^2 + c$ as a function of the current square.

I simulated with COMSOL Multiphysics the effective index experienced by the pump modes as a function of the current for a fixed value of the resistivity ρ_1, since the simulation does not take into account the dependence of the resistivity on the temperature. I found the interference pattern at the output of a Mach-Zehnder interferometer as a function of the applied current, using the simulated refractive indexes. The interference pattern exhibits a constant oscillation frequency f_1, since it assumes a constant resistivity ρ_1. I compared this constant oscillation frequency obtained in this simulation with the current-dependent oscillation frequency derived experimentally. The oscillation frequency of the simulation meets the experimental data when the current has the value I_1. Therefore, I derived that the resistivity at I_1 is ρ_1. I repeated the same procedure for another value of fixed resistivity ρ_2 and found correspondence with the experimental data for the current value I_2. Fig. 5.4(b) shows the comparison between the simulations and oscillation frequency derived from fitting the experimental data. In Eq. (5.17), the relation between the resistivity and the current square is linear, which allows deriving the coefficients m and q in Eq. (5.17).

The same procedure has been followed for the resistor "3". The results are summarized in Tab. 5.2.

Note that q is the resistivity of the resistance at room temperature, i.e., when the current $I = 0$. The obtained values are compatible with the value declared by the manufacturer ($0.15\ \Omega\,\mu m$).

Finally, I used these results to simulate the effective refractive indexes experienced by the propagating modes as a function of the current applied. This simulation takes into account the

Resistor label	$m\left[\Omega\frac{\mu m}{mA^2}\right]$	$q\ [\Omega\,\mu m]$
1	$2.5(2)\times10^{-4}$	0.152(8)
3	$2.2(5)\times10^{-4}$	0.16(3)

Table 5.2.: Results in the characterization of the resistivity coefficients when the resistivity is described by Eq. (5.17).

dependence of the resistivity on the current as in Eq. (5.17). With the effective refractive indexes and the resistor length, I found a map that associates the current applied to the resistor to the phase acquired by the propagating mode. Fig. 5.4(c) shows the interference pattern at the Mach-Zehnder interferometer output Q as a function of the phase characterized in this way when applying a current to the resistor "1".

The important result of this characterization is that it allows deriving the phase applied to any mode propagating in the waveguide nearby the resistor: once the resistivity is characterized, the thermo-optic properties of the material can be simulated. The results do not depend on the geometry of the resistor. As an example, the values derived for the resistors 1 and 3 and listed in Tab. 5.2 are compatible even though they present different geometries, as it is listed in Tab. 5.3.

	Width	Height	Length
Pump p_1	0.6 μm	0.3 μm	204.0 μm
Pump p_0 and signal	0.6 μm	0.3 μm	204.0 μm
Idler	0.6 μm	0.3 μm	534.8 μm

Table 5.3.: Geometry of the phase shifters, placed 1 μm above the corresponding waveguide. The length, height, and width of the resistors are defined consistently with the corresponding dimensions of the waveguides on the chip.

The simulated effective refractive indexes as a function of the driving current for the pump and the idler obtained with the resistor characterization are shown in Fig. 5.5(a).

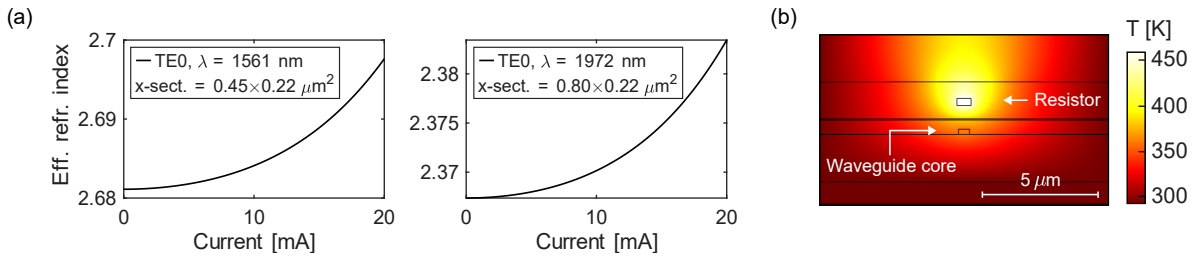

Figure 5.5.: Simulated effective refractive indexes and simulation for the evaluation of thermal cross-talk effects. (a) Effective refractive index as a function of the current applied to the resistor, for the pump (left) and the idler (right). λ: wavelength; x-sect: waveguide cross-section. (b) Simulation of the temperature on the waveguide cross-section for a driving current of 20 mA.

5.4.1. Thermal cross-talk effects

I evaluated the possibility of thermal cross-talk effects between the heaters. I simulated temperature distribution on the waveguide cross-section. The results of the simulation, for a driving current of 20 mA, are shown in Fig. 5.5(b). In this case, the thermal cross-talk appears to be negligible at a distance of 5 μm from the waveguide. In the design, the closer distances

between the heaters and the nearby waveguides are between the idler phase shifter and source 1, with a distance of 8 μm, and between the pump phase shifter and source 2, with a distance of 7.45 μm. Therefore, I assumed the thermal cross-talk effects to be negligible. Moreover, even though the phase shifters were characterized for a driving current between 0 and 20 mA, the final experiment has been carried out with a driving current that did not exceed 15 mA.

5.5. Spurious pump phase-shift characterization

As a preliminary measurement, the classic behavior of the circuit was characterized by monitoring the residual pump intensity at the signal output as a function of γ_{p1} and γ_i. In this way, a phase contribution on the pump was measured as the idler phase shifter was operated, as reported in Fig. 5.6(a). This behavior was attributed to a spurious coupling of part of the pump p_1 to the first idler ADC (ADC$_i$), which was estimated in about 10%. When applying a phase γ_i to the idler, the part of the pump leaking into the idler phase-shifting arm gets an additional spurious phase contribution[2] φ_p. Moreover, being also the pump ADC not 100% efficient, some of the p_1 power does not couple to the pump phase-shifting arm. The p_1 beam is thus taking three different paths, as illustrated in Fig. 5.6(b), giving rise to a three-branch interferometer.

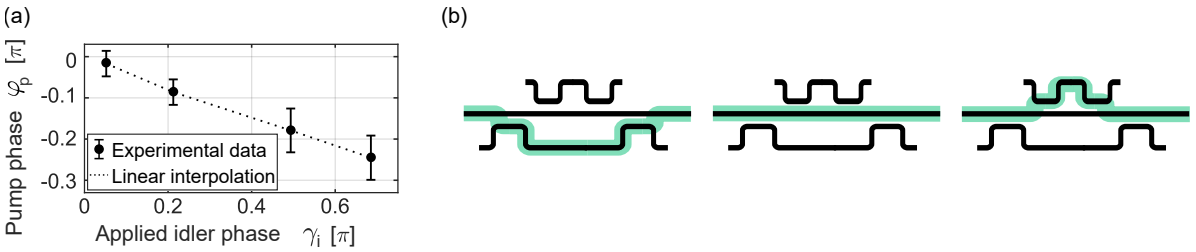

Figure 5.6.: (a) Experimental characterization of the correlation between a spurious pump phase contribution φ_p and an applied idler phase γ_i. The pump wavelength is 1561 nm. (b) Schematic of the phase manipulation stage qualitatively showing the contributions of the pump p_1 at the input of the second source. p_1 partially couples with the idler ADC (left), propagates along the central waveguide (middle), and couples with the pump ADC (right).

This additional pump phase contribution must be taken into account in the interference pattern. Therefore, Eq. (5.10) should be modified in

$$C \propto 1 + cos(\gamma_{p_1} + \varphi_p(\gamma_i) - \gamma_i + \bar{\gamma}). \tag{5.20}$$

This means that the phase shift observed in the signal photon counts with respect to the reference measurement will carry not only the phase γ_i, but also the additional phase contribution φ_p.

5.6. Experimental results

Following the procedure described in Sect. 5.3, I swept the pump phase γ_{p_1} to observe single-photon interference in the idler photon counts when applying a phase γ_i to the idler. In Fig. 5.7(a), I report two interference measurements, with $\gamma_i = 0$ and $\gamma_i = 0.21\pi$. As expected, the interference patterns are phase-shifted, as the idler carries different phase information in the

[2]The spurious contribution is indicated with the letter φ to discriminate it from the voluntarily induced phase shift γ.

two measurements. The same procedure has been followed for four different values of γ_i, and each interference pattern was compared with a reference measurement taken with $\gamma_s = 0$. The experimental values for $\Delta\gamma_s$, i.e., the phase shift experienced by the signal interferogram with respect to its reference, are reported in Fig. 5.7(b), as a function of γ_i. When correcting the measured $\Delta\gamma_s$ by the phase shift φ_p experienced by the pump, the idler phase can be retrieved. Indeed, Fig. 5.7(c) shows a one-to-one correspondence between the global measured phase shift $\gamma_{\mathrm{UP}} = \Delta\gamma_s - \varphi_p$ and the phase applied to the signal photons γ_s.

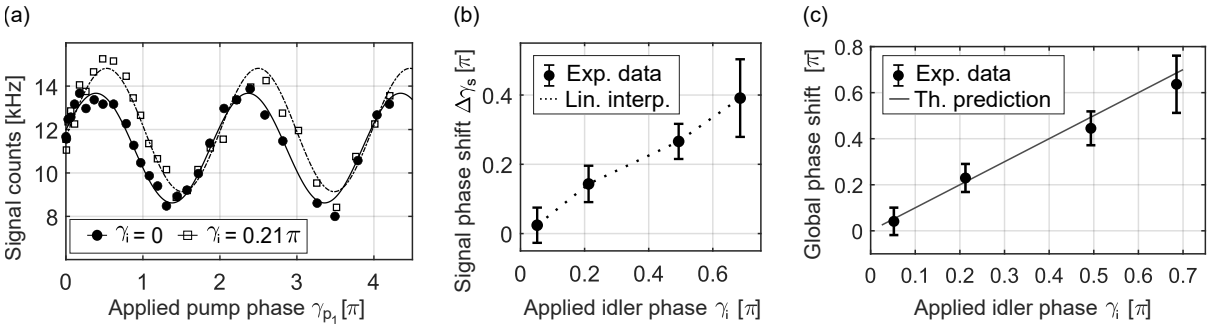

Figure 5.7.: Experimental results. (a) Signal counts as a function of γ_{p_1}, for $\gamma_i = 0$ and $\gamma_i = 0.21\pi$. Dots: experimental data after the subtraction of the dark counts (325 Hz). The integration time per point is 1 s. The marker size is larger than the error bar. Lines: sinusoidal fit. The fitting function is of the form $Counts = a \times \sin(b\gamma_{p_1} + c) + d$, with a, b, c and d parameters of the fit. (b) Signal phase shift $\Delta\gamma_s$ as a function of γ_i. (c) Correspondence between the experimental data (dots) and the theoretical prediction (line).

Therefore, in this experiment, I retrieved the phase information of the idler photons at around 2 μm by only detecting photons in the O-band. The experiment has been performed with an integrated design in which the whole nonlinear interferometer, including photon pair generation and phase probing stages, is integrated on the same chip, resulting in significantly enhanced miniaturization and robustness compared to bulk UP systems. Moreover, since the optical modes supported by an integrated structure are spatially confined, alignment between the sources is guaranteed, maximizing their spatial indistinguishability [13].

Conclusions

Quantum interference with undetected photons is a technique that allows decoupling the probing and the detection stages in active sensing scenarios. In particular, it allows decoupling the probing and the detection wavelengths, making it possible to use probing photons that are strongly resonant with the target, and detected photons in a spectral region where the detection technologies are mature and efficient. This provides the dual advantage of enhanced measurement sensitivity, together with good responsivity of the target. Moreover, decoupling the probing and the detection wavelengths allows probing the target with long wavelengths, enabling non-invasive, low-energy imaging.

In this thesis, I presented the work I carried out during my doctoral studies. I realized a state-of-the-art setup for quantum imaging with undetected photons. Among the results that are in line with the state-of-the-art experiments, I studied and simulated the spatial correlation between the idler and signal photons, which enables the imaging capabilities of a free-space nonlinear optical photon-pair source. This work has been used to validate the experimental results in [30].

The research questions of this thesis were whether undetected photon techniques could be extended to practical imaging and detection scenarios for diffuse targets and whether the standard configuration could be implemented in an integrated photonic design.

The novel contribution of this thesis is twofold.

First, it proposes and validates an experimental implementation for extending the technique of imaging with undetected photons for imaging a diffusive target [31]. Indeed, the interference visibility in an experiment of imaging with undetected photons is heavily affected in the interaction with a diffusive target, due to the distinguishability that it introduces between the two probabilistic generation processes. A large limitation is due to the change in the angular distribution due to the interaction with the target. The approach described in this thesis consists of providing an angular distribution to the photons before their interaction with the target to maximize the indistinguishability between the generation processes. The perspective of this work is to expand the applicability of the technique to in vivo biomedical imaging and, more generally, to scenarios in which precise alignment of the target with an optical element beyond it is impractical. The prospects for improvement are engineering-based: automated, fast, and densified data acquisition would allow for a higher image resolution.

Second, this thesis presented the first experiment of sensing with undetected photons on a photonic integrated circuit. The integrated platform holds the promise for the production of miniaturized commercial devices that are compatible with the consumer electronics, enabling the development of integrated refractometric sensors based on undetected photons. This work was published in [28, 29].

In conclusion, this thesis constitutes a step forward for practical applications of quantum interference with undetected photons. It demonstrates an imaging configuration suitable for diffusive targets and a design for quantum phase measurements with undetected photons on a photonic integrated circuit.

A. Detailed calculations

This appendix presents the calculations that were omitted from the main text for brevity.

A.1. Induced coherence without induced emission

Here I present the calculation for different configurations for the experiment of induced coherence without induced emission, outlined in Chap. 2.

I keep the general assumption in which the unitary transformation associated to the experiment can be written as

$$\hat{\mathcal{U}} = \hat{\mathbb{1}} + \hat{\mathcal{H}}_{eff\,1} + \hat{\mathcal{H}}_{eff\,2}, \tag{A.1}$$

where

$$\hat{\mathcal{H}}_{eff\,1} = \tilde{p}_1 \hat{a}^\dagger_{s_1} \hat{a}^\dagger_{i_1} + h.c. \quad \text{and} \quad \hat{\mathcal{H}}_{eff\,2} = \tilde{p}_2 \hat{a}^\dagger_{s_2} \hat{a}^\dagger_{i_2} + h.c. \tag{A.2}$$

The differences between the configurations discussed below rely on the different transformations to which the creation operators $\hat{a}^\dagger_{s_1}$ and $\hat{a}^\dagger_{i_1}$ are subjected.

A.1.1. Configuration 1: Cascaded sources

Two distinct sources, all paths superposed, losses on idler, phases applied to pump, signal, and idler

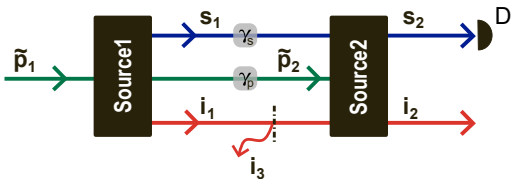

Figure A.1.: Same as Fig. 2.4(a). Cascaded configuration. A classical beam with amplitude $\tilde{p}_1$ pumps a nonlinear optical source, and signal and idler are generated in the modes s_1 and i_1, respectively. Photons in the mode s_1 acquire a phase γ_s. A phase γ_p is applied to the residual pump, which is used to pump a second nonlinear source. In the second source are generated the signal and idler modes s_2 and i_2. The idler in mode i_1 interacts with a beam splitter, and the transmitted modes are superposed with i_2. Lost idler modes are labeled as i_3. Photons in mode s_2 are measured with a photodetector (D).

A phase γ_s is applied to the signal mode s_1, the idler mode i_1 is subjected to losses modeled with a beam splitter of complex transmittance $te^{i\gamma_i}$, and a phase is applied to the pump. Neither the signal mode nor the pump is subjected to losses.

$$\hat{a}^\dagger_{s_1} = \mathrm{e}^{i\gamma_s}\hat{a}^\dagger_{s_2}, \quad \hat{a}^\dagger_{i_1} = t\mathrm{e}^{i\gamma_i}\hat{a}^\dagger_{i_2} + \sqrt{1-t^2}\hat{a}^\dagger_{i_3}, \quad \tilde{p}_2 = \mathrm{e}^{i\gamma_p}p, \quad \text{and} \quad \tilde{p}_1 = p \tag{A.3}$$

Being the initial state the vacuum state,

$$|\psi_0\rangle = |0\rangle_{s_2} |0\rangle_{i_2} |0\rangle_{i_3} = |0\rangle_s |00\rangle_i \,, \tag{A.4}$$

and the final state

$$|\psi\rangle = \hat{\mathcal{U}} |\psi_0\rangle = |0\rangle_s |00\rangle_i + \tilde{a} |1\rangle_s |10\rangle_i + \tilde{b} |1\rangle_s |01\rangle_i \,, \tag{A.5}$$

where the complex amplitudes are

$$\tilde{a} = p\, \mathrm{e}^{i(\gamma_s+\gamma_i)} \left(t + \mathrm{e}^{i\Delta\gamma}\right), \qquad \text{and} \qquad \tilde{b} = p\sqrt{1+t^2}\, \mathrm{e}^{i\gamma_s}. \tag{A.6}$$

The reduced density matrix for the signal states is found by tracing out the idler states:

$$\begin{aligned} \hat{\rho}_s &= \langle 00|_i |\psi\rangle \langle\psi|00\rangle_i + \langle 10|_i |\psi\rangle \langle\psi|10\rangle_i + \langle 01|_i |\psi\rangle \langle\psi|01\rangle_i \\ &= |0\rangle_s \langle 0|_s + \left(|\tilde{a}|^2 + \left|\tilde{b}\right|^2\right) |1\rangle_s \langle 1|_s \,. \end{aligned} \tag{A.7}$$

And the probability of detecting a signal photon, i.e., the probability for a signal photon to be in the mode s_2, is

$$p_s = |\tilde{a}|^2 + \left|\tilde{b}\right|^2 = 2\,p^2(1 + t\cos(\Delta\gamma)) \tag{A.8}$$

The visibility of the interference pattern is equal to the modulus of the complex transmittance of the beam splitter interacting with the idler mode i_1:

$$v = t \tag{A.9}$$

A.1.2. Configuration 2: Folded

One source employed twice in a folded configuration, all paths superposed, losses on idler, phases applied to pump, signal, and idler

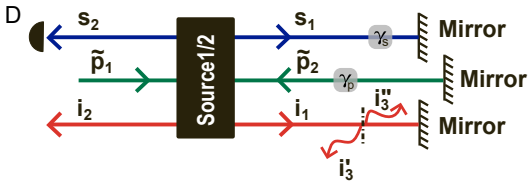

Figure A.2.: Same as Fig. 2.4(b). Folded configuration. A classical beam with amplitude $\tilde{p}_1$ pumps a nonlinear optical source from left to right. A phase γ_p is applied to the residual pump, which is reflected by a mirror. The pump beam interacts again with the phase shifter and pumps the nonlinear source from right to left with complex amplitude $\tilde{p}_2$. From left to right, the modes s_1 and i_1 are generated. The mode s_1 interacts with a phase shifter characterized by γ_s, is reflected by a mirror, and interacts with the phase shifter again, acquiring a global phase $2\gamma_s + \pi$. The idler mode i_1 is transmitted with complex amplitude $te^{i\gamma_i}$. The transmitted mode is reflected by a mirror and experiences the interaction with the beam splitter characterized by transmittance $te^{i\gamma_i}$. The transmitted modes are superposed with the modes s_2 and i_2. The lost idler modes in the propagation from left to right are labeled as i_3', and i_3'' from right to left. Photons in the mode s_2 are detected with a photodetector.

The signal generated in the mode s_1 interacts with a phase shifter, is reflected by a mirror and interacts with the phase shifter a second time

$$\hat{a}^\dagger_{s_1} = \mathrm{e}^{i\gamma_s}\mathrm{e}^{i\pi}\mathrm{e}^{i\gamma_s}\hat{a}^\dagger_{s_2} = \mathrm{e}^{i(2\gamma_s)}\hat{a}^\dagger_{s_2} \tag{A.10}$$

The idler mode i_1 is subjected to losses, such that

$$\begin{aligned}\hat{a}^\dagger_{i_1} &= t\,\mathrm{e}^{i\gamma_i}\hat{a}^\dagger_{i'_1} + \sqrt{1-t^2}\hat{a}^\dagger_{i'_3} \\ &= t\,\mathrm{e}^{i\gamma_i}\left(\mathrm{e}^{i\pi}t\mathrm{e}^{i\gamma_i}\hat{a}^\dagger_{i_2} + \sqrt{1-t^2}\hat{a}^\dagger_{i''_3}\right) + \sqrt{1-t^2}\hat{a}^\dagger_{i'_3} \\ &= -t^2\,\mathrm{e}^{i(2\gamma_i)}\hat{a}^\dagger_{i_2} + \sqrt{1-t^2}\hat{a}^\dagger_{i'_3} + t\sqrt{1-t^2}\hat{a}^\dagger_{i''_3}\end{aligned} \tag{A.11}$$

where $\hat{a}^\dagger_{i'_1}$ is the creation operator for the transmitted mode i'_1, $\hat{a}^\dagger_{i'_3}$ is the creation operator for the mode lost in the propagation from left to right (see Fig. A.2) and $\hat{a}^\dagger_{i''_3}$ is the creation operator for the mode lost in the propagation from right to left.

The pump interacts with a phase shifter twice between the crystals

$$\tilde{p}_2 = \mathrm{e}^{i(2\gamma_p)}p, \qquad \text{and} \qquad \tilde{p}_1 = p. \tag{A.12}$$

The initial state is the vacuum state

$$|\psi_0\rangle = |0\rangle_{s_2}|0\rangle_{i_2}|0\rangle_{i'_3}|0\rangle_{i''_3} = |0\rangle_s|000\rangle_i\,, \tag{A.13}$$

and the final state is obtained by applying the transformation $\hat{\mathcal{U}}$:

$$\begin{aligned}|\psi\rangle &= \hat{\mathcal{U}}|\psi_0\rangle \\ &= |0\rangle_s|000\rangle_i + \tilde{a}\,|1\rangle_s|100\rangle_i + \tilde{b}\,|1\rangle_s|010\rangle_i + \tilde{c}\,|1\rangle_s|001\rangle_i\,,\end{aligned} \tag{A.14}$$

where

$$\tilde{a} = p\,\mathrm{e}^{2i(\gamma_s+\gamma_i)}\left(t^2 + \mathrm{e}^{2i\Delta\gamma}\right), \quad \tilde{b} = -p\sqrt{1-t^2}\,\mathrm{e}^{i2\gamma_s} \quad \text{and} \quad \tilde{c} = -p\,t\sqrt{1-t^2}\,\mathrm{e}^{i(2\gamma_s+\gamma_i)}. \tag{A.15}$$

The reduced density matrix is found tracing out the idler states

$$\begin{aligned}\hat{\rho}_s &= \langle 000|_i|\psi\rangle\langle\psi|000\rangle_i + \langle 100|_i|\psi\rangle\langle\psi|100\rangle_i + \langle 010|_i|\psi\rangle\langle\psi|010\rangle_i + \langle 001|_i|\psi\rangle\langle\psi|001\rangle_i \\ &= |0\rangle_s\langle 0|_s + \left(|\tilde{a}|^2 + \left|\tilde{b}\right|^2 + |\tilde{c}|^2\right)|1\rangle_s\langle 1|_s\,,\end{aligned} \tag{A.16}$$

and the probability of detecting a signal photon in the mode s_2 is

$$p_s = |\tilde{a}|^2 + \left|\tilde{b}\right|^2 + |\tilde{c}|^2 = 2\,p^2(1 + t^2\cos(2\Delta\gamma)) \tag{A.17}$$

The visibility of the interference pattern is

$$v = t^2. \tag{A.18}$$

Both the visibility and the phase shift in the interference pattern take into account that the idler mode generated from left to right in Fig. A.2 interacts with the object of complex transmittance $te^{i\gamma_i}$ twice.

One source employed twice in a folded configuration, all paths superposed, losses and phases on pump, signal, and idler

Here, I include the possibility that the signal and the pump can be subjected to losses between the generation processes in the folded configuration. Without loss of generality, I assume that the signal and the pump are subjected to losses characterized by real amplitude, and phases are applied to the signal and the pump with an additional phase manipulation stage. The configuration is schematized in Fig. A.3.

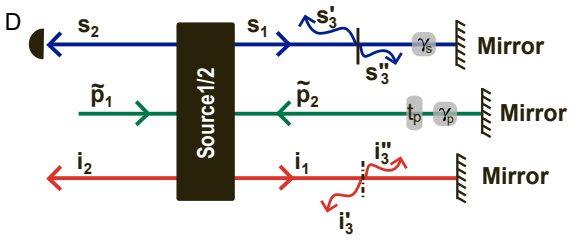

Figure A.3.: Induced coherence without induced emission: folded configuration with losses on all modes. The modes generated from left to right are subjected to losses, as well as the pump from right to left.

The signal generated in the mode s_1 is transmitted with real probability amplitude t_s, and is superposed with the mode s_1'. Lost modes in this propagation from left to right (see Fig. A.3) are labeled as s_3'. The mode s_1' experiences a phase shift γ_s, is reflected with a mirror (phase shift π) and interacts again with the phase shifter characterized by γ_s. This mode is transmitted with probability t_s and superposed with the mode s_2. The mode for photons lost along the propagation from right to left are labeled as $s_3{}''$.

$$\begin{aligned}\hat{a}^\dagger_{s_1} &= t_s \hat{a}^\dagger_{s_1'} + \sqrt{1-t_s^2}\hat{a}^\dagger_{s_3'} \\ &= t_s \mathrm{e}^{i(2\gamma_s)}\mathrm{e}^{i\pi}\left(t_s \hat{a}^\dagger_{s_2} + \sqrt{1-t_s^2}\hat{a}^\dagger_{s''_3}\right) + \sqrt{1-t_s^2}\hat{a}^\dagger_{s_3'} \\ &= -t_s^2 \mathrm{e}^{i(2\gamma_s)}\hat{a}^\dagger_{s_2} + \sqrt{1-t_s^2}\hat{a}^\dagger_{s_3'} - t_s\sqrt{1-t_s^2}\mathrm{e}^{i(2\gamma_s)}\hat{a}^\dagger_{s''_3}\end{aligned} \tag{A.19}$$

The idler mode i_1 is subjected to losses, and the result for $\hat{a}^\dagger_{i_1}$ is the same as in Eq. (A.11). Here I added the subscript i to the modulus of the amplitude for the idler mode to be transmitted to differentiate it from the probability of transmittance for the signal mode:

$$\hat{a}^\dagger_{i_1} = -t_i^2\, \mathrm{e}^{i(2\gamma_i)}\hat{a}^\dagger_{i_2} + \sqrt{1-t_i^2}\hat{a}^\dagger_{i_3'} + t_i\sqrt{1-t_i^2}\hat{a}^\dagger_{i''_3} \tag{A.20}$$

The pump

$$\tilde{p}_2 = t_p^2\, \mathrm{e}^{i(2\gamma_p)}p, \qquad \text{and} \qquad \tilde{p}_1 = p. \tag{A.21}$$

The initial state is the vacuum state:

$$|\psi_0\rangle = |0\rangle_{s_2}|0\rangle_{s_3'}|0\rangle_{s''_3}|0\rangle_{i_2}|0\rangle_{i_3'}|0\rangle_{i''_3} = |000\rangle_s\,|000\rangle_i\,. \tag{A.22}$$

The final state is found by applying the transformation $\hat{\mathcal{U}}$ to the initial vacuum state:

$$\begin{aligned}|\psi\rangle &= \hat{\mathcal{U}}\,|\psi_0\rangle \\ &= |000\rangle_s\,|000\rangle_i + \tilde{a}\,|100\rangle_s\,|100\rangle_i + \tilde{b}\,|100\rangle_s\,|010\rangle_i + \tilde{c}\,|100\rangle_s\,|010\rangle_i + \\ &\quad + \tilde{d}\,|010\rangle_s\,|100\rangle_i + \tilde{e}\,|010\rangle_s\,|010\rangle_i + \tilde{f}\,|010\rangle_s\,|001\rangle_i +, \\ &\quad + \tilde{g}\,|001\rangle_s\,|100\rangle_i + \tilde{h}\,|001\rangle_s\,|010\rangle_i + \tilde{j}\,|001\rangle_s\,|001\rangle_i\end{aligned} \tag{A.23}$$

with

$$\tilde{a} = p\,\mathrm{e}^{i2(\gamma_s+\gamma_i)}\left(t_s^2 t_i^2 + t_p^2 \mathrm{e}^{i2\Delta\gamma}\right), \qquad \tilde{b} = -p\,t_s^2\sqrt{1-t_i^2}\mathrm{e}^{i2\gamma_s},$$
$$\tilde{c} = -p\,t_s^2 t_i\sqrt{1-t_i^2}\,\mathrm{e}^{i(2\gamma_s+\gamma_i)}, \qquad \tilde{d} = -p\,t_i^2\sqrt{1-t_s^2}\,\mathrm{e}^{i2\gamma_i},$$
$$\tilde{e} = p\,\sqrt{1-t_s^2}\sqrt{1-t_i^2}, \qquad \tilde{f} = p\,t_i\sqrt{1-t_s^2}\sqrt{1-t_i^2}\,\mathrm{e}^{i\gamma_i},$$
$$\tilde{g} = -p\,t_s t_i^2\sqrt{1-t_s^2}\,\mathrm{e}^{i2(\gamma_s+\gamma_i)}, \qquad \tilde{h} = -p\,t_s\sqrt{1-t_s^2}\sqrt{1-t_i^2}\,\mathrm{e}^{i2\gamma_s},$$
$$\text{and} \quad \tilde{j} = -p\,t_s t_i\sqrt{1-t_s^2}\sqrt{1-t_i^2}\,\mathrm{e}^{i(2\gamma_s+\gamma_i)}.$$

The reduced density matrix is found tracing out the idler states

$$\begin{aligned}\hat{\rho}_s &= \langle 000|_i\,|\psi\rangle\,\langle\psi|000\rangle_i + \langle 100|_i\,|\psi\rangle\,\langle\psi|100\rangle_i + \langle 010|_i\,|\psi\rangle\,\langle\psi|010\rangle_i + \langle 001|_i\,|\psi\rangle\,\langle\psi|001\rangle_i \\ &= \frac{1}{2}\Big[\,|000\rangle_s\,\langle 000|_s + \left(|\tilde{a}|^2 + \left|\tilde{b}\right|^2 + |\tilde{c}|^2\right)|100\rangle_s\,\langle 100|_s + \left(\left|\tilde{d}\right|^2 + |\tilde{e}|^2 + \left|\tilde{f}\right|^2\right)|010\rangle_s\,\langle 010|_s + \\ &\quad + \left(|\tilde{g}|^2 + \left|\tilde{h}\right|^2 + \left|\tilde{j}\right|^2\right)|001\rangle_s\,\langle 001|_s + \left(\tilde{a}\tilde{d}^* + \tilde{b}\tilde{e}^* + \tilde{c}\tilde{f}^*\right)|100\rangle_s\,\langle 010|_s + \\ &\quad + \left(\tilde{a}\tilde{g}^* + \tilde{b}\tilde{h}^* + \tilde{c}\tilde{j}^*\right)|100\rangle_s\,\langle 001|_s + \left(\tilde{d}\tilde{g}^* + \tilde{e}\tilde{h}^* + \tilde{f}\tilde{j}^*\right)|010\rangle_s\,\langle 001|_s + \\ &\quad + h.c.\Big]\end{aligned} \tag{A.24}$$

And the probability for the signal to be in mode s_2 is

$$p_s = |\tilde{a}|^2 + \left|\tilde{b}\right|^2 + |\tilde{c}|^2 = p^2\left[t_p^4 + t_s^4 + 2t_s^2 t_i^2 t_p^2\cos(2\Delta\gamma)\right]. \tag{A.25}$$

It follows that the visibility of the interference pattern is

$$v = t_i^2\frac{2t_s^2 t_p^2}{t_s^4 + t_p^4}. \tag{A.26}$$

A.2. Imaging with undetected photons

In this section, I present the calculation for imaging with undetected photons in the case in which imaging is enabled by position correlation and momentum anti-correlation. In both cases, the imaging system is described by the unitary transformation

$$\hat{\mathcal{U}} = \hat{\mathbb{1}} + \hat{\mathcal{H}}_{eff\,1} + \hat{\mathcal{H}}_{eff\,2}, \tag{A.27}$$

where

$$\hat{\mathcal{H}}_{eff\,1} = \int d\boldsymbol{q}_{s_1}\,d\boldsymbol{q}_{i_1}\,C(\boldsymbol{q}_{s_1},\boldsymbol{q}_{i_1})\,\hat{a}^\dagger_{s_1}(\boldsymbol{q}_{s_1})\hat{a}^\dagger_{i_1}(\boldsymbol{q}_{i_1}) + h.c. \tag{A.28}$$

and

$$\hat{\mathcal{H}}_{eff\,2} = \mathrm{e}^{i\gamma_p}\int d\boldsymbol{q}_{s_2}\,d\boldsymbol{q}_{i_2}\,C(\boldsymbol{q}_{s_2},\boldsymbol{q}_{i_2})\,\hat{a}^\dagger_{s_2}(\boldsymbol{q}_{s_2})\hat{a}^\dagger_{i_2}(\boldsymbol{q}_{i_2}) + h.c. \tag{A.29}$$

The Hamiltonians (A.28) and (A.29) describe the generation of photon pairs in source j ($j = 1, 2$) with transverse momenta components $\boldsymbol{q}_{s_j}$ and $\boldsymbol{q}_{i_j}$, with joint probability amplitude $C(\boldsymbol{q}_{s_j},\boldsymbol{q}_{i_j})$.

A.2.1. Position correlation

I consider a cascaded configuration in which imaging is enabled by position correlation, as illustrated in Fig. A.4. Fig. A.4 is the same as Fig. 3.3. However, the caption contextualizes the imaging system in the specific framework of imaging enabled by position correlation.

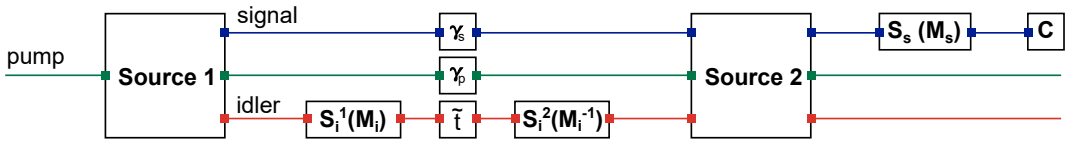

Figure A.4.: Same as Fig. 3.3. Cascaded configuration for a setup of imaging with undetected photons. Two sources are coherently pumped. The idler photon is magnified with magnification M_i, such that it interacts with a target of complex space-dependent transmittance $\tilde{t}(M_i\boldsymbol{x}_i)$, where $\boldsymbol{x}_i$ is the idler transversal coordinate at the source. Signal photons are subjected to magnification M_s after the second source and are measured at the camera (C) position $\boldsymbol{x}_c = M_s\boldsymbol{x}_s$, where $\boldsymbol{x}_s$ is the signal transversal coordinate at the source.

Due to the **spatial** superposition between the idler modes and the interaction with the target, the construction operator for the idler mode in source 1 is

$$\hat{a}^\dagger_{i_1}(\boldsymbol{x}_i) = \tilde{t}(M_i\boldsymbol{x}_i)\hat{a}^\dagger_{i_2}(\boldsymbol{x}_i) + \tilde{r}(M_i\boldsymbol{x}_i)\hat{a}^\dagger_{i_3}(\boldsymbol{x}_i), \tag{A.30}$$

where $\tilde{t}(M_i\boldsymbol{x_i}) = t(M_i\boldsymbol{x}_i)\exp(i\gamma_t(M_i\boldsymbol{x}_i))$ is the complex transmittance of the target at the transverse spatial coordinate $\boldsymbol{x}_t = M_i\boldsymbol{x_i}$, with $\boldsymbol{x}_i$ is the transverse spatial coordinate of the idler at the source, and M_i the magnification. $\tilde{r}$ represents the probability amplitude for a photon to be lost in the mode labeled with i_3, and satisfies the condition $\left|\tilde{t}(\boldsymbol{x_t})\right|^2 + \left|\tilde{r}(\boldsymbol{x_t})\right|^2 = 1$. The transmittance $\tilde{t}(M_i\boldsymbol{x}_i)$, the reflectance $\tilde{r}(M_i\boldsymbol{x}_i)$, and the creation operators $\hat{a}^\dagger_{i_2}(\boldsymbol{x}_i)$ and $\hat{a}^\dagger_{i_3}(\boldsymbol{x}_i)$ can be written as the inverse Fourier transform ($\mathscr{F}^{-1}$) of their counterparts in the transverse momenta component space. In the following, I will make explicit the dependence on the spatial coordinate or the momenta coordinate, and I will not use a different symbol to indicate a quantity in either space. Applying the convolution theorem and taking into account the linearity of the transformation,

$$\begin{aligned}\hat{a}^\dagger_{i_1}(\boldsymbol{x}_i) &= \mathscr{F}^{-1}\left[\frac{1}{M_i}\tilde{t}\left(\frac{\boldsymbol{q}_i}{M_i}\right)\right]\mathscr{F}^{-1}\left[\hat{a}^\dagger_{i_2}(\boldsymbol{q}_i)\right] + \mathscr{F}^{-1}\left[\frac{1}{M_i}\tilde{r}\left(\frac{\boldsymbol{q}_i}{M_i}\right)\right]\mathscr{F}^{-1}\left[\hat{a}^\dagger_{i_3}(\boldsymbol{q}_i)\right] \\ &= \mathscr{F}^{-1}\left[\frac{1}{M_i}\tilde{t}\left(\frac{\boldsymbol{q}_i}{M_i}\right) * \hat{a}^\dagger_{i_2}(\boldsymbol{q}_i) + \frac{1}{M_i}\tilde{r}\left(\frac{\boldsymbol{q}_i}{M_i}\right) * \hat{a}^\dagger_{i_3}(\boldsymbol{q}_i)\right].\end{aligned} \tag{A.31}$$

By applying a Fourier transform both to the left-hand-side term and the right-hand-side term, and making explicit the convolution operation $*$, it follows that

$$\hat{a}^\dagger_{i_1}(\boldsymbol{q}_i) = \int d\boldsymbol{q}\,\frac{1}{M_i}\left[\tilde{t}\left(\frac{\boldsymbol{q}_i - \boldsymbol{q}}{M_i}\right)\hat{a}^\dagger_{i_2}(\boldsymbol{q}_i) + \tilde{r}\left(\frac{\boldsymbol{q}_i - \boldsymbol{q}}{M_i}\right)\hat{a}^\dagger_{i_3}(\boldsymbol{q}_i)\right]. \tag{A.32}$$

Similarly, one has to consider the phase shift of the signal modes generated in source 1 and their superposition with the signal modes generated in source 2:

$$\hat{a}^\dagger_{s_1}(\boldsymbol{x}_s) = \hat{a}^\dagger_{s_2}(\boldsymbol{x}_s)\,\mathrm{e}^{i\gamma_s}. \tag{A.33}$$

Since γ_s is time independent,

$$\hat{a}^\dagger_{s_1}(\boldsymbol{q}_s) = \hat{a}^\dagger_{s_2}(\boldsymbol{q}_s)\,\mathrm{e}^{i\gamma_s}. \tag{A.34}$$

By substituting Eqs. (A.32) and (A.34) in Eqs. (A.27), (A.28), and (A.29), and applying the resulting unitary transformation to the vacuum state $|\text{vac}\rangle$, the final state is

$$\begin{aligned}|\psi\rangle &= \hat{\mathcal{U}}\,|\text{vac}\rangle \\ &= |\text{vac}\rangle + \int d\boldsymbol{q}d\boldsymbol{q}_s d\boldsymbol{q}_i\, \mathrm{e}^{i\gamma_s} C(\boldsymbol{q}_s,\boldsymbol{q}_i)\Bigg\{ \left[\frac{1}{M_i}\tilde{t}\left(\frac{\boldsymbol{q}_i-\boldsymbol{q}}{M_i}\right) + \mathrm{e}^{i(\gamma_p-\gamma_s)}\right] |\boldsymbol{q}_s\rangle\,|\boldsymbol{q}_i,0\rangle + \\ &\qquad + \frac{1}{M_i}\tilde{r}\left(\frac{\boldsymbol{q}_i-\boldsymbol{q}}{M_i}\right)|\boldsymbol{q}_s\rangle\,|0,\boldsymbol{q}_i\rangle\Bigg\},\end{aligned} \tag{A.35}$$

where $|\boldsymbol{q}_s\rangle$ represents the signal state generated with transverse momentum $\boldsymbol{q}_s$. If the idler state generated with transverse momentum $\boldsymbol{q}_i$ is in the mode i_2, it is represented with $|\boldsymbol{q}_i,0\rangle$, otherwise if the idler is lost in mode i_3, it is written as $|0,\boldsymbol{q}_i\rangle$.

The creation operator for a signal photon at transversal coordinate $\boldsymbol{x}_c = M_s\boldsymbol{x}_s$ on the camera is

$$\hat{a}_s^\dagger(\boldsymbol{x}_c) = \int d\boldsymbol{q_s}\,\hat{a}_{s_2}^\dagger(\boldsymbol{q}_s)\mathrm{e}^{i\boldsymbol{q}_s\boldsymbol{x}_c/M_s}. \tag{A.36}$$

The probability $p_s(\boldsymbol{x}_c)$ of measuring a photon at the camera is proportional to the photon number at the camera

$$\begin{aligned}p(\boldsymbol{x}_c) &\propto \langle\psi|\,\hat{a}_s^\dagger(\boldsymbol{x}_c)a_s(\boldsymbol{x}_c)\,|\psi\rangle \\ &\propto \int d\boldsymbol{x}_t \left|\check{C}\left(\frac{\boldsymbol{x}_c}{M_s},\frac{\boldsymbol{x}_t}{M_i}\right)\right|^2 \Big(1+t(\boldsymbol{x}_t)\cos[\gamma_p-\gamma_s-\gamma_t(\boldsymbol{x}_t)]\Big).\end{aligned} \tag{A.37}$$

A.2.2. Momentum anti-correlation

In the case in which imaging is enabled by position correlation, the construction operators $\hat{a}_{i_1}^\dagger$ and $\hat{a}_{s_1}^\dagger$ can be written as

$$\begin{aligned}\hat{a}_{i_1}^\dagger(\boldsymbol{q}_i) &= \tilde{t}(\boldsymbol{q}_i)\hat{a}_{i_2}^\dagger(\boldsymbol{q}_i) + \tilde{r}(\boldsymbol{q}_i)\hat{a}_{i_3}^\dagger(\boldsymbol{q}_i) \\ \hat{a}_{s_1}^\dagger(\boldsymbol{q}_s) &= \hat{a}_{s_2}^\dagger(\boldsymbol{q}_s)\mathrm{e}^{i\gamma_s}.\end{aligned} \tag{A.38}$$

By substitution in Eqs. (A.27), (A.28), and (A.29), the unitary transformation is

$$\hat{\mathcal{U}} = \hat{\mathbb{1}} + \int d\boldsymbol{q}_s d\boldsymbol{q}_i\, C(\boldsymbol{q}_s,\boldsymbol{q}_i)\mathrm{e}^{i\gamma_s}\Big\{\Big[\tilde{t}(\boldsymbol{q}_s)+\mathrm{e}^{i(\gamma_p-\gamma_s)}\Big]\hat{a}_{s_2}^\dagger(\boldsymbol{q}_s)\hat{a}_{i_2}^\dagger(\boldsymbol{q}_i) + \tilde{r}(\boldsymbol{q}_s)\hat{a}_{s_2}^\dagger(\boldsymbol{q}_s)\hat{a}_{i_3}^\dagger(\boldsymbol{q}_i)\Big\} + h.c. \tag{A.39}$$

The final state

$$\begin{aligned}|\psi\rangle &= \hat{\mathcal{U}}\,|\text{vac}\rangle \\ &= |\text{vac}\rangle + \int d\boldsymbol{q}_s d\boldsymbol{q}_i\, C(\boldsymbol{q}_s,\boldsymbol{q}_i)\mathrm{e}^{i\gamma_s}\Big\{\Big[\tilde{t}(\boldsymbol{q}_s)+\mathrm{e}^{i(\gamma_p-\gamma_s)}\Big]\,|\boldsymbol{q}_s\rangle\,|\boldsymbol{q}_i,0\rangle + \tilde{r}(\boldsymbol{q}_s)\,|\boldsymbol{q}_s\rangle\,|0,\boldsymbol{q}_i\rangle\Big\}.\end{aligned} \tag{A.40}$$

I calculate the reduced density matrix $\hat{\rho}_s$, by tracing out the idler state in the density matrix $|\psi\rangle\langle\psi|$:

$$\begin{aligned}\hat{\rho}_s &= |\text{vac}\rangle\langle\text{vac}| + \\ &\quad + \int d\boldsymbol{q}_s d\boldsymbol{q}_i d\boldsymbol{q}'_s\, C(\boldsymbol{q}_s,\boldsymbol{q}_i)C^*(\boldsymbol{q}_s,\boldsymbol{q}'_i)\left[\left|\tilde{t}(\boldsymbol{q}_i)+\mathrm{e}^{i(\gamma_p-\gamma_s)}\right|^2 + |\tilde{r}(\boldsymbol{q}_i)|^2\right]|\boldsymbol{q}_s\rangle\,\langle\boldsymbol{q}'_s|\,.\end{aligned} \tag{A.41}$$

The probability of measuring a photon in the state $\boldsymbol{q}_s''$ is

$$\begin{aligned} p(\boldsymbol{q}_s'') &= \langle \boldsymbol{q}_s'' | \, \hat{\rho}_s \, | \boldsymbol{q}_s'' \rangle \\ &\propto \int d\boldsymbol{q}_i |C(\boldsymbol{q}_s'', \boldsymbol{q}_i)|^2 \left[1 + t(\boldsymbol{q_i}) \cos\left(\gamma_p - \gamma_s - \gamma_t(\boldsymbol{q}_i)\right)\right]. \end{aligned} \tag{A.42}$$

For simplicity, I rename $\boldsymbol{q}_s''$ as $\boldsymbol{q}_s$. I assume that the optical system S_s univocally associates a transverse momenta component $\boldsymbol{q}_s$ to a transverse coordinate on the camera plane, i.e., there is a map that associates $\boldsymbol{q}_s \xrightarrow{S_s} \boldsymbol{x}_c = \boldsymbol{x}_{\boldsymbol{q}_s}$. In the same way, the system S_i associates the momentum component $\boldsymbol{q}_i$ to a position on the target: $\boldsymbol{q}_i \xrightarrow{S_i} \boldsymbol{x}_t = \boldsymbol{x}_{\boldsymbol{q}_i}$.

Therefore, the probability of measuring a photon at the camera coordinate $\boldsymbol{x}_{\boldsymbol{q}_s}$ is

$$p(\boldsymbol{x}_{\boldsymbol{q}_s}) \propto \int d\boldsymbol{q}_i |C(\boldsymbol{q}_s, \boldsymbol{q}_i)|^2 \left[1 + t(\boldsymbol{x}_{\boldsymbol{q_i}}) \cos\left(\gamma_p - \gamma_s - \gamma_t(\boldsymbol{x}_{\boldsymbol{q}_i})\right)\right]. \tag{A.43}$$

A.3. Longitudinal phase mismatch

In Eq. (3.4), I wrote the longitudinal phase mismatch Δk_z as a function of the photon transverse components $\boldsymbol{q}$ and wavelength λ. In the following, the derivation is made explicit.

$$\Delta k_z = \sqrt{k_p^2 - \left|\boldsymbol{q}_p\right|^2} - \sqrt{k_s^2 - \left|\boldsymbol{q}_s\right|^2} - \sqrt{k_i^2 - \left|\boldsymbol{q}_i\right|^2}, \tag{A.44}$$

where $k = |\boldsymbol{k}| = \frac{2\pi}{\lambda} n(\lambda)$, where n is the refractive index.

$$\begin{aligned} \Delta k_z &= k_p \sqrt{1 - \frac{\left|\boldsymbol{q}_p\right|^2}{k_p^2}} - k_s \sqrt{1 - \frac{\left|\boldsymbol{q}_s\right|^2}{k_s^2}} - k_i \sqrt{1 - \frac{\left|\boldsymbol{q}_i\right|^2}{k_i^2}} \\ &\simeq k_p - \frac{1}{2} \frac{\left|\boldsymbol{q}_p\right|^2}{k_p} - \left(k_s - \frac{1}{2} \frac{\left|\boldsymbol{q}_s\right|^2}{k_s}\right) - \left(k_i - \frac{1}{2} \frac{\left|\boldsymbol{q}_i\right|^2}{k_i}\right) \end{aligned} \tag{A.45}$$

Where I assumed the case of collinear generation, in the paraxial approximation where the relation $|q|^2/k^2 \ll 1$ holds. In the paraxial approximation, the phase matching condition can be written as $k_p - k_s - k_i \simeq 0$. The condition of transverse momentum conservation allows writing the pump transverse momentum component as a function of the signal and idler components: $\boldsymbol{q}_p = \boldsymbol{q}_s - \boldsymbol{q}_i$.

$$\begin{aligned} \Delta k_z &\simeq -\left[|\boldsymbol{q}_s|^2 \left(\frac{1}{2k_p} - \frac{1}{2k_s}\right) + |\boldsymbol{q}_i|^2 \left(\frac{1}{2k_p} - \frac{1}{2k_i}\right) + \frac{\boldsymbol{q}_s \cdot \boldsymbol{q}_i}{k_p}\right] \\ &\simeq \frac{k_i}{2k_s k_p} \left|\boldsymbol{q}_s - \frac{k_s}{k_i} \boldsymbol{q}_i\right|^2 \\ &\simeq \frac{\lambda_p \lambda_s}{2\pi \lambda_i} \frac{n_i}{n_s n_p} \left|\boldsymbol{q}_s - \frac{n_s \lambda_i}{n_i \lambda_s} \boldsymbol{q}_i\right|^2 \end{aligned} \tag{A.46}$$

In the specific case of not strongly degenerate generation $n_s/n_i \simeq 1$. This in the case of interest of this thesis, where $n_s/n_i \simeq 0.984$. Additionally, I approximate $n_p = 1.89 \simeq 2$.

It results

$$\Delta k_z \simeq \frac{\lambda_p \lambda_s}{4\pi \lambda_i} \left|\boldsymbol{q}_s - \frac{\lambda_i}{\lambda_s} \boldsymbol{q}_i\right|^2. \tag{A.47}$$

B. Simulations

In this Appendix, I share the Matlab codes I wrote for the simulations presented in this thesis. The original files are available upon request at chiara.michelini [at] unitn.it.

B.1. Joint spectral intensity for SPDC with ppKTP

The simulation of the joint spectral intensity for a type-0 collinear SPDC process in ppKTP follows. This simulation takes into account the temperature dependence of both the refractive index and the poling period of the crystal.

```
%% JSI for ppKTP 532 nm -> 810 nm + 1550 nm
% ***** Constants *****
c = physconst('LightSpeed'); % [m/s]
% ***** Parameters *****
% Crystal temperature [\degC]; Poling period at room temperature [m]; Crystal length [m]
T = 73; pp0 = 9.675e-6; L = 2e-2;
% Pump central wavelength and bandwidth [m]
lambda_p0 = 532e-9; delta_lambda_p0 = 0.005*1e-9;
% Signal and idler wavelength ranges [m]
lambda_lim_s = [805, 816]*1e-9; lambda_lim_i = [1500, 1590]*1e-9; %m
% ***** Sellmeier Equations *****
Lambda=(.3:.0001:1.8)*1e-6; % [m] % Wavelengths
Omega = 2*pi*c./Lambda; % Frequencies
l = Lambda*1e6; % [um]
% ***** Coefficients *****
% Reference doi:10.1063/1.1519097
Az = 1.71645; Bz = 0.01346; Cz = 0.5924; Dz = 0.06503;
Ez = 0.3226; Fz = 67.1208; Gz = 0.01133;
% Terms in Sellmeier equations
t1 = (Az*l.^2)./(l.^2 - Bz);
t2 = (Cz*l.^2)./(l.^2 - Dz);
t3 = (Ez*l.^2)./(l.^2 - Fz);
t4 = Gz*l.^2;
% Temperature dependence - refractive index
% Reference doi:10.1364/ao.42.006661
T0 = 25; % [\degC]
a1 = [9.9587, 9.9228, -8.9603, 4.1010]*1e-6;
n1 = a1(1) + a1(2)./l + a1(3)./(l.^2) + a1(4)./(l.^3);
a2 = [-1.1882 10.459 -9.8136 3.1481]*1e-8;
n2 = a2(1) + a2(2)./l + a2(3)./(l.^2) + a2(4)./(l.^3);
delta_n = n1*(T-T0)+n2*(T-T0)^2;
% Refractive index
nz = sqrt(1 + t1 + t2 + t3 - t4) + delta_n;
% Omega is dense enough for a linear interpolation
fit1 = fit(Omega'*1e-15, nz', 'linearinterp');
nz_fit = @(x) fit1(x*1e-15);
% Temperature dependence - poling period
% Reference doi:10.1364/ao.42.006661
% % Negligible contribution with respect to
% % refractive index temperature dependence
alpha = 6.75e-6; % [1/\degC]
beta  = 11e-9; % [1/\degC^2]
pp = pp0*(1 + alpha*(T-T0) + beta*(T-T0)^2);
% ***** Pump envelope function (PEF) *****
% Angular frequencies
w_p0 = c*2*pi/lambda_p0;
```

```
dw_p0 = c*2*pi*delta_lambda_p0/lambda_p0^2;
w_s_lim = c*2*pi./lambda_lim_s;
w_i_lim = c*2*pi./lambda_lim_i;
w_s = linspace(min(w_s_lim), max(w_s_lim), 750); % row vector
w_i = linspace(min(w_i_lim), max(w_i_lim), 751)';% column vector
% Energy conservation
W_p = w_i + w_s; % 2D matrix
% PEF
PEF = sqrt(exp(-(W_p-w_p0).^2/(2*dw_p0)^2));
% ***** Phase matching function (PMF)*****
sz = size(W_p);
w_p_arr = reshape(W_p, [1,sz(1)*sz(2)]); % 1D array
% Momenta
k_s = w_s.*nz_fit(w_s)'/c; % row vector
k_i = w_i.*nz_fit(w_i)/c; % column vector
k_p_arr = w_p_arr.*nz_fit(w_p_arr)'/c;
K_p = reshape(k_p_arr, sz); % 2D matrix
% Additional momentum contribution
K = 2*pi/pp;
% Phase mismatch
delta_k = K_p - k_i - k_s;
% Phase matching function
phi = (delta_k - K)*L/2;
PMF = L*(sin(phi))./(phi);
% ***** Joint spectral amplitude (JSA) ******
JSA_not_norm = PEF.*PMF;
normalization_constant = trapz(w_i, (trapz(w_s, abs(JSA_not_norm).^2, 2)));
JSA = JSA_not_norm/sqrt(normalization_constant);
% ***** Joint spectral intensity (JSI) ******
JSI = abs(JSA).^2;
% Plot
lambda_s = c*2*pi./w_s; lambda_i = c*2*pi./w_i;
[X,Y] = meshgrid(lambda_s, lambda_i);
figure
surf(X*1e9,Y*1e9, JSI);
view(2); shading flat; colorbar
xlim(lambda_lim_s*1e9); ylim(lambda_lim_i*1e9)
xlabel('Signal wavelength [nm]'); ylabel('Idler wavelength [nm]')
title('Joint spectral intensity')
set(gca, 'Fontsize', 14)
```

B.2. Momenta distribution for SPDC with ppKTP

Detailed below is the code for the simulation of the transverse momenta distribution for a type-0 SPDC in a ppKTP crystal. This simulation is based on the work of Lerch et al. [50].

B.2.1. Main

```
% ***** Constants *****
c = physconst('LightSpeed'); % [m/s]
% ***** Parameters *****
% Crystal temperature [C]; Poling period at room temperature [m]; Crystal length [m]; Pump
% waist [m]
T = 73; pp0 = 9.675e-6; L = 2e-2; w0 = 20e-6;
% Pump central wavelength[m]
lambda_p0 = 532e-9;
    omega_p0 = 2*pi*c./lambda_p0; % pump frequency [Hz]
    % % Signal frequency vector centered at pump frequency/2
    omega_s = (0.5:1/100:1.5)*omega_p0/2;
    lambda_s = 2*pi*c./omega_s;
% ***** Sellmeier Equations *****
Lambda=(.3:.0001:1.8)*1e-6; % [m] % Wavelengths
Omega = 2*pi*c./Lambda; % Frequencies
l = Lambda*1e6; % [um]
```

```
% ***** Coefficients *****
% Reference doi:10.1063/1.1519097
Az = 1.71645; Bz = 0.01346; Cz = 0.5924; Dz = 0.06503;
Ez = 0.3226; Fz = 67.1208; Gz = 0.01133;
% Terms in Sellmeier equations
t1 = (Az*l.^2)./(l.^2 - Bz);
t2 = (Cz*l.^2)./(l.^2 - Dz);
t3 = (Ez*l.^2)./(l.^2 - Fz);
t4 = Gz*l.^2;
% Temperature dependence - refractive index
% Reference doi:10.1364/ao.42.006661
T0 = 25; % [\degC]
a1 = [9.9587, 9.9228, -8.9603, 4.1010]*1e-6;
n1 = a1(1) + a1(2)./l + a1(3)./(l.^2) + a1(4)./(l.^3);
a2 = [-1.1882 10.459 -9.8136 3.1481]*1e-8;
n2 = a2(1) + a2(2)./l + a2(3)./(l.^2) + a2(4)./(l.^3);
delta_n = n1*(T-T0)+n2*(T-T0)^2;
% Refractive index
nz = sqrt(1 + t1 + t2 + t3 - t4) + delta_n;
% Omega is dense enough for a linear interpolation
fit1 = fit(Omega'*1e-15, nz', 'linearinterp');
nz_fit = @(x) fit1(x*1e-15);
% Temperature dependence - poling period
% Reference doi:10.1364/ao.42.006661
% % Negligible contribution with respect to
% % refractive index temperature dependence
alpha = 6.75e-6; % [1/\degC]
beta  = 11e-9; % [1/\degC^2]
pp = pp0*(1 + alpha*(T-T0) + beta*(T-T0)^2);
% % Signal and idler transverse momenta [1/m]
% [Decrease spacing in q_s for better resolution]
qs_x = (-1:.05:1)*1e6; % column vector
qs_y = (-1:.05:1)'*1e6; % row vector
qi_x = (-1:.05:1)*1e6; % column vector
qi_y = (-1:.05:1)'*1e6; % row vector
%% S(qx, qy, omega)
%  S(qs_x, qs_y, lambda_s) is a 3D matrix
S=zeros(length(qs_y), length(qs_x), length(lambda_s)); % Preallocation
sz = size(S);
for i=1:length(qs_y) % for each qs_y
    for j=1:length(qs_x) % for each qs_x
        for k=1:length(lambda_s) % for each lambda_s
            % Calculate the matrix element S(qs_x, qs_y, lambda_s)
            S(i,j,k) = SPDC_spatial(qs_x(j), qs_y(i), qi_x, qi_y, lambda_p0, lambda_s(k), w0, L, pp,
                nz_fit);
        end
    end
    clc
    fprintf('Progress: %.1f%%\n', i*j*k*100/(sz(1)*sz(2)*sz(3)))
end
S=S/max(max(max(S))); % normalize S to maximum
[idx, ~] = find(S==1); % find maximum location to slice S in 2D space
s(:,:)=S(idx(1),:,:); % = S(qs_x, qs_y=0, omega_s)
%% Figure
figure
[X,Y] = meshgrid(2*omega_s/omega_p0, qs_x*1e-6);
surf(X, Y, s)
colorbar
colormap hot
shading flat
view(2)
% xlim([0.6 1.4])
xlabel('\omega_s [\omega_p/2]')
ylabel('q_x_s [1/\mum]')
title('Probability density S(q_x_s, 0, \omega_s)')
set(gca, 'fontsize', 14, 'XTick', [.8 1 1.2])
xlim([min(2*omega_s/omega_p0), max(2*omega_s/omega_p0)])
```

B.2.2. Nested function

```
function S = SPDC_spatial(qs_x, qs_y, qi_x, qi_y, lambda_p, lambda_s, w0, L, pp, nz_fit)
% S = SPDC_spatial(qs_x, qs_y, qi_x, qi_y, lambda_p, lambda_s, w0, L, pp, nz_fit)
%   Returns S(qs_x, qs_y, lambda_s)
%   S, qs_x, qs_y , lambda_s, lambda_p, w0, L, and pp are numbers
%   qi_x is a row vector, qi_y is a column vector
%   nz_fit is a fit function
%   Unit measurement in SI
c=physconst('LightSpeed');
omega_p = 2*pi*c/lambda_p; omega_s = 2*pi*c/lambda_s;
q_i_square=qi_x.^2+qi_y.^2; % 2D matrix
k_i= (omega_p-omega_s)*nz_fit(omega_p-omega_s)/c; % number
delta_ki_z= sqrt(k_i^2-q_i_square); % 2D matrix
q_s_square=qs_x^2+qs_y^2; % number
k_s= (omega_s)*nz_fit(omega_s)/c; % number
delta_ks_z= sqrt(k_s^2-q_s_square); % number
qx = (qi_x+qs_x); % row vector
qy = (qi_y+qs_y); % column vector
q_p_square = qx.^2+qy.^2; % 2D matrix
k_p = omega_p*nz_fit(omega_p)/c; % number
delta_kp_z= sqrt(k_p^2-q_p_square); % 2D matrix
delta_k_z = delta_ki_z + delta_ks_z - delta_kp_z; % 2D matrix
joint_amplitude = exp(-(w0^2*(q_p_square))/4).*(L*sin((delta_k_z+2*pi/pp)*L/2)).*(1./((delta_k_z+2*pi/pp)
    *L/2));
joint_density = abs(joint_amplitude).^2;
S = trapz(qi_y, trapz(qi_x, joint_density, 2));
end
```

B.3. Imaging in far field

The following code allows simulating the two-dimensional image obtained with a system for imaging with undetected photons in a far field configuration, in which the pump is focused with pump waist `w_p` at the crystal center. Both the probing and the detected photons are assumed to be monochromatic, at wavelengths `lambda_i` and `lambda_s`, respectively. The simulated object is a resolution test target with three stripes separated by a distance of `x_separation`.

```
%% Imaging in far field of a resolution USAF-like target
%********** parameters **********
w_p = 342e-6; % pump waist [m]
% pump, signal and idler wavelengths (m)
lambda_p = 532e-9; lambda_s = 810e-9; lambda_i = 1550e-9;
% magnification of the signal on the camera, and of the idler on the target
M_s = 1; M_i = 1;
% propagation distances of the signal from the crystal to the camera, and
% propagation distance of the idler from the crystal to the target [m]
d_s = 250e-3; d_i = 200e-3;
% target properties: separation between the lines in an USAF-like target [m]
x_separation = .25e-3;
% maximum transversal momentum components of the signal and the idler [m]
% it is not relevant to the resolution, but could be useful to determine
% weather the target/camera is entirely illuminated
q_s_max = 5e4; q_i_max = 5e4;
%*****************************
% descrete array of momenta component:
step_q = min(q_i_max, q_s_max)/100;
qx_s = [flip(-step_q:-step_q:-q_s_max), 0:step_q:q_s_max]; qy_s = qx_s;
qx_i = [flip(-step_q:-step_q:-q_i_max), 0:step_q:q_i_max]; qy_i = qx_i;
% q2r is a map that associate q to a spatial coordinate in the far field
function r = q2r(q, M, d, lambda)
r = M*d*lambda*q/2/pi;
end
x_s = q2r(qx_s, M_s, d_s, lambda_s); y_s = q2r(qy_s, M_s, d_s, lambda_s);
x_i = q2r(qx_i, M_i, d_i, lambda_i); y_i = q2r(qy_i, M_i, d_i, lambda_i);
```

```
%*** construction of the USAF-like target (three vertical stripes)
step_x_i = abs(x_i(3)-x_i(2)); step_y_i = abs(y_i(3)-y_i(2));
usaf_dim_x = 2e-2; usaf_dim_y = 2e-2; %m
if x_i(3)-x_i(2) > 0
    x_usaf = [flip(-step_x_i:-step_x_i:-(usaf_dim_x/2)), 0:step_x_i:usaf_dim_x/2];
    y_usaf = [flip(-step_y_i:-step_y_i:-(usaf_dim_y/2)), 0:step_y_i:usaf_dim_x/2];
elseif x_i(3)-x_i(2) < 0
    x_usaf = flip([flip(-step_x_i:-step_x_i:-(usaf_dim_x/2)), 0:step_x_i:usaf_dim_x/2]);
    y_usaf = flip([flip(-step_y_i:-step_y_i:-(usaf_dim_y/2)), 0:step_y_i:usaf_dim_y/2]);
else
    warning('Someting is wrong in the definition of x_usaf and y_usaf. Try increasing usaf_dim_x/y')
end
y_start = -5*x_separation/2; y_end = 5*x_separation/2;
x_A_start = -5*x_separation/2; x_A_end = -3*x_separation/2; % first stripe
x_B_start = -x_separation/2; x_B_end = x_separation/2; % second stripe
x_C_start = 3*x_separation/2; x_C_end = 5*x_separation/2; % third stripe
idx_y_start = find(abs(y_usaf-(y_start))<step_y_i/2);
idx_y_end = find(abs(y_usaf-(y_end))<step_y_i/2);
idx_x_A_start = find(abs(x_usaf-(x_A_start))<step_x_i/2); idx_x_A_end = find(abs(x_usaf-(x_A_end))<
    step_x_i/2);
idx_x_B_start = find(abs(x_usaf-(x_B_start))<step_x_i/2); idx_x_B_end = find(abs(x_usaf-(x_B_end))<
    step_x_i/2);
idx_x_C_start = find(abs(x_usaf-(x_C_start))<step_x_i/2); idx_x_C_end = find(abs(x_usaf-(x_C_end))<
    step_x_i/2);
mask = zeros(size(meshgrid(x_usaf, y_usaf)));
mask(min(idx_y_start, idx_y_end):max(idx_y_start, idx_y_end), min(idx_x_A_start,idx_x_A_end):max(
    idx_x_A_start,idx_x_A_end)) = 1;
mask(min(idx_y_start, idx_y_end):max(idx_y_start, idx_y_end), min(idx_x_B_start,idx_x_B_end):max(
    idx_x_B_start,idx_x_B_end)) = 1;
mask(min(idx_y_start, idx_y_end):max(idx_y_start, idx_y_end), min(idx_x_C_start,idx_x_C_end):max(
    idx_x_C_start,idx_x_C_end)) = 1;
[X_usaf, Y_usaf] = meshgrid(x_usaf, y_usaf);
% Figure of the target
figure
surf(X_usaf*1e3, Y_usaf*1e3, mask); view(2)
shading flat; colormap gray; clim([0 1]); colorbar
xlabel('X position [mm]'); ylabel('Y position [mm]'); title('Target')
% ******** Object illuminated by the idler ********
idx_min = find(abs(x_usaf - min(x_i))<step_x_i*1e-4); idx_max = find(abs(x_usaf - max(x_i))<step_x_i*1e
    -4);
idy_min = find(abs(y_usaf - min(y_i))<step_y_i*1e-4); idy_max = find(abs(y_usaf - max(y_i))<step_y_i*1e
    -4);
t = mask(idy_min:idy_max, idx_min:idx_max);
[X_i, Y_i]=meshgrid(x_i, y_i);
% Figure of the target illuminated by the idler
figure
surf(X_i*1e3, Y_i*1e3, t); view(2)
shading flat; colormap gray; clim([0 1]); colorbar
xlabel('X position [mm]'); ylabel('Y position [mm]'); title('Target illuminated')
% ****** Imaging ******
function rho_momentum = momentum_correlation(w_p, qx_s, qy_s, qx_i, qy_i)
    rho_momentum = exp( -((qx_i + qx_s).^2 + (qy_i + qy_s)'.^2)*(w_p)^2/2);
end
v=zeros(size(meshgrid(x_s, y_s)));
for i = 1:length(qx_s)
    for j = 1:length(qy_s)
        p = momentum_correlation(w_p, qx_s(i), qy_s(j), qx_i, qy_i);
        arg = p .* t;
        norm_const_arg = p; norm_const = sum(sum(norm_const_arg)); % normalization
        v(j,i) = sum(sum(arg))/norm_const; % visibility
    end
end
[X_s, Y_s]=meshgrid(x_s, y_s);
% Figure of the visibility on camera
figure
surf(X_s*1e3, Y_s*1e3, v); view(2)
shading flat; colormap gray; clim([0 1]); colorbar
xlabel('X position [mm]'); ylabel('Y position [mm]'); title('Visibility on camera')
% ***** cut line to contrast analysys between the lines
imaging_line = v(floor(length(y_s)/2),:);
```

```
[~, loc_max] = findpeaks(imaging_line); [~, loc_min] = findpeaks(-imaging_line);
if isempty(loc_min)
    contrast_value = 0;
else
    contrast_value = (imaging_line(loc_max(1))-imaging_line(loc_min(1)))/(imaging_line(loc_max(1))+
        imaging_line(loc_min(1)));
end
figure
plot(x_s*1e3, imaging_line, 'linewidth', 1.5); ylim([0 1]);
xlabel('X position [mm]'); ylabel('Visibility on camera')
title('Contrast'), subtitle(['contrast = ', num2str(contrast_value)])
```

B.4. Visibility interference and distribution width

Simulation of the p parameter associated to the visibilities `v` (line 3), provided the average number of photons at the camera `N`, and the width of the signal distribution at zero visibility, `sigma_s`.

```
function p = psim(N,sigma_s)
phi = linspace(0, 2*pi*10, 1e5);
v = ([0.01:.001:.29, .3:.01:1]'); % visibility
perc = .1587; percs = [perc, 1-perc]; % percentiles for sigma_exp evaluation
interference_ideal = N*(1+v.*cos(phi));
sigma_exp = zeros(size(v));
bin_n = 50;
for i = 1:length(v)
    [y, binEdges] = histcounts(interference_ideal(i,:), bin_n);
    bidEdges_shift = circshift(binEdges,-1);
    x = (binEdges(1:end-1)+bidEdges_shift(1:end-1))/2;
    n = 100; step_x = x(2)-x(1);
    x_new = [x(1)-n*step_x:step_x:x(1)-step_x, x, ...
        x(end)+step_x:step_x:x(end)+n*step_x]; x = x_new;
    y_new = [zeros(size(x(1)-n*step_x:step_x:x(1)-step_x)), y, ...
        zeros(size(x(end)+step_x:step_x:x(end)+n*step_x))]; y = y_new;
    distribution = exp(-(x-mean(x)).^2/(sqrt(2)*sigma_s)^2);
    h = distribution/trapz(x,distribution);
    q = conv(y, h, 'same');
    cumulative_norm = cumsum(q)/max(cumsum(q)); c = cumulative_norm;
    a = 1; b = length(x); % initialization
    for j = 1:length(x)-1
        if abs(c(j)-c(j+1)) < 1e-3 && j<length(x)/2
            a = j;
        elseif abs(c(j)-c(j+1)) < 1e-3 && j >length(x)/2
            b = j;
            break
        end
    end
    c1=c(a:b);
    x1=x(a:b);
    f = fit(c1', x1', 'linearinterp');
    sigma_exp(i) = (f(percs(2))-f(percs(1)))/2;
end
p = 1- sigma_s./sigma_exp;
end
```

Bibliography

[1] Nabeel Aslam, Hengyun Zhou, Elana Urbach, Matthew Turner, Ronald Walsworth, Mikhail Lukin, and Hongkun Park. Quantum sensors for biomedical applications. *Nature Reviews Physics*, 5:1–13, 02 2023.

[2] Ludovic Thobois, Jean Cariou, and Ismail Gultepe. Review of lidar-based applications for aviation weather. *Pure and Applied Geophysics*, 176, 05 2019.

[3] Andrew Wallace, Jing Ye, Nils Krichel, Aongus McCarthy, Robert Collins, and Gerald Buller. Full waveform analysis for long-range 3d imaging laser radar. *EURASIP Journal on Advances in Signal Processing*, 2010:33, 01 2010.

[4] Jianan Fang, Kun Huang, E Wu, Ming Yan, and Heping Zeng. Mid-infrared single-photon 3d imaging. *Light Sci Appl*, 12(1), June 2023.

[5] A A Kalachev, D A Kalashnikov, A A Kalinkin, T G Mitrofanova, A V Shkalikov, and V V Samartsev. Biphoton spectroscopy of yag:er3+ crystal. *Laser Physics Letters*, 4(10):722, jun 2007.

[6] M. Mancinelli, A. Trenti, S. Piccione, G. Fontana, J. S. Dam, P. Tidemand-Lichtenberg, C. Pedersen, and L. Pavesi. Mid-infrared coincidence measurements on twin photons at room temperature. *Nature Communications*, 8(1), May 2017.

[7] T. B. Pittman, Y. H. Shih, D. V. Strekalov, and A. V. Sergienko. Optical imaging by means of two-photon quantum entanglement. *Phys. Rev. A*, 52:R3429–R3432, Nov 1995.

[8] Miles J. Padgett and Robert W. Boyd. An introduction to ghost imaging: quantum and classical. *Philosophical Transactions of the Royal Society A: Mathematical, Physical and Engineering Sciences*, 375(2099):20160233, June 2017.

[9] Matteo Sanna, Davide Rizzotti, Stefano Signorini, and Lorenzo Pavesi. 2 µm ghost spectroscopy with an integrated silicon quantum photonics source. *Advanced Quantum Technologies*, 7(1), October 2023.

[10] Gabriela Barreto Lemos, Mayukh Lahiri, Sven Ramelow, Radek Lapkiewicz, and William N. Plick. Quantum imaging and metrology with undetected photons: tutorial. *J. Opt. Soc. Am. B*, 39(8):2200–2228, Aug 2022.

[11] L. J. Wang, X. Y. Zou, and L. Mandel. Induced coherence without induced emission. *Physical Review A*, 44(7):4614–4622, October 1991.

[12] X. Y. Zou, L. J. Wang, and L. Mandel. Induced coherence and indistinguishability in optical interference. *Physical Review Letters*, 67(3):318–321, July 1991.

[13] Armin Hochrainer, Mayukh Lahiri, Manuel Erhard, Mario Krenn, and Anton Zeilinger. Quantum indistinguishability by path identity and with undetected photons. *Rev. Mod. Phys.*, 94:025007, Jun 2022.

[14] X. Y. Zou, T. Grayson, G. A. Barbosa, and L. Mandel. Control of visibility in the interference of signal photons by delays imposed on the idler photons. *Physical Review A*, 47(3):2293–2295, March 1993.

[15] Dmitry A. Kalashnikov, Anna V. Paterova, Sergei P. Kulik, and Leonid A. Krivitsky. Infrared spectroscopy with visible light. *Nature Photonics*, 10(2):98–101, January 2016.

[16] Jinghan Dong, Arthur C. Cardoso, Haichen Zhou, Jingrui Zhang, Weijie Nie, Alex S. Clark, and John G. Rarity. Methane sensing via unbalanced nonlinear interferometry using a CMOS camera and undetected mid-infrared light. *Applied Physics Letters*, 126(6):061104, 02 2025.

[17] Gabriela Barreto Lemos, Victoria Borish, Garrett D. Cole, Sven Ramelow, Radek Lapkiewicz, and Anton Zeilinger. Quantum imaging with undetected photons. *Nature*, 512(7515):409–412, August 2014.

[18] Inna Kviatkovsky, Helen M. Chrzanowski, and Sven Ramelow. Mid-infrared microscopy via position correlations of undetected photons. *Optics Express*, 30(4):5916, February 2022.

[19] Emma Pearce, Nathan R. Gemmell, Jefferson Flórez, Jiaye Ding, Rupert F. Oulton, Alex S. Clark, and Chris C. Phillips. Practical quantum imaging with undetected photons. *Opt. Continuum*, 2(11):2386–2397, Nov 2023.

[20] Aron Vanselow, Paul Kaufmann, Helen M. Chrzanowski, and Sven Ramelow. Ultrabroadband spdc for spectrally far separated photon pairs. *Opt. Lett.*, 44(19):4638–4641, Oct 2019.

[21] Fang Wang, Tao Zhang, Runzhang Xie, Anna Liu, Fuxing Dai, Yue Chen, Tengfei Xu, Hailu Wang, Zhen Wang, Lei Liao, Jianlu Wang, Peng Zhou, and Weida Hu. Next-generation photodetectors beyond van der waals junctions. *Advanced Materials*, 36(3), November 2023.

[22] I.E. Gordon, L.S. Rothman, C. Hill, R.V. Kochanov, Y. Tan, P.F. Bernath, M. Birk, V. Boudon, A. Campargue, K.V. Chance, B.J. Drouin, J.-M. Flaud, R.R. Gamache, J.T. Hodges, D. Jacquemart, V.I. Perevalov, A. Perrin, K.P. Shine, M.-A.H. Smith, J. Tennyson, G.C. Toon, H. Tran, V.G. Tyuterev, A. Barbe, A.G. Császár, V.M. Devi, T. Furtenbacher, J.J. Harrison, J.-M. Hartmann, A. Jolly, T.J. Johnson, T. Karman, I. Kleiner, A.A. Kyuberis, J. Loos, O.M. Lyulin, S.T. Massie, S.N. Mikhailenko, N. Moazzen-Ahmadi, H.S.P. Müller, O.V. Naumenko, A.V. Nikitin, O.L. Polyansky, M. Rey, M. Rotger, S.W. Sharpe, K. Sung, E. Starikova, S.A. Tashkun, J. Vander Auwera, G. Wagner, J. Wilzewski, P. Wcisło, S. Yu, and E.J. Zak. The HITRAN2016 molecular spectroscopic database. *Journal of Quantitative Spectroscopy and Radiative Transfer*, 203:3–69, December 2017.

[23] Daniel Popa and Florin Udrea. Towards integrated mid-infrared gas sensors. *Sensors*, 19(9):2076, May 2019.

[24] David Huang, Eric A. Swanson, Charles P. Lin, Joel S. Schuman, William G. Stinson, Warren Chang, Michael R. Hee, Thomas Flotte, Kenton Gregory, Carmen A. Puliafito, and James G. Fujimoto. Optical coherence tomography. *Science*, 254(5035):1178–1181, November 1991.

[25] Adam Vallés, Gerard Jiménez, Luis José Salazar-Serrano, and Juan P. Torres. Optical sectioning in induced coherence tomography with frequency-entangled photons. *Phys. Rev. A*, 97:023824, Feb 2018.

[26] Anna V Paterova, Hongzhi Yang, Chengwu An, Dmitry A Kalashnikov, and Leonid A Krivitsky. Tunable optical coherence tomography in the infrared range using visible photons. *Quantum Science and Technology*, 3(2):025008, April 2018.

[27] D. A. R. Dalvit, T. J. Volkoff, Y.-S. Choi, A. K. Azad, H.-T. Chen, and P. W. Milonni. Quantum frequency combs with path identity for quantum remote sensing. *Phys. Rev. X*,

14:041058, Dec 2024.

[28] **Chiara Michelini**, Stefano Signorini, Valerio Pruneri, and Lorenzo Pavesi. Undetected photon interference measurements on a silicon chip. In Keith S. Deacon and Ronald E. Meyers, editors, *Quantum Communications and Quantum Imaging XXI*, page 2. SPIE, October 2023.

[29] **Chiara Michelini**, Stefano Signorini, Lorenzo Pavesi, and Valerio Pruneri. Quantum undetected photon phase measurement on a silicon chip. *APL Photonics*, 10(10), October 2025.

[30] Carsten Pitsch, Alessia Suprano, Benjamin Guery, Francesco Poggiali, **Chiara Michelini**, Henri Haka, Davide Moschella, Dominik Walter, Ugo Zanforlin, Massimiliano Proietti, Massimiliano Dispenza, Alberto Tosi, and Federica Villa. Toward video-rate quantum ghost imaging. *APL Photonics*, 10(10), October 2025.

[31] **Chiara Michelini**, Ugo Zanforlin, Alessia Suprano, Francesco Poggiali, Massimiliano Proietti, Lorenzo Pavesi, and Massimiliano Dispenza. Quantum imaging with undetected photons of non-transmissive target. In Mark A. Itzler, K. Alex McIntosh, and Joshua C. Bienfang, editors, *Advanced Photon Counting Techniques XIX*, page 17. SPIE, May 2025.

[32] MUQUABIS. Multiscale Quantum BioImaging and Spectroscopy. `https://www.muquabis.eu/`, 03 2026. The MUQUABIS project has received funding from Horizon Europe, the European Union's Framework Programme for Research and Innovation, under grant agreement 101070546. Views and opinions expressed are however those of the authors only and do not necessarily reflect those of the European Union. Neither the European Union nor the granting authority can be held responsible for them.

[33] Geoffrey New. *Introduction to Nonlinear Optics*. Cambridge University Press, Cambridge, 1st ed. edition, 2011.

[34] David J. Griffiths. *Introduction to Electrodynamics*. Cambridge University Press, 5 edition, 2023.

[35] Bahaa Saleh and Malvin Teich. *Fundamentals of Photonics, 3rd Edition*. John Wiley & Sons, 02 2019.

[36] Frits. Zernike and John E. Midwinter. *Applied nonlinear optics*. Wiley series in pure and applied optics. Wiley, New York, N.Y., 1973.

[37] Uri Levy, Stanislav Derevyanko, and Yaron Silberberg. *Light Modes of Free Space*, page 237–281. Elsevier, 2016.

[38] John H Moore, Christopher C Davis, Michael A Coplan, and Sandra C Greer. *Building Scientific Apparatus*. Cambridge University Press, Cambridge, 06 2009.

[39] Kiyoshi Kato and Eiko Takaoka. Sellmeier and thermo-optic dispersion formulas for ktp. *Applied Optics*, 41(24):5040, August 2002.

[40] M. Katz, D. Eger, M. B. Oron, and A. Hardy. Erratum: "refractive dispersion curve measurement of ktiopo4 using periodically segmented waveguides and periodically poled crystals" [j. appl. phys. 90, 53 (2001)]. *Journal of Applied Physics*, 92(12):7702–7702, December 2002.

[41] Shai Emanueli and Ady Arie. Temperature-dependent dispersion equations for ktiopo4 and ktioaso4. *Applied Optics*, 42(33):6661, 2003.

[42] Zhanshi Yao, Kaiyi Wu, Bo Xue Tan, Jiawei Wang, Yu Li, and Andrew W. Poon. Integrated

Silicon Photonic Microresonators: Emerging Technologies. *IEEE Journal of Selected Topics in Quantum Electronics*, 24(6), Nov/Dec 2018, Art. no. 5900324.

[43] Charles L. Phillips and John M. Parr. *Signals, Systems, and Transforms*. Prentice-Hall, Inc., USA, 1995.

[44] E. Timurdogan, C. V. Poulton, M. J. Byrd, and M. R. Watts. Electric field-induced second-order nonlinear optical effects in silicon waveguides. *Nature Photonics*, 11(3):200–206, February 2017.

[45] Massimo Borghi, Claudio Castellan, Stefano Signorini, Alessandro Trenti, and Lorenzo Pavesi. Nonlinear silicon photonics. *Journal of Optics*, 19, 06 2017.

[46] Robert W. Boyd. *Nonlinear Optics, 3rd Edition*. Academic Press, 03 2008.

[47] P. A. Franken, A. E. Hill, C. W. Peters, and G. Weinreich. Generation of optical harmonics. *Physical Review Letters*, 7(4):118–119, August 1961.

[48] J. J. Sakurai and Jim Napolitano. *Modern Quantum Mechanics*. Cambridge University Press, 2 edition, 2017.

[49] Andreas Christ, Alessandro Fedrizzi, Hannes Hübel, Thomas Jennewein, and Christine Silberhorn. Chapter 11 - parametric down-conversion. In Alan Migdall, Sergey V. Polyakov, Jingyun Fan, and Joshua C. Bienfang, editors, *Single-Photon Generation and Detection*, volume 45 of *Experimental Methods in the Physical Sciences*, pages 351–410. Academic Press, 2013.

[50] Stefan Lerch, Bänz Bessire, Christof Bernhard, Thomas Feurer, and André Stefanov. Tuning curve of type-0 spontaneous parametric down-conversion. *J. Opt. Soc. Am. B*, 30(4):953–958, Apr 2013.

[51] Ryan S. Bennink. Optimal collinear gaussian beams for spontaneous parametric down-conversion. *Phys. Rev. A*, 81:053805, May 2010.

[52] Laserfabriken. ppKTP Crystal. `https://www.laserfabriken.com/ppktp/`, 08 2025.

[53] Max Born, Emil Wolf, A. B. Bhatia, P. C. Clemmow, D. Gabor, A. R. Stokes, A. M. Taylor, P. A. Wayman, and W. L. Wilcock. *Principles of Optics: Electromagnetic Theory of Propagation, Interference and Diffraction of Light*. Cambridge University Press, October 1999.

[54] Takafumi Ono, Gary F. Sinclair, Damien Bonneau, Mark G. Thompson, Jonathan C. F. Matthews, and John G. Rarity. Observation of nonlinear interference on a silicon photonic chip. *Optics Letters*, 44(5):1277, March 2019.

[55] Stefano Signorini, Mattia Mancinelli, Massimo Borghi, Martino Bernard, Mher Ghulinyan, Georg Pucker, and Lorenzo Pavesi. Intermodal four-wave mixing in silicon waveguides. *Photonics Research*, 6(8):805, July 2018.

[56] Govind P. Agrawal. *Fiber-Optic Communication Systems*. Wiley, May 2002.

[57] Mark Fox. *Quantum Optics: An Introduction*. Oxford University Press, 04 2006.

[58] A. Migdall, Polyakov S. V., Fan J., and J. C. Bienfang. *Single-photon generation and detection: physics and application*. Experimental methods in the physical sciences 45. Elsevier Academic Press, 2013.

[59] S. Signorini and L. Pavesi. On-chip heralded single photon sources. *AVS Quantum Science*, 2(4), October 2020.

[60] M. V. Chekhova and Z. Y. Ou. Nonlinear interferometers in quantum optics. *Advances in Optics and Photonics*, 8(1):104, March 2016.

[61] L. Mandel. Coherence and indistinguishability. *Optics Letters*, 16(23):1882, December 1991.

[62] L. Mandel. Quantum effects in one-photon and two-photon interference. *Reviews of Modern Physics*, 71(2):S274–S282, March 1999.

[63] Christopher C. Gerry and Peter L. Knight. *Introductory Quantum Optics*. Cambridge University Press, 2 edition, 2023.

[64] M. Liscidini and J. E. Sipe. Stimulated emission tomography. *Physical Review Letters*, 111(19), November 2013.

[65] T. J. Herzog, J. G. Rarity, H. Weinfurter, and A. Zeilinger. Frustrated two-photon creation via interference. *Physical Review Letters*, 72(5):629–632, January 1994.

[66] Nathan R. Gemmell, Jefferson Flórez, Emma Pearce, Olaf Czerwinski, Chris C. Phillips, Rupert F. Oulton, and Alex S. Clark. Loss-compensated and enhanced midinfrared interaction-free sensing with undetected photons. *Physical Review Applied*, 19(5), May 2023.

[67] Lukas Novotny and Bert Hecht. *Principles of Nano-Optics*. Cambridge University Press, September 2012.

[68] Eugene Hecht. *Optics*. Addison Wesley, 4th intern edition, 2002.

[69] Balakrishnan Viswanathan, Gabriela Barreto Lemos, and Mayukh Lahiri. Resolution limit in quantum imaging with undetected photons using position correlations. *Optics Express*, 29(23):38185, November 2021.

[70] Marta Gilaberte Basset, René Sondenheimer, Jorge Fuenzalida, Andres Vega, Sebastian Töpfer, Elkin A. Santos, Sina Saravi, Frank Setzpfandt, Fabian Steinlechner, and Markus Gräfe. Experimental analysis of image resolution of quantum imaging with undetected light through position correlations. *Phys. Rev. A*, 108:052610, Nov 2023.

[71] S.P. Walborn, C.H. Monken, S. Pádua, and P.H. Souto Ribeiro. Spatial correlations in parametric down-conversion. *Physics Reports*, 495(4–5):87–139, October 2010.

[72] Armin Hochrainer, Mayukh Lahiri, Radek Lapkiewicz, Gabriela Barreto Lemos, and Anton Zeilinger. Quantifying the momentum correlation between two light beams by detecting one. *Proceedings of the National Academy of Sciences*, 114(7):1508–1511, January 2017.

[73] Balakrishnan Viswanathan, Gabriela Barreto Lemos, and Mayukh Lahiri. Position correlation enabled quantum imaging with undetected photons. *Optics Letters*, 46(15):3496, July 2021.

[74] Jorge Fuenzalida, Armin Hochrainer, Gabriela Barreto Lemos, Evelyn A. Ortega, Radek Lapkiewicz, Mayukh Lahiri, and Anton Zeilinger. Resolution of quantum imaging with undetected photons. *Quantum*, 6:646, February 2022.

[75] Inna Kviatkovsky, Helen M. Chrzanowski, Ellen G. Avery, Hendrik Bartolomaeus, and Sven Ramelow. Microscopy with undetected photons in the mid-infrared. *Science Advances*, 6(42), October 2020.

[76] Hamamatsu. ORCA-Quest qCMOS camera C15550-20UP - Technical note. `https://www.hamamatsu.com/content/dam/hamamatsu-photonics/sites/documents/99_SALES_LIBRARY/sys/SCAS0154E_C15550-20UP_tec.pdf`, 10 2025.

[77] Daniel Asoubar, Site Zhang, Frank Wyrowski, and Michael Kuhn. Parabasal field decom-

position and its application to non-paraxial propagation. *Optics Express*, 20(21):23502, September 2012.

[78] Mayukh Lahiri, Radek Lapkiewicz, Gabriela Barreto Lemos, and Anton Zeilinger. Theory of quantum imaging with undetected photons. *Phys. Rev. A*, 92:013832, Jul 2015.

[79] Edmund Optics. Why Use a Flat Top Laser Beam? `https://www.edmundoptics.co.uk/knowledge-center/application-notes/optics/why-use-a-flat-top-laser-beam`, 11 2025.

[80] Grant R. Fowles. *Introduction to modern optics / by Grant R. Fowles.* Dover Publications, New York, 2nd ed., dover ed. edition, 1975.

[81] Paolo Mazzoldi, Massimo Nigro, and Cesare Voci. *Fisica. Elettromagnetismo e onde.* Edises, Napoli, 2 edition, 2021.

[82] R. Piazza and V. Degiorgio. *Scattering, Rayleigh*, page 234–242. Elsevier, 2005.

[83] Songcan Lai and Gert von Bally. Fringe contrast evaluation by means of histograms. In Gyorgy Akos, Gabor Lupkovics, and Andras Podmaniczky, editors, *OPTIKA '98: 5th Congress on Modern Optics*, volume 3573, page 384. SPIE, August 1998.

[84] Luis Miguel Sanchez-Brea, Juan Antonio Quiroga, Angel Garcia-Botella, and Eusebio Bernabeu. Histogram-based method for contrast measurement. *Applied Optics*, 39(23):4098, August 2000.

[85] L.B. Soldano and E.C.M. Pennings. Optical multi-mode interference devices based on self-imaging: principles and applications. *Journal of Lightwave Technology*, 13(4):615–627, April 1995.

[86] Daoxin Dai and Shipeng Wang. Asymmetric directional couplers based on silicon nanophotonic waveguides and applications. *Frontiers of Optoelectronics*, 9(3):450–465, September 2016.

[87] Mario Bertolotti, Victor Bogdanov, Aldo Ferrari, Andrei Jascow, Natalia Nazorova, Alexander Pikhtin, and Luigi Schirone. Temperature dependence of the refractive index in semiconductors. *Journal of the Optical Society of America B*, 7(6):918, June 1990.

[88] A. von Meier. *Electric Power Systems: A Conceptual Introduction.* Wiley survival guides in engineering and science. Wiley, 2006.